NEXT GENERATION COMPUTER CONTROLLED OPTICAL SURFACING

By

Dae Wook Kim

A Dissertation Submitted to the Faculty of the

COLLEGE OF OPTICAL SCIENCES

In Partial Fulfillment of the Requirements
For the Degree of

DOCTOR OF PHILOSOPHY

In the Graduate College

THE UNIVERSITY OF ARIZONA

2009

THE UNIVERSITY OF ARIZONA
GRADUATE COLLEGE

As members of the Dissertation Committee, we certify that we have read the dissertation

prepared by Dae Wook Kim

entitled "Next Generation Computer Controlled Optical Surfacing"

and recommend that it be accepted as fulfilling the dissertation requirement for the

Degree of Doctor of Philosophy

____ Date: Dec. 1, 2009
James Burge

____ Date: Dec. 1, 2009
Robert Parks

____ Date: Dec. 1, 2009
Hubert Martin

____ Date: Dec. 1, 2009
Jose Sasian

Final approval and acceptance of this dissertation is contingent upon the candidate's submission of the final copies of the dissertation to the Graduate College.

I hereby certify that I have read this dissertation prepared under my direction and recommend that it be accepted as fulfilling the dissertation requirement.

____ Date: Dec. 1, 2009
Dissertation Director: James Burge

STATEMENT BY AUTHOR

SIGNED: Dae Wook Kim

ACKNOWLEDGEMENTS

James Burge: My captain. Thank you for everything. I am sure that I would not be here today without you.

Marty Valente: Your unconditional supports and helps. I will always remember them. Thank you.

Robert Parks, Hubert Martin and Jose Sasian: Having you all in my dissertation committee was a blessing. Thank you.

Sug-Whan Kim: This work is based on our vision and dream. Thank you.

Hwa-Yeob Kim, Jin-Sook Kim, Jae-Wook Kim, Byung-Suk Lee and Young-Ok Kim: My parents, my brother. Simply, I love you.

Large Optics Fabrication and Testing group: My good friends and peers. I will never forget your helps throughout the years.

Optical Engineering and Fabrication Facility: Opticians, engineering and administrative staffs. Thank you my friends for your supports and helps.

OPTJCS group: It was my pleasure to investigate and explore the beauty of optics with you.

Global Space Optics Laboratory: I owe much to you.

Thank you, God.

DEDICATION

To Heeyoung

Aiden Jun and Daniel Yu

with love

TABLE OF CONTENTS

LIST OF FIGURES

APPENDIX A: Rigid Conformal Polishing Tool using Non-linear Visco-elastic Effect

APPENDIX B: Parametric Smoothing Model for Rigid Conformal Polishing Laps that use Visco-elastic Materials

APPENDIX C: Static Tool Influence Function for Fabrication Simulation of Hexagonal Mirror Segments for Extremely Large Telescopes

APPENDIX D: Parametric Modeling of Edge Effects for Polishing Tool Influence Functions

APPENDIX E: Edge Tool Influence Function Library using the Parametric Edge Model for Computer Controlled Optical Surfacing

APPENDIX F: Non-sequential Optimization Technique for a Computer Controlled Optical Surfacing Process using Multiple Tool Influence Functions

LIST OF TABLES

ABSTRACT

Precision optics can be accurately fabricated by computer controlled optical surfacing (CCOS) that uses well characterized polishing tools driven by numerically controlled machines. The CCOS process is optimized to vary the dwell time of the tool on the workpiece according to the desired removal and the calibrated tool influence function (TIF), which is the shape of the wear function by the tool. This study investigates four major topics to improve current CCOS processes, and provides new solutions and approaches for the next generation CCOS processes.

The first topic is to develop a tool for highly aspheric optics fabrication. Both the TIF stability and surface finish rely on the tool maintaining intimate contact with the workpiece. Rigid tools smooth the surface, but do not maintain intimate contacts for aspheric surfaces. Flexible tools conform to the surface, but lack smoothing. A rigid conformal (RC) lap using a visco-elastic non-Newtonian medium was developed. It conforms to the aspheric shape, yet maintains stability to provide natural smoothing.

The second topic is a smoothing model for the RC lap. The smoothing naturally removes mid-to-high frequency errors while a large tool runs over the workpiece to remove low frequency errors efficiently. The CCOS process convergence rate can be significantly improved by predicting the smoothing effects. A parametric smoothing model was introduced and verified.

The third topic is establishing a TIF model to represent measured TIFs. While the linear Preston's model works for most cases, non-linear removal behavior as the tool overhangs the workpiece edge introduces a difficulty in modeling. A parametric model for the edge TIFs was introduced and demonstrated. Various TIFs based on the model are provided as a library.

The last topic is an enhanced process optimization technique. A non-sequential optimization technique using multiple TIFs was developed. Operating a CCOS with a small and well characterized TIF achieves excellent performance, but takes a long time. Sequential polishing runs using large and small tools can reduce this polishing time. The non-sequential approach performs multiple dwell time optimizations for the entire CCOS runs simultaneously. The actual runs will be sequential, but the optimization is comprehensive.

1. INTRODUCTION

Various computer controlled optical surfacing (CCOS) processes have been developed since the 1960s [1-9]. These CCOS processes can provide good solutions for fabrication of precision optics because of their high convergence rate based on deterministic removal processes. Many large aspheric optical surfaces and off-axis segments have been successfully fabricated using these CCOS techniques [4-9]. Nevertheless, further development in the efficiency and performance of the current CCOS techniques is highly desired to meet the demanding target specifications of many next generation optical systems, which usually have hundreds of aspheric mirrors (*e.g.* Thirty Meter Telescope [10], European Extremely Large Telescope [11] and Laser Inertial Fusion Engine [12]) or large off axis mirrors (*e.g.* Giant Magellan Telescope (GMT) [13]).

Those extremely large telescopes (ELTs) use giant segmented primary mirrors with hundreds of square meter collecting area, and may have hundreds of segments. Each meter-class segment is to have the surface form accuracy of better than 18nm peak-to-valley [14]. Such a primary mirror system is to be phased and aligned to the precision of about 10-20nm RMS (root-mean-square) [15]. The next generation CCOS process needs to fabricate such precision optical surfaces in a highly efficient manner. In addition to the superb figuring ability, suppression of mid-spatial frequency error (*a.k.a.* tool marks) on these precision optical surfaces is important for maximum performance (*i.e.* less scattering and well defined point spread function) of the optical systems [16]. Most of the recent large optical surfaces have been polished until the spatial frequencies of the surface errors satisfied a target structure function or power spectral density (PSD) specification to quantify the target form accuracy as a function of spatial frequencies [16-17]. The demand for an efficient workpiece edge figuring process has been also increased due to the popularity of segmented optics in those next generation optical systems. Because those systems have multiple mirror segments as their primary or secondary mirrors, and the total length of edges is much larger than the conventional system with one mirror, and the edges are distributed across the whole pupil. Thus, a precise and efficient edge fabrication method is important to ensure the final performance of the optical system (*e.g.* light collecting power and spatial resolution based on the point spread function) and reasonable delivery time. Therefore, the improved next generation CCOS technique must provide an efficient fabrication process for a mass-fabrication of aspheric precision optical surfaces.

Most CCOS processes are based on three main components, i) a numerically controlled (NC) polishing machine, ii) a polishing tool and iii) an embedded process control intelligence (*i.e.* process optimization software). The NC polishing machine provides a stable and repeatable control environment to move the polishing tool on a workpiece. The second component polishing tool makes the actual contact and removes material from the workpiece. The tool needs to provide a deterministic tool influence function (TIF), which is the shape of the wear function created by the polishing tool motion and workpiece motion. This well characterized TIF is usually mathematically modeled and used as building blocks in the process optimization software, the last component. The embedded process control intelligence designs and optimizes polishing run parameters, such as tool rpm, tool pressure, and dwell time map (*i.e.* tool ablation time as a function of tool position on a workpiece) to achieve a target removal map. This study provides some novel approaches for the polishing tool and embedded process control intelligence parts, which enables enhanced CCOS processes.

1.1 Rigid Conformal Polishing Tool

The TIF, which is the building block for a CCOS process, is a direct function of tool properties, such as pressure distribution under the tool, tool contact area shape, tool motion, and so forth. Thus, developing a well-behaved tool is an essential component to achieve a deterministic TIF. Tool development for aspheric (or freeform) optics production is an especially complex problem. Because local curvatures of an aspheric surface vary as a function of position on a workpiece, a tool with a rigid surface shape cannot be used. Instead, flexibility is required to maintain intimate contact with the workpiece surface, and not to leave zones in the workpiece surface figure due to the tool-workpiece misfit. However, the smoothing effect that naturally removes mid-to-high spatial frequency errors by a rigid tool rubbing high portions on a rough surface disappears as the tool becomes too compliant [18]. Thus, tool development is the art of balancing between flexibility and rigidity.

The present work in Section 2.1 introduces a rigid conformal (RC) lap, which uses a visco-elastic non-Newtonian fluid (*a.k.a.* solid-liquid) that has both flexibility and rigidity at the same time, but for different time scales. (*Note:* A US provisional patent was filed for the RC lap.) A detailed RC lap structure and specifications of the manufactured RC lap are provided in Sections 2.1.1-2.1.3. The performance demonstration is given in Section 2.1.4.

1.2 Parametric Smoothing Model

As mentioned earlier, the smoothing effect becomes more important for large workpiece fabrication, because it is almost the only way to correct mid-to-high spatial frequency errors smaller than the tool size. Based on the deterministic TIFs of CCOS processes, large-scale errors (*i.e.* low spatial frequency errors) compared to the tool size can be corrected by increasing the dwell time on the error areas. However, this method cannot be used for errors smaller than the tool size unless smaller and smaller tools are utilized. Smaller tools require much higher tool positioning accuracy to avoid residual tool marks, which is another source of mid-spatial frequency errors. Also, the use of small tools increases the overall fabrication time.

Correcting these mid-to-high spatial frequency errors on the optical surfaces is very important for next generation ELTs [10-11, 13] and nuclear fusion energy plants using high power lasers (*e.g.* LIFE [12]). Because the mid-to-high-spatial frequency errors are directly related to the sharpness of the point spread function or the scattering characteristic of high power laser application optics, the overall performance of those systems may be degraded due to these errors.

There have been some quantitative investigations for the smoothing effects for semi-flexible tools. Brown and Parks quantitatively explained the smoothing effects by elastic backed flexible lapping belts in 1981 [19]. The smoothing effect using a large flexible polishing lap was mathematically studied and introduced by Mehta and Reid using the Bridging model [20]. The Bridging model was further developed using a Fourier series decomposition approach by Tuell [18, 21]. These models were successfully demonstrated with experimental data.

The RC lap using the visco-elastic fluid achieved both flexibility and rigidity at the same time, but for different time scales. Because the property of the visco-elastic fluid varies as a function of applied stress frequency, the smoothing effect by the RC lap needs to be described by a new smoothing model.

A parametric smoothing model for the RC lap was developed to quantitatively describe the smoothing effects in Section 2.2. This model uses a parametric approach to include other effects such as fluid dynamics of the polishing compound and total effective stiffness of the whole tool structure. Some theoretical background about the Bridging model for semi-flexible tools is provided in Sections 2.2.1 and 2.2.2. The parametric smoothing model based on the Bridging model is introduced in Section 2.2.3.

Experimental smoothing results by a conventional pitch tool and the RC lap are provided and compared in Section 2.2.4.

1.3 Parametric Modeling of Edge Effects

In order to develop a successful CCOS process including the edge figuring, accurate TIF models to represents the measured TIFs are required. These TIF models can be used to simulate and optimize the CCOS process in the process optimization software. A theoretical TIF can be calculated based on the equation of material removal, Δz, which is known as the Preston's equation,

$$\Delta z(x, y) = \kappa \cdot P(x, y) \cdot V_T(x, y) \cdot \Delta t(x, y) \tag{1}$$

where Δz is the integrated material removal from the workpiece surface, κ the Preston coefficient (*i.e.* removal rate), P pressure on the tool-workpiece contact position, V_T magnitude of relative speed between the tool and workpiece surface and Δt dwell time. It assumes that the integrated material removal, Δz, depends on P, V_T and Δt linearly.

A nominal TIF calculated by integrating Eq. (1) under a moving tool fits well to an experimental (*i.e.* measured) TIF as long as the tool stays inside the workpiece, as shown in Appendix C. However, once the tool overhangs the edge of workpiece, the measured TIF tends to deviate from the nominal behavior due to dramatically varying pressure range, tool bending, and non-linear effects due to tool material (*e.g.* pitch) flow.

Assuming the linearity of Preston's equation, the edge effects can be associated with the pressure distribution on the tool-workpiece contact area. Jones suggested a linear pressure distribution model in 1986 [5]. Luna-Aguilar, et al.(2003) and Cordero-Davila, et al.(2004) developed this approach further using a non-linear high pressure distribution near the edge-side of the workpiece, but they did not report the model's validity by demonstrating it using experimental evidence [22-23].

For any real polishing tool, the actual removal distribution is a complex function of many factors such as tool-workpiece configuration, tool stiffness, polishing compounds, polishing pad, and so forth. Approaches based on an analytical pressure distribution *p(x,y)* [5, 22-23] tend to ignore some of these effects. Also, in the edge TIF cases, the linearity for Preston's equation may need to be reconsidered since the pressure distribution changes over a wide range of pressure. The linearity is usually valid for a moderate range of pressure values for a given polishing configuration.

A parametric edge TIF model to predict the edge TIFs is introduced in Section 2.3. Rather than assigning the edge effects to a certain type of analytical pressure distribution model, we define a parametric model based on measured data that allows us to create an accurate TIF without the need of identifying the actual cause of the abnormal behavior in edge removal. We then re-defined the Preston coefficient, κ, which has been regarded as a constant in the spatial domain, as a function of position in the TIF via the parametric approach. By doing so, we can simulate the combined net effect of many complex factors without adding more terms to the original Preston's equation, Eq. (1). The performance evaluation for the parametric edge TIF model was conducted by comparing the model and measured edge TIFs. A TIF library including various TIFs using this edge model is provided in Appendix E.

1.4 Non-Sequential Optimization Technique

Using the well characterized TIFs, a CCOS run can be optimized and designed. This optimization is mainly based on a de-convolution process of the target removal map using the TIFs. In general, a dwell time map (*i.e.* ablation time as a function of position on the workpiece) is the main optimization subject for the process optimization software to achieve a given target removal map. In other words, the control intelligence uses the TIF as a building block to achieve the target removal map by spatially distributing and accumulating the TIF blocks on the workpiece. Because no general solution to the dwell time map exists, as briefly explained in Appendix F, finding the best dwell time map solution becomes an optimization problem. There has been a wide range of study for dwell time map optimization techniques (*e.g.* Fourier transform based algorithms, matrix-based least-squares algorithms) [24-27].

In a conventional CCOS process, a single dwell time map of a TIF is optimized to achieve a target material removal. The convergence rate and overall efficiency of CCOS figuring are optimized using a sequence of polishing runs, where the largest scale irregularities are addressed by large tools. Smaller tools are used to correct small scale irregularities and tool marks from the larger tools. These multiple CCOS runs are optimized one by one. For instance, a large tool may be used to address the current target removal. Then, a small tool is used to remove the remaining target removal. This method works, but may not be optimal.

A new CCOS process suggested in Section 2.4 uses a non-sequential optimization technique utilizing multiple TIFs simultaneously in a single CCOS run optimization, while the conventional CCOS processes use TIFs in a sequential manner. The actual polishing runs are still to be sequential under the guidance of comprehensive optimization. This new technique, which enables the ensemble of various TIFs, forms an attractive solution for the mass fabrication capability of high quality optical surfaces. General concepts and enhanced merit functions for the non-sequential optimization are introduced in Sections 2.4.1-2.4.2. The structure of a non-sequential optimization engine is presented in Section 2.4.3. Its performance is compared with the conventional optimization technique cases in Section 2.4.4. The comparison shows significant improvements in figuring efficiency and mid-spatial frequency error suppression.

Note: This dissertation is based on a collection of published journal articles. All the published works were logically connected and integrated into this dissertation in a coherent manner. The in-depth discussions and details of the studies are given in the appended reprints of the papers.

2. PRESENT STUDY

The methods, results, and conclusions of this study

are presented in the paper appended to this dissertation.

The following is a summary of the key findings in the articles.

2.1 Rigid Conformal Polishing Tool using Non-linear Visco-elastic effect

For a polishing tool, which is stroked on the surface, both the TIF stability and surface finish by the tool rely on the polishing interface maintaining intimate contact with the workpiece. Pitch tools serve this function for surfaces that are near spherical, where the curvature has small variation across the part. The rigidity of such tools provides natural smoothing of the surface, but limits the application for aspheric surfaces. In contrast, highly flexible tools, such as those created with an air bonnet or magnetorheological fluid, conform to the surface, but lack intrinsic stiffness, so they provide little natural smoothing. A RC lap with both rigidity and flexibility at the same time was developed using a non-linear visco-elastic (*i.e.* non-Newtonian) medium. The following Sections 2.1.1-2.1.4 are a summary of an article submitted to the journal *Optics Express*, Appendix A.

2.1.1 Visco-elastic non-Newtonian fluid

Since the days of Sir Isaac Newton, opticians have relied on the visco-elastic properties of pitch to create effective polishing tools. Pitch acts as a highly viscous Newtonian fluid for long time scales – it undergoes shear motion that is proportional to the shear stress, so it flows to conform to the shape of the workpiece. At constant temperature, this flow is characterized by the viscosity and is described by the Navier-Stokes equations [28]. Pitch has two principal limitations for polishing: the TIF tends to be unstable, and it does not flow fast enough to accommodate the use of large tools on steep aspheric surfaces.

In order to insure that the tool conforms to the surface, we desire a lap made from a material that will flow much more quickly than pitch. Yet we wish to maintain the tool's rigid behavior to preserve the natural smoothing abilities. Such a tool can be made by replacing the pitch with a visco-elastic non-Newtonian. The visco-elastic fluid will act like a solid for a short time period under stress. If stress is applied over a long time period, it flows like a liquid.

For an example, a bar made of non-Newtonian silastic polymer (SP) (~2×2×15cm pink bar) was hand-molded as shown in Fig. 1.

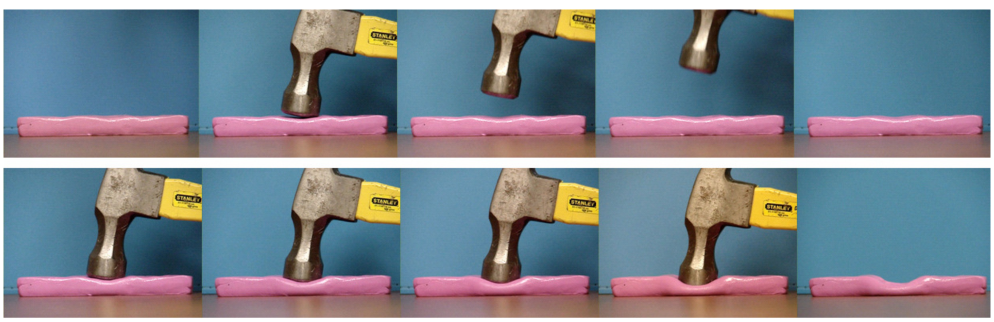

Fig. 1. Two phases of a visco-elastic non-Newtonian silastic polymer: solid-like phase for <~0.1 seconds hammering impulse (top), and liquid-like phase for ~17 seconds long stress by hammer's weight (bottom).

In the upper figure, the bar was hammered for less than ~0.1 seconds time (*i.e.* impact duration). The bar was deformed by a small amount after the harsh impact. This is the solid-like behavior of the non-Newtonian fluid. The lower figure shows a large deformation of the bar. When the hammer was gently placed on the bar loaded by only its weight, the bar started to flow just like a liquid. The duration of the load was ~17 seconds, much longer than the hammer strike case. The time duration threshold that distinguishes the two phases varies for different non-Newtonian fluids.

2.1.2 General comparison between different tool types

There are three general types of polishing tools: i) rigid tools, ii) semi-flexible tools, and iii) compliant tools. The schematic tool structures for these tool types are given in Fig. 2.

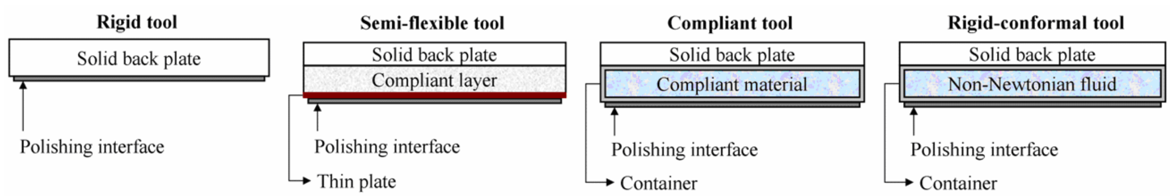

Fig. 2. Schematic tool structures of four different tool types

Each type has its own optimal flexibility and rigidity for its major purpose as a polishing tool. A general comparison between different tool types is summarized in Table 1. As you see in Table 1, it is difficult to achieve both flexibility and rigidity at the same time due to their conflicting characteristics.

However, the RC lap takes the advantages from both the rigid and compliant tool in two different time scales. Because the tool motion (*e.g.* orbital motion in Appendix D) is usually fast (*e.g.* >10Hz) relative to the local features under the motion (*e.g.* bumps), the RC lap acts like a high storage modulus rigid tool with respect to that time scale. (A detailed explanation about the storage modulus is given in Section 2.2.2.) For instance, if the tool is orbiting at 100rpm on a bumpy area on the workpiece, the tool rubs on the bumps with high local pressure. Thus, it can smooth the bumpy surface. Also, the RC lap can go over the edge of the workpiece because the tool does not conform to the edge as long as the tool spins or orbits at high speed. However, the tool still fits to the local curvature changes of the workpiece since the RC lap moves on the workpiece relatively slowly (*e.g.* ~1 rpm workpiece rotation) along the tool path. (This local curvature characteristic was well described by Parks [29].) For instance, for an off-axis parabolic workpiece, the tool may travel around the workpiece once a minute. The tool will fit to the slowly varying local curvature of the off-axis part. The non-Newtonian fluid flows like a liquid for this long time scale motion. Thus, a RC lap can be used for many different workpieces (including aspheric and freeform surfaces) like a compliant tool. Also, it is not difficult to make a large tool (*e.g.* >30cm diameter tool) because the non-Newtonian fluid is more easily handled (or contained) than a liquid or air. The tool manufacturing cost is also low.

Table 1. General comparison between different tool types [a, b]

	Rigid tool	Semi-flexible tool	Compliant tool	Rigid conformal tool
Making large tool (*e.g.* >30cm)	Easy	Easy	Difficult	Easy
Cost (including a NC machine)	Inexpensive	Medium	Expensive	Inexpensive
A tool for different workpieces	No	Limited	Yes	Yes
Smoothing	Good	Good	Poor	Medium
Predictability	Low	Fair	Excellent	Good
Fitting to workpiece surface	Poor	Fair	Good	Good
Working on aspheric workpiece	Difficult	Good	Easy	Easy
Working on freeform workpiece	Difficult	Hard	Easy	Easy
Working over the edge	Yes	Yes	No	Yes
Tool maintenance	Difficult	Easy	Medium	Easy

[a]Blue items are usually regarded as advantages.
[b]This is just a general comparison. These characteristics may vary for a specific tool.

2.1.3 Manufactured RC lap

Three RC laps (110, 220, and 330mm in diameter) were manufactured. Among many visco-elastic non-Newtonian fluids, Silly Putty™ was used in these RC laps. The 220mm RC lap and 330mm RC lap are presented as an example in Fig. 3 and 4, respectively. The 330mm RC lap was used on the 8.4m diameter GMT off axis segment at the Steward Observatory Mirror Lab.

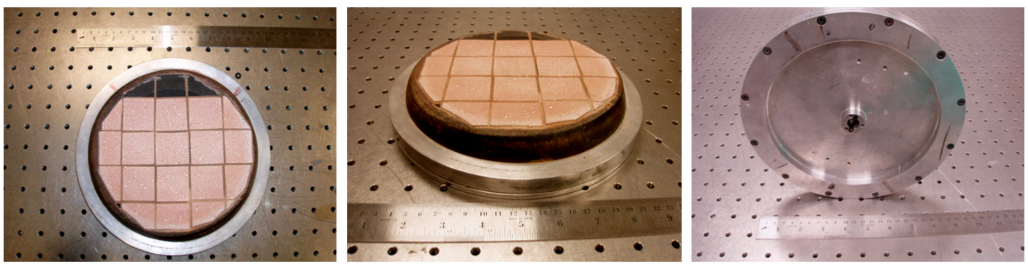

Fig. 3. Manufactured 220mm diameter RC lap (bottom, side, top view from left to right) Three of the polishing pad tiles were intentionally removed to show the structure below.

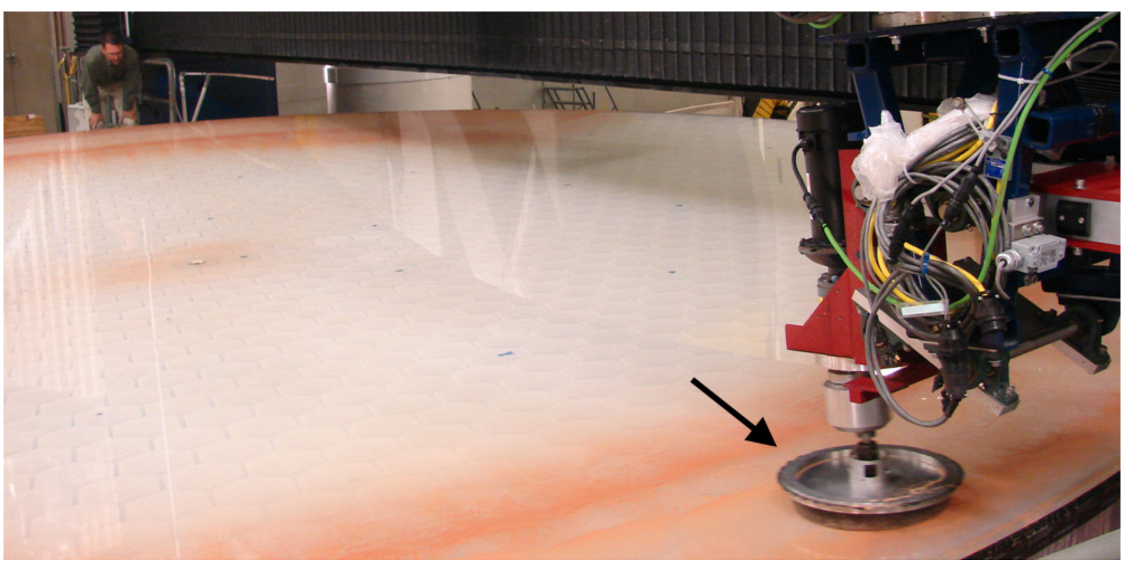

Fig. 4. 330mm diameter RC lap (black arrow) on the 8.4m diameter GMT off axis segment at the Steward Observatory Mirror Lab.

A machined aluminum back plate and a Bellofram^{TM} diaphragm [30] were used with a polyurethane polishing pad. A Cerium doped polyurethane polishing pad LP-66 was tiled for channels. (LP-66 is a polyurethane polishing pad sold by Universal Photonics INC.) Detailed specification of the RC laps is listed in Table. 2.

Table 2. Specification of three RC laps

Tool diameter	110, 220, 330mm
Aluminum back plate thickness	10mm
Non-Newtonian fluid	Silly-Putty^{TM}
Non-Newtonian fluid thickness	10-20mm
Diaphragm	Bellofram^{TM} diaphragm
Polyurethane polishing pad	LP-66 (Cerium doped pad)
Polyurethane polishing pad thickness	0.5mm

2.1.4 Performance of the RC lap

A polyurethane polishing pad needs to be conditioned (*i.e.* breaking down the rough pad surface) on a conditioning workpiece before its first polishing run. In order to qualitatively analyze the conditioning process and the performance of the RC lap after conditioning, the Preston constant and surface roughness values were measured as a function of tool age. The tool age was set to zero when a new polyurethane pad was attached to the RC lap.

Approximately 100 experiments using the 110mm RC lap were conducted on five Pyrex workpieces. The RC lap was run within the optimal RC lap operation range discussed in Appendix A. The experimental results are plotted in Fig. 5.

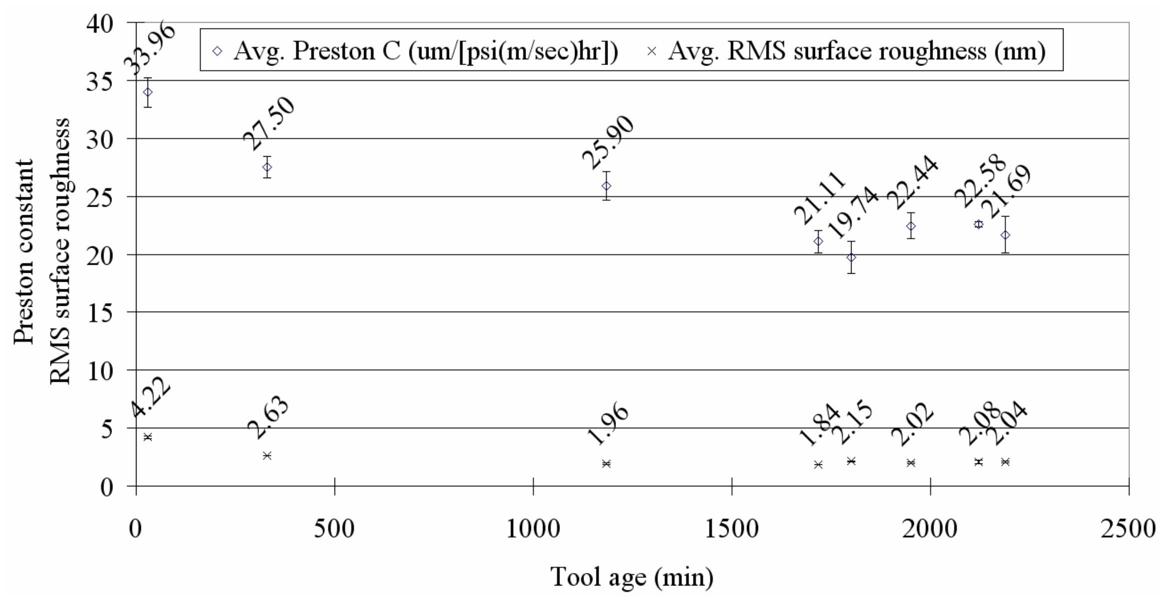

Fig. 5. Preston's constant and RMS surface roughness *vs.* tool age (*Note:* Error-bars represent the standard deviation of the value)

The Preston constant values (diamond marker in Fig. 5) were ~34μm/[psi(m/sec)hr] when the RC lap was used for the first time. As the tool age approached ~1700minutes, the Preston constant stabilized at ~21μm/[psi(m/sec)hr]. The surface roughness values were stable at ~2nm RMS after ~1200minutes tool age. Of course, the tool age axis can be scaled depending on the initial surface roughness of the conditioning workpiece, tool pressure, and tool speed. For instance, higher tool speed and pressure may reduce the conditioning time due to the higher removal per unit time. Once the RC lap was conditioned (*e.g.* >1700minutes tool age in this case), the Preston constant varied with only ~10% standard deviation. The conditioning process and stable Preston constant after conditioning were successfully demonstrated for the RC lap.

The surface roughness after a polishing run is another important criterion used to estimate a tool's performance. If a tool leaves a smooth surface which meets a target specification, the workpiece can be finished using the tool. Otherwise, additional processes using other tools (*e.g.* pitch tools) are required for the final touch-up process to improve the surface roughness. This increases the complexity and time of the CCOS process, so a tool giving a good surface finish is highly desirable.

The surface roughness is a function of many parameters, such as glass material, polishing compound type, and so forth. It is, therefore, invalid to say a tool always gives a certain value for RMS surface roughness. Instead, a tool should be compared to another tool in a similar condition. We set a classical pitch tool as our reference for this study. The pitch tool is well known for its excellent surface finish.

A ULE substrate was used as a common workpiece. The surface roughness after each run was measured using a Wyko NT9800™ interferometer. (Wyko NT9800™ is a trademark of Veeco.) More information about the surface roughness experiment set-up is provided in Table. 3.

Table 3. Two surface roughness experiment set-ups

	110mm RC lap	110mm pitch tool
Polishing Compound	Hastilite ZD	Rhodite 906
Tool Motion	Orbital	Orbital
Workpiece	ULE	ULE
Measurement area	~0.2 by 0.3mm	~0.2 by 0.3mm
Sampling interval	484nm	484nm

The experimental surface roughness results are presented in Fig. 6. The reference target surface roughness was set as ~0.9nm RMS, which was an average value from the experiments using a pitch tool with Rhodite 906 polishing compound. The surface finish from the RC lap with Hastilite ZD polishing compound was superb. For 10 repeated experiments, the average surface roughness was ~0.75nm RMS with ~0.1nm standard deviation, which is similar or even slightly better than the pitch tool case. (We acknowledge that there may be a better polishing compound for the pitch tool for this specific set-up, which could have given better surface finish. We use this result only as a brief reference for comparison purposes.)

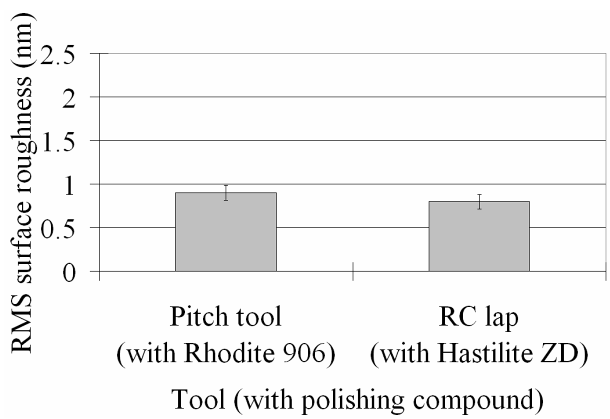

Fig. 6. Surface roughness using a pitch tool and RC lap on a ULE substrate (*Note:* Error-bars represent the standard deviation of the value)

We have demonstrated that the RC lap, with appropriate polishing compound which depends on a given polishing configuration, can provide a <1nm RMS super smooth surface finish. This may eliminate the need for an extra final touch-up step for most CCOS processes, which usually have <2nm RMS surface roughness target specifications.

In summary, the measured experimental data using the RC lap successfully showed TIF stability of <10% and superb surface finish with <10Å roughness on a ULE substrate. The smoothing characteristic of the RC lap is investigated in Section 2.2.

2.2 Parametric Smoothing Model for Rigid Conformal Lap

A parametric smoothing model to describe and predict the smoothing effects by the RC lap was developed. The smoothing factor *SF* was defined to describe the smoothing effect. For a given RC lap the smoothing action is conveniently represented by a linear function *SF vs.* PV_{ini} (*i.e.* initial peak-to-valley of ripples). In order to include other unknown factors, which affect the smoothing action, the smoothing model was parameterized with two parameters. The following Sections 2.2.1-2.2.4 are a summary of an article submitted to the journal *Optics Express*, Appendix B.

2.2.1 Bridging model for smoothing effects by semi-flexible tools

One of the most common approaches to balance between flexibility and rigidity is using semi-flexible tools as shown in Fig. 2. It usually uses a relatively thin metal plate as a tool base, so that the plate's low order bending modes are used to fit the workpiece local curvatures. A foam layer is often placed between the thin plate and another base structure (*e.g.* thick plate). A polishing pad (*e.g.* polyurethane pad) or pitch is used under the semi-flexible thin plate as a polishing interface material.

In order to describe the smoothing effects by semi-flexible tools, the Bridging model was introduced [20]. As the tool moves on the workpiece, it continuously bends by different amounts to fit the local curvature, resulting in continuous changes in the pressure distribution under the tool. If a semi-flexible tool meets mid-spatial frequency ripples, the tool contacts the ridges of highs in the surface with higher pressure, and begins to smooth them out. The lap may be imagined to form a bridge across the ridges [20].

For a semi-flexible tool, the strains induced from the thin plate bending influence the polishing pressure distribution. Kirchhoff's thin plate equations were modified to include the effect of transverse shear strain. For the one-dimensional case, the polishing pressure distribution *p(x)* due to the sinusoidal error *error(x)* on the surface can be derived based on the theory of elasticity as

$$error(x) = PV(1 - \sin(2\pi \cdot \xi \cdot x)) \tag{2}$$

$$P(x) = P_{nominal} + \frac{error(x)}{\frac{1}{D_{plate} \cdot (2\pi\xi)^4} + \frac{1}{D_{s\_plate} \cdot (2\pi\xi)^2} + \frac{1}{\kappa_{total}}} \tag{3}$$

where PV is the peak-to-valley magnitude of the sinusoidal error, ξ is the spatial frequency of the surface error, $P_{nominal}$ is the nominal pressure under the tool, D_{plate} is the flexural rigidity of the plate, D_{s_plate} is the transverse shear stiffness of the plate, and κ_{total} is the compressive stiffness of the whole tool including elastic material (*e.g.* pitch) and polishing interface material (*e.g.* polyurethane pad) [20]. The flexural rigidity and transverse shear stiffness of the flexible thin plate are defined as

$$D_{plate} = E_{plate} \cdot t_{plate}{}^3 / 12(1 - \nu_{plate}{}^2) \tag{4}$$

$$D_{s\_plate} = E_{plate} \cdot t_{plate} / 2(1 - \nu_{plate}) \tag{5}$$

where E_{plate} is the Young's modulus of the plate material, t_{plate} is the plate thickness, and ν_{plate} is the Poisson's ratio of the plate.

The Bridging model in Eq. (3) describing the smoothing effects by a semi-flexible tool was successfully demonstrated with experimental results [20].

2.2.2 Dynamic modulus of non-Newtonian fluid

Non-Newtonian fluids can resist deformation in a solid-like or fluid-like manner depending on the frequency of the applied stress. In order to quantitatively describe these time-dependent characteristics, the dynamic modulus is used. The dynamic modulus is defined as the ratio of the stress to strain under an oscillating stress condition.

Two dynamic modulus values, tensile storage modulus and loss modulus, are defined as Eq. (6) and (7). The storage modulus is related to the elastic deformation, and the loss modulus is related to the time-dependent visco-elastic behavior of a non-Newtonian fluid.

$$Storage\ modulus: E' = \frac{\sigma_0}{\varepsilon_0}\cos\delta \tag{6}$$

$$Loss\,modulus: E'' = \frac{\sigma_0}{\varepsilon_0}\sin\delta \tag{7}$$

where the oscillating stress and strain are expressed as

$$\varepsilon = \varepsilon_0 \sin(t\omega) \tag{8}$$

$$\sigma = \sigma_0 \sin(t\omega + \delta) \tag{9}$$

The time, t, dependent strain ε has amplitude ε_0 and angular frequency ω. The time dependent stress σ has amplitude σ_0 and same angular frequency ω with phase lag δ between the stress and strain [31].

The phase lag δ is a function of the angular frequency ω for the visco-elastic non-Newtonian fluid. For an ideal solid, the strain and stress are oscillating in phase (*i.e.* δ=0°). If the material is an ideal viscous fluid, the stress is 90° out of phase (*i.e.* δ=90°) with the strain. A loss tangent, which is the ratio between the storage and loss modulus, is a convenient measure of the relative contribution of the solid-like and fluid-like mechanical responses [32]. The loss factor $\tan\delta$ is defined as

$$\tan\delta = \frac{E''}{E'} \quad . \qquad (10)$$

For instance, $\tan\delta > 1$ indicates a fluid-like behavior of the non-Newtonian material. If $\tan\delta < 1$, it means that the solid-like response is dominant over the fluid-like response. Thus, for efficient smoothing actions, the RC lap needs to be run under conditions where $\tan\delta < 1$.

Some measured storage modulus and loss tangent values for fused silica and silastic polymer Silly-Putty™ (SP) were obtained from the literature, and are presented in Fig. 7 [32]. Because fused silica can be regarded as an elastic solid, the loss tangent is almost zero. Also, the storage modulus is almost a constant ~70GPa over the 0-10Hz oscillating stress frequencies. In contrast, the SP is a non-Newtonian fluid, which contains a visco-elastic agent (polydimethylsiloxane). The frequency dependence of the storage modulus is clearly shown in Fig. 7 (right). The SP begins to act like a solid (*i.e.* $\tan\delta<1$) when the applied stress frequency is larger than ~1Hz [32].

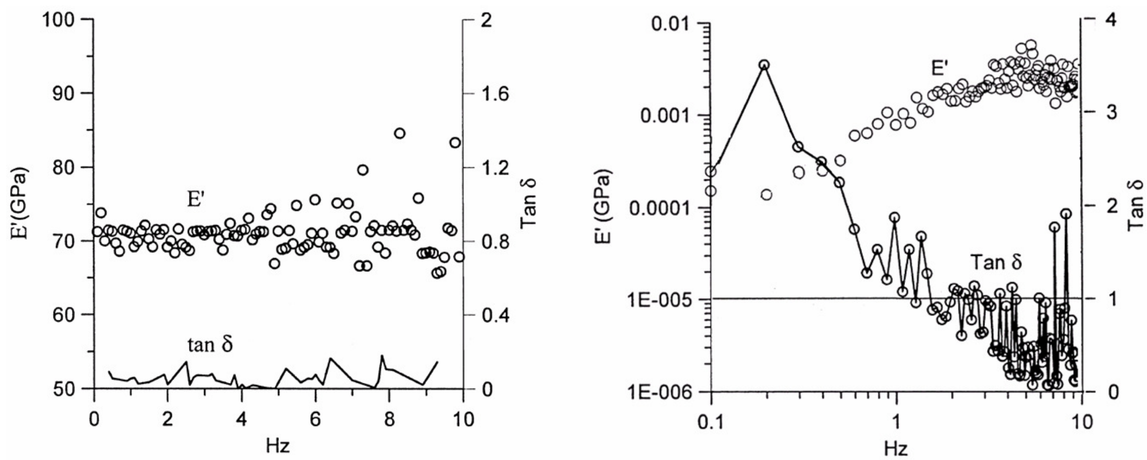

Fig. 7. Storage modulus E' and loss factor $tan\delta$ for fused silica (left) and Silly-Putty™ (right) as a function of applied stress frequency from the literature [32]

2.2.3 Parametric smoothing model for RC lap

The smoothing action by the RC lap can be described using the storage modulus of the visco-elastic non-Newtonian material. Because there is no flexible thin plate in RC laps, the Bridging model in Eq. (3) can be simplified as

$$P(x) = P_{nominal} + \kappa_{total} \cdot error(x) \ . \tag{11}$$

Because the elastic material (*i.e.* visco-elastic material under $\tan\delta<1$ condition) in the RC lap is the main source of the total compressive compliance of the tool, the total stiffness κ_{total} can be approximated by two springs connected in series as

$$\frac{1}{\kappa_{total}} = \frac{1}{\kappa_{elastic}} + \frac{1}{\kappa_{others}} \tag{12}$$

where $\kappa_{elastic}$ is the stiffness of the elastic material and κ_{others} is the combined stiffness of all other structures including polishing pad, polishing compound fluid, wrapping material, and so forth. Because the elastic material is a non-Newtonian fluid in the RC lap, the compressive stiffness $\kappa_{elastic}$ is a function of applied stress frequency ω.

By combining Eq. (11) and (12) the pressure distribution under the RC lap is expressed as

$$P(x) = P_{nominal} + \kappa_{total} \cdot error(x) = P_{nominal} + \frac{1}{\dfrac{1}{\kappa_{elastic}} + \dfrac{1}{\kappa_{others}}} \cdot error(x) \quad . \tag{13}$$

The stiffness of the elastic material $\kappa_{elastic}$ can be expressed in terms of the storage modulus in Section 2.2.2, which defines the local pressure due to a bump on the workpiece. If an elastic material with storage modulus E' has a thickness L and is compressed by a bump of height ΔL, the compressive stiffness $\kappa_{elastic}$ is

$$\kappa_{elastic} = \frac{\sigma_0}{\Delta L} = \frac{\varepsilon_0 \cdot E'/\cos\delta}{\Delta L} = \frac{\{\Delta L/L\} \cdot E'/\cos\delta}{\Delta L} = \frac{E'}{L \cdot \cos\delta} \tag{14}$$

based on Eq. (6).

The applied angular frequency ω is determined by the spatial frequency of the surface error ξ and the speed of the tool motion V_{tool_motion} as

$$\omega = \frac{2\pi}{T} = \frac{2\pi}{(1/\xi \cdot V_{tool\_motion})} = 2\pi \cdot \xi \cdot V_{tool\_motion} \tag{15}$$

where T is the time interval between a position under the tool sees two adjacent peaks in the sinusoidal ripple, and V_{tool_motion} is the speed of the tool motion.

In most smoothing cases, the practical interest is not in the polishing pressure distribution itself, but in the speed of the smoothing action using the pressure distribution on a given ripple as shown in Fig. 8. This can be modeled by using the pressure distribution in the Preston's equation in Eq. (1).

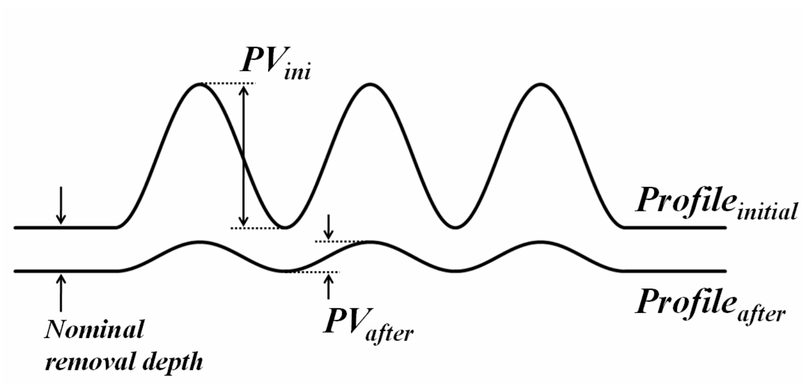

Fig. 8. The sinusoidal ripple profiles (before and after smoothing), which shows the values to determine the smoothing factor *SF* in Eq. (19)

For a given initial sinusoidal ripple magnitude PV_{ini}, the additional polishing pressure P_{add} on the peak is

$$P_{add} = P - P_{nominal} = \frac{1}{\frac{1}{\kappa_{elastic}} + \frac{1}{\kappa_{others}}} \cdot PV_{ini} \tag{16}$$

from Eq. (13). Then, for a dwell time Δt, the decrease in the ripple magnitude ΔPV is calculated using the Preston's equation as

$$\Delta PV = PV_{ini} - PV_{after} = R_{Preston} \cdot P_{add} \cdot V_{tool\_workpiece} \cdot \Delta t \tag{17}$$

where $R_{Preston}$ is the Preston coefficient (*i.e.* removal rate). In order to normalize ΔPV, the nominal removal depth (*i.e.* removal depth from the nominal pressure) is used as

$$nominal\_removal\_depth = R_{Preston} \cdot P_{nominal} \cdot V_{tool\_workpiece} \cdot \Delta t \ . \tag{18}$$

Using Eq. (16), (17) and (18), the smoothing factor *SF* is defined as

$$SF \equiv \frac{\Delta PV}{nominal\_removal\_depth} = \frac{1}{P_{nominal} \cdot (\dfrac{1}{\kappa_{elastic}(\omega)} + \dfrac{1}{\kappa_{others}})} \cdot PV_{ini} \quad . \tag{19}$$

This definition for the smoothing factor in Eq. (19) turns out to be very useful, because *SF* is a linear function of PV_{ini}. For instance, the smoothing factor can be easily calculated for a given initial ripple magnitude.

Because the real smoothing effect may be affected by other complex factors such as shear stiffness characteristics of polishing pads and wrapping materials (*e.g.* the diaphragm in Table 2) and fluid dynamics of polishing compounds, the theoretical smoothing model in Eq. (19) was parameterized using two parameters C_1 and C_2 to fit the measured data. The first parameter C_1 represents κ_{others} and some other unknown effects, which may change the slope of the linear *SF* function. As the PV_{ini} becomes smaller and smaller the fluid dynamics of the polishing compound may begin to limit the smoothing action. This can give a limiting minimum ripple magnitude PV_{min} of the ripple, which means no more smoothing actions below PV_{min}. This can be represented as an x-intercept C_2 in *SF vs.* PV_{ini} graphs. The resulting parametric smoothing model for the RC lap is

$$SF \equiv \frac{1}{P_{nominal} \cdot (\dfrac{1}{\kappa_{elastic}(\omega)} + \dfrac{1}{C_1})} \cdot (PV_{ini} - C_2) \tag{20}$$

where C_1 is the slope correction parameter and C_2 is the x-intercept parameter. Because this is a linear function, these two parameters can be easily determined in practice by performing a few smoothing runs using a given polishing tool.

2.2.4 Experimental verification of the parametric smoothing model

Smoothing experiments to verify the parametric smoothing model were conducted using a conventional pitch tool and a RC lap. For the experiments, sinusoidal ripples were generated on Pyrex substrates and measured using an Intellium™ Fizeau interferometer by ESDI. The experimental set-up is presented in Table 4.

Table 4. Operating condition for the pitch tool and RC lap

Workpiece	250mm diameter Pyrex
Tool motion	Orbital tool motion (w/ 30mm orbital radius)
Tool motion speed	94.2mm/sec (*i.e.* 30RPM)
Nominal tool pressure	2500 Pascal (*i.e.* 0.36PSI)
Polishing compound	Rhodite 906 (Cerium based)
Polishing compound particle size	~2μm

Because the actual ripples were not ideal sinusoidal curves, an averaged peak-to-valley value using >90% and <90% height values was used to calculate the *PV*. Some measured profiles are presented in Fig. 9 as an example. (These profiles represent a few points in Fig. 10.) The decrease in ripple magnitude as the smoothing time gets longer is clearly shown. The pitch tool (left) smoothes out the ripples much quicker than the RC lap (right).

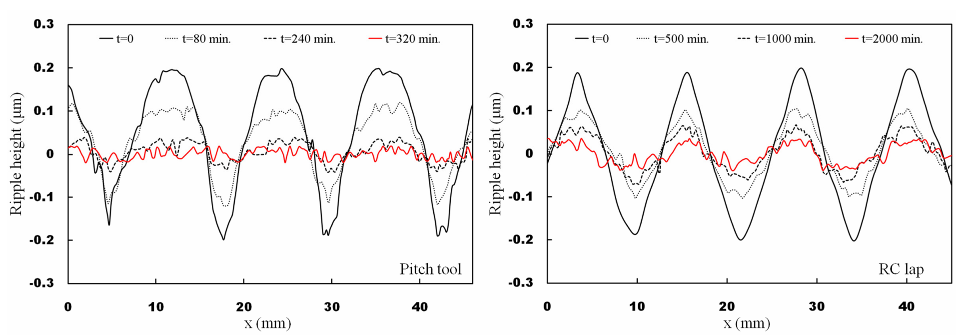

Fig. 9. Measured ripple profiles as tool smoothes out the ripples: pitch tool (left) and RC lap (right) (*Note:* The initial ripple magnitude *PV* was about 0.4μm for both cases.)

Approximately 100 smoothing experiments were performed. The experiments were performed until no more reduction in the ripple magnitude (*i.e.* smoothing factor SF=~0) was observed. The experimental results are plotted in Fig. 10.

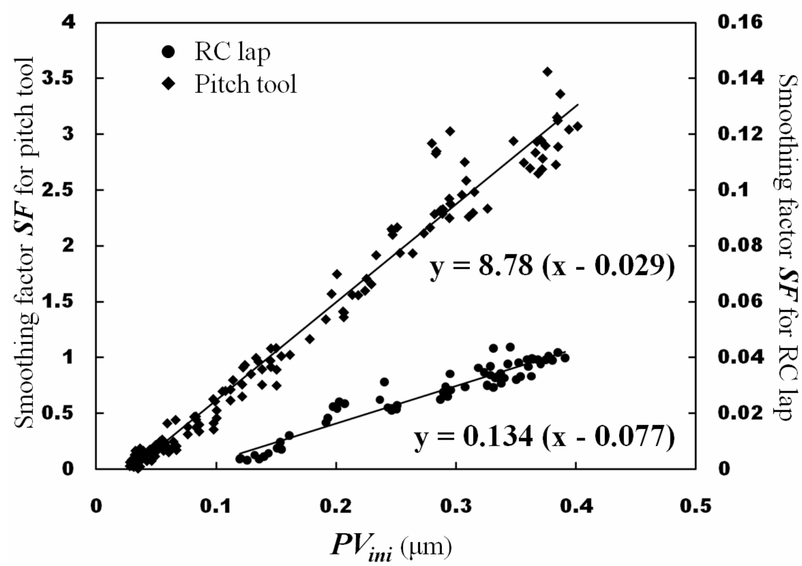

Fig. 10. Measured smoothing factor SF *vs.* initial ripple magnitude P_{ini} for pitch tool and RC lap. (*Note:* The solid line represents the linear fit using the parametric smoothing model. Two parameters C_1 and C_2 were used to fit the measured data as shown in Table. 5.)

Two parameters C_1 and C_2 in the parametric smoothing model were used to fit the measured data as shown in Fig. 10. The first parameter C_1 was used to match the slope of the data. The second parameter C_2 was used to match the x-intercept of the data, which is the parametric representation of the smoothing limit PV_{min} mentioned in Section 2.2.3. The fitted parameter values are presented in Table 5 with the calculated compressive stiffness $\kappa_{elastic}$ values from Eq. (14) and (15). For the storage modulus (*i.e.* Young's modulus) of the pitch tool, a typical value 2.5 GPa was assumed [33]. The actual storage modulus of the pitch is a function of many factors such as the temperature of pitch. This uncertainty becomes a part of the first parameter C_1 in the parametric smoothing model. Also, pitch is practically a solid within the orbital tool motion time scale. Thus, the phase lag δ was assumed as 0. For the RC lap storage modulus E' =0.003GPa and phase lag δ=0 was used. (More detailed calculation procedures for the compressive stiffness $\kappa_{elastic}$ values are provided in Appendix B.)

Table 5. Compressive stiffness $\kappa_{elastic}$ and two parameter values for the smoothing model

	$\kappa_{elastic}$ (Pa/μm)	C_1 (Pa/μm)	C_2 (μm)
Pitch tool	312500	23608	0.029
RC lap	375	3141	0.077

The linear trend predicted by the parametric smoothing model in Eq. (20) was successfully verified. The C_1 for the pitch tool case was much smaller (~0.08 times) than the compressive stiffness $\kappa_{elastic}$ of the pitch, so the slope of the parametric *SF* function was smaller than the slope solely based on the pitch stiffness itself. One possible explanation for this result may be the polishing compound liquid layer between the pitch surface and the workpiece, which may change the total compressive stiffness. However, the pitch tool still shows ~66 times faster (*i.e.* ~66 times steeper *SF* slope) smoothing action than the RC lap. The limiting magnitude of the ripple PV_{min} was measured experimentally and fitted using the second parameter C_2. The pitch tool was able to smooth out the ripples down to PV_{min} =~0.029μm.

In contrast, the C_1 for the RC lap was much larger (~8.4 times) compared to the compressive stiffness of the SP, so the slope of the *SF* graph was almost entirely determined by the compressive stiffness of the SP. This may result from the fact that the contributions to the total stiffness κ_{total} from the thin (0.5mm) polyurethane pad and wrapping material were much smaller than the contribution from the SP. Also, the PV_{min} was measured and fitted using C_2. The RC lap smoothed out the ripples down to PV_{min} =~0.077μm. A steeper slope for faster smoothing action can be achieved by using different non-Newtonian fluids with higher storage modulus value. Also, changing the thickness L of the elastic material is expected to result in a steeper SF function, because $\kappa_{elastic}$ is a direct function of L as shown in Eq. (14). These additional factors as well as the ripple spatial frequency, which changes the applied stress frequency, will be investigated in future studies.

2.3 Parametric Modeling of Edge Effects for TIFs

While a linear Preston's model for material removal allows the TIF to be theoretically determined for most cases, nonlinear removal behavior as the tool runs over the edge of the part introduces a difficulty in modeling the edge TIF. As mentioned in Section 1.3, the linearity for Preston's equation may need to be reconsidered since the edge pressure distribution changes over a wide range of pressure. The linearity of the Preston's model is usually valid for a moderate range of pressure values for a given polishing configuration.

A series of studies and experiments to represent and model the measured TIFs using various tool motions and conditions were conducted in Appendices C, D and E. Theoretical TIF models (for not-overhanging cases) based on the Preston's equation are introduced with measured data in Appendix C. Appendix D provides in-depth study for the edge TIF model development based on measured data. Various TIFs based on the edge TIF model are given as a TIF library in Appendix E. The following Sections 2.3.1-2.3.4 are a summary of articles published in the journal *Optics Express* (Appendices C and D) and SPIE *Proceedings* (Appendix E).

2.3.1 Theoretical TIF model using Preston's equation

The theoretical basis for a new three dimensional polishing simulation technique was developed in Appendix C. The TIF can be calculated using the Preston's equation of material removal, Δz, in Eq. (1).

The theoretical TIF's applicability for polishing simulation was verified by comparing the computer generated (theoretical) TIFs against the measured TIFs in Appendices C and D for various polishing parameters. For instance, the theoretical TIF for the RC lap was calculated. A measured and theoretical static TIF using the 220mm RC lap with an orbital tool motion is shown in Fig. 11.

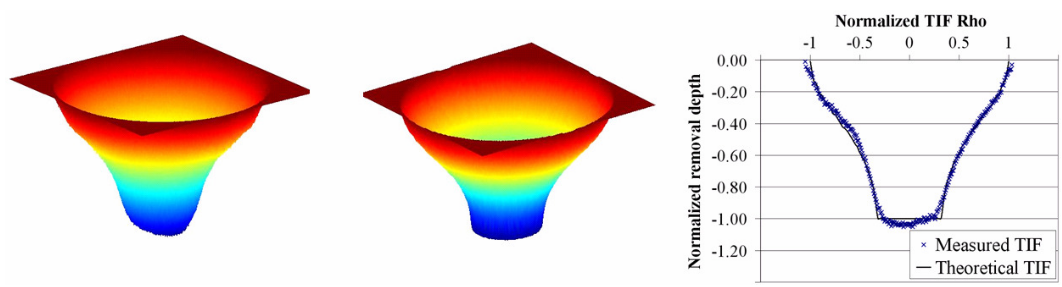

Fig. 11. The TIFs using the RC lap with an orbital tool motion: measured 3D TIF (left), theoretical 3D TIF (middle), and averaged radial profiles of them (right)

The good matching between the measured and theoretical TIFs proves that the removal process can be precisely modeled and predicted. However, once the tool overhangs the edge of workpiece, the measured TIF tends to deviate from the nominal behavior due to dramatically varying pressure range, tool bending, and other non-linear effects.

2.3.2 Parametric edge TIF model

For a given tool motion and pressure distribution under the tool-workpiece contact area, a TIF can be calculated using Eq. (1). The basic edge TIF uses the linear pressure model [5] explained in Appendix D. Two types of tool motion, orbital and spin, were modeled. For the orbital case, the tool orbits around the TIF center with orbital radius, $R_{orbital}$, and does not rotate. For the spin case, the tool rotates about the center of the tool. These tool motions are depicted in Fig. 12. The tool overhang ratio S_{tool} defined in Fig 13 is fixed for the spin tool motion case, but varies as a function of tool position (A~F in Fig. 12 (left)) for the orbital case while the basic edge TIF calculation is being made.

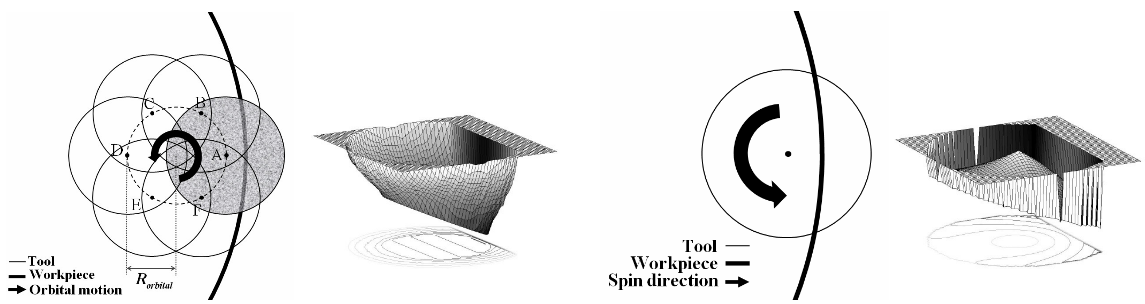

Fig. 12. Orbital (left) and spin (right) tool motion with the basic edge TIF.

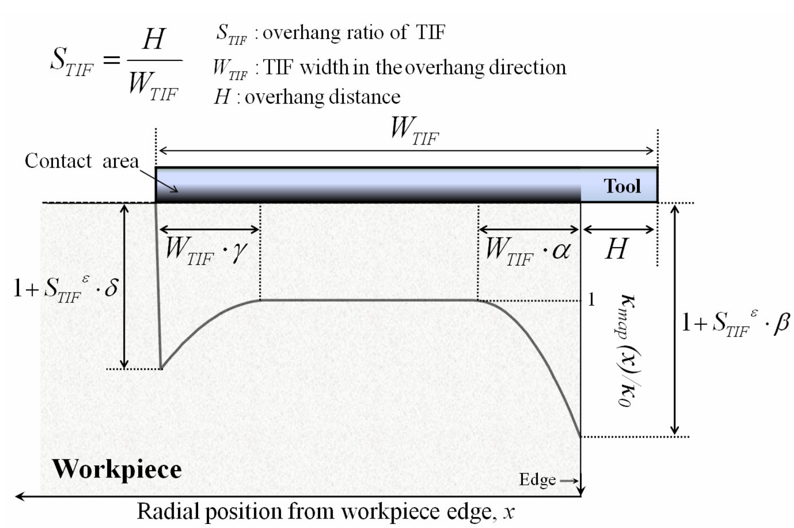

Fig. 13. Degrees of freedom of the κ map (in x-profile) using five parameters.

On top of the basic edge TIF, a new concept using the κ map for the parametric edge TIF model is introduced. The κ map represents the spatial distribution of the Preston coefficient $\kappa(x,y)$ in Eq. (1). It changes as a function of TIF overhang ratio, S_{TIF}, and five function control parameters (α, β, γ, δ and ε). S_{TIF} is defined as the ratio of the overhang distance, H, to the TIF width in the overhang direction, W_{TIF}, in Fig. 13. The TIF width may not be equal to the tool width since it includes the tool motion. For instance, the TIF width is equal to the tool width for the spin motion case. However, for the orbital motion case, the TIF width becomes the sum of the tool width and orbital motion diameter. The parametric edge TIF can be calculated by multiplying the basic edge TIF by the κ map.

The virtue of this parametric κ map approach is that it does not require independent understanding of each and every factor affecting the material removal process. Instead, only the combined net effect of them is represented by the κ map. The κ map is defined by a local coordinate centered at the edge of the workpiece. x represents the radial position from the workpiece edge.

The edge-side high removal, based on the non-linear high pressure distributions near the workpiece edge, is approximated by the first quadratic correction term, f_1, with two parameters, α and β. The first parameter, α, determines the range of the quadratic correction from the edge of the workpiece. The second parameter, β, controls the magnitude of the correction. This degree of freedom using α and β is shown in Fig. 13. This correction is defined analytically as

$$f_1(x,\alpha,\beta) = \frac{\beta}{(W_{TIF} \cdot \alpha)^2} \cdot (x + W_{TIF} \cdot \alpha)^2 \cdot \Theta(x + W_{TIF} \cdot \alpha) \tag{21}$$

where $\Theta(z)$ is the step function; 1 for $z \geq 0$ and 0 for $z<0$.

The second correction term, f_2, defined by Eq. (22) addresses the discrepancy between the simulated removal using the basic edge TIF and the measured removal in the workpiece-center-side region. Similar to f_1, it has two parameters, γ and δ. The third parameter, γ, determines the range of the second correction, and the fourth parameter, δ, controls the magnitude of the correction as shown in Fig. 13.

$$f_2(x,\gamma,\delta) = \frac{\delta}{(W_{TIF}\cdot\gamma)^2}\cdot(-x - W_{TIF} + W_{TIF}\cdot S_{TIF} + W_{TIF}\cdot\gamma)^2 \cdot \Theta(-x - W_{TIF} + W_{TIF}\cdot S_{TIF} + W_{TIF}\cdot\gamma) \quad (22)$$

Using these two correction terms, the κ map is defined in Eq. (23). It is a sum of the first and second correction terms, and includes a fifth parameter, ε. The fifth parameter, ε, was introduced to change the magnitude of the κ map as a function of TIF overhang ratio, S_{TIF}. Larger ε means the required correction magnitude increases faster as the overhang ratio increases.

$$\kappa(x,\alpha,\beta,\gamma,\delta,\varepsilon) = \kappa_0\cdot\{1 + S_{TIF}{}^{\varepsilon}\cdot(f_1 + f_2)\} \quad (23)$$

where κ_0 is the Preston coefficient when there is no overhang.

Some example parametric edge TIFs using the κ map are shown in Table 6. As we increase the overhang ratio, S_{TIF}, non-linearly increasing removal near the workpiece edge is clearly shown as a result of the first correctional term for both the orbital and spin cases. The effects of the second correction are also observed. Due to the opposite signs of δ for the orbital (δ = 20) and spin (δ = -3) cases, in the workpiece-center-side region, there is more and less removal than the basic edge TIF's.

Table 6. Normalized parametric edge TIFs[c]

Tool motion	Overhang ratio, S_{TIF}				Scale
	0	0.1	0.2	0.3	
Orbital	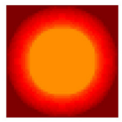	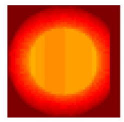	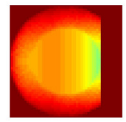	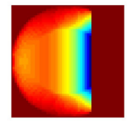	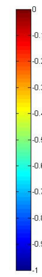
Spin	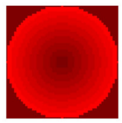	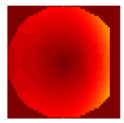	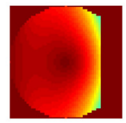	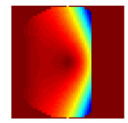	

[c](Orbital: α=0.2, β=4, γ=0.4, δ=20, ε=1.5 / Spin: α=0.4, β=6, γ=0.3, δ=-3, ε=0.9)

2.3.3 Performance of the parametric edge TIF model

The performance of the parametric edge TIF model was evaluated by comparing four different edge TIF models with the measured edge TIFs as shown in Fig. 14. The simulated removal profile based on the nominal TIF model (*i.e.* no edge model) does not follow the overall slope of the measured removal profile. Especially, it shows a large difference in the edge-side removal (x = 0 to -60mm). The computed removal profile using the basic edge TIF model seems to have a closer overall slope to the measured removal. However, two mismatches between the measured and simulated removal are clearly observed in the edge-side and workpiece-center-side regions. The parametric edge TIF model using only the first correction allows us to correct the discrepancy in the edge-side removal. The removal profile based on the parametric edge TIF model using both the first and the second correction is well matched with the experimental removal profile over the whole range of the removal profile.

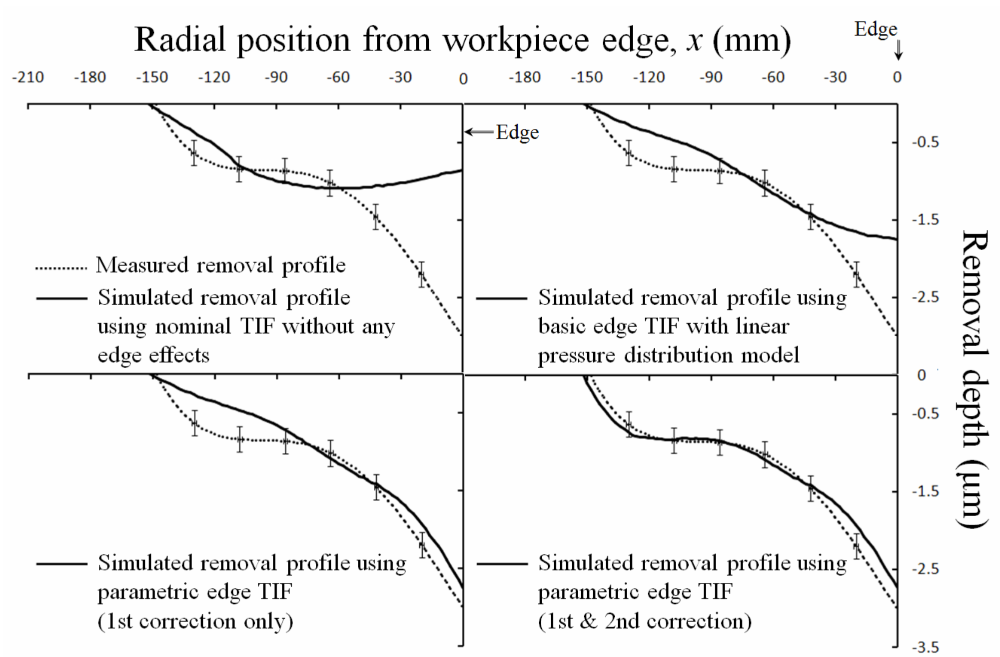

Fig. 14. Measured (with RMS error bars) *vs.* simulated (using different edge TIF models) edge removal profiles for the orbital tool motion case.

We define a normalized fit residual, Δ, as a figure of merit to quantify the performance of the parametric model compared to the data. This is normalized as

$$\Delta = \frac{RMS\ \ of\ (data - model)}{RMS\ \ of\ data} \cdot 100\ (\%)\ \ . \tag{24}$$

This quantitative comparison result is given in Fig. 15. It is clear that the normalized fit residual, Δ, is relatively low (about 10~20%) for all TIF model cases when the overhang ratio is small (S_{TIF}<0.14 for the orbital case and S_{TIF}<0.02 for the spin case). It basically means that there is no difference between nominal and edge TIF models when the overhang effects are negligible. The improvements become significant as the overhang ratio increases. For the orbital tool motion case with S_{TIF} =0.28, the normalized fit residual, Δ, falls to 10% (parametric edge TIF using both corrections) from 52% (nominal TIF), or from 30% (basic edge TIF). For the spin tool motion case with S_{TIF} =0.4, the normalized fit residual, Δ, is dramatically improved to 12% (parametric edge TIF using both corrections) from 87% (nominal TIF), or from 66% (basic edge TIF). The second correction is not really required for the spin tool motion case, in contrast to the orbital tool motion case, where the second correction brought significant improvement.

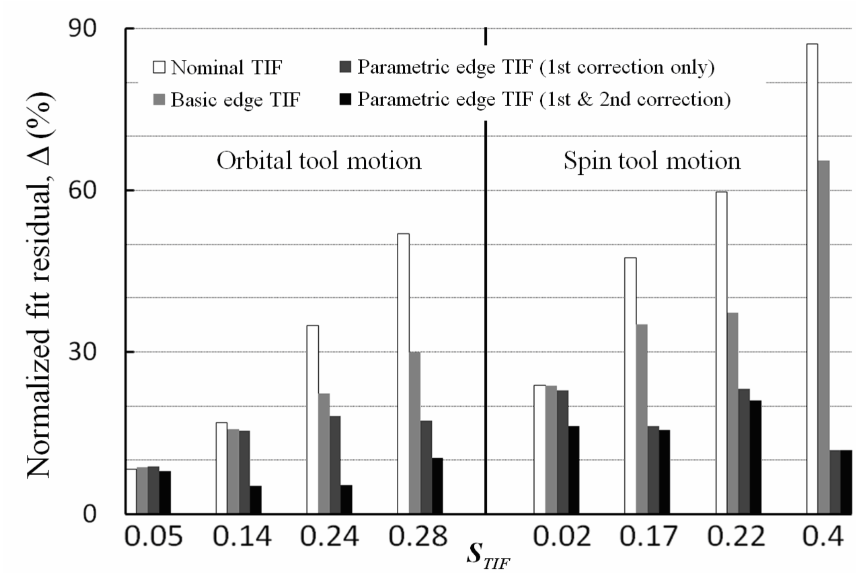

Fig. 15. Normalized fit residual, Δ, of the simulated removal profiles using different TIF models for orbital and spin tool motion cases.

2.3.4 TIF library using the parametric edge TIF model

A TIF library was generated using the parametric TIF model for various tool shapes, tool motions, and tool sizes. The library is provided in Appendices E and F. We assumed the same control parameter values as the experimental cases in Appendix D (Orbital tool motion: α=0.2, β=4, γ=0.4, δ=20, ε=1.5 and Spin tool motion: α=0.4, β=6, γ=0.3, δ=-3, ε=0.9). The relative rotation speed between the tool and workpiece was also varied since it plays an important role to determine the TIF shapes.

2.4 Non-Sequential Optimization Technique using Multiple TIFs and Enhanced Merit Functions

Based on the various TIFs in the TIF library, a non-sequential optimization technique to optimize the CCOS process was developed in Appendix F. Operating CCOS with small tool and very well characterized TIF achieves excellent performance, but it takes a long time. This overall polishing time can be reduced by performing sequential polishing runs that start with large tools and finish with smaller tools. A variation of this technique that uses a set of different size TIFs simultaneously is presented. Also enhanced merit functions are introduced for the optimization technique. The following Sections 2.4.1-2.4.4 are a summary of an article published in the journal *Optics Express*, Appendix F.

2.4.1 Conventional (i.e. sequential) vs. non-sequential optimization technique

For the case of conventional (*i.e.* sequential) CCOS optimization, a single dwell time map for one TIF has been the major search space for the optimal solution. In other words, an optimization engine searches for the optimal dwell time values for a TIF on the workpiece, which gives the best residual error map. After the CCOS run is executed, another (or the same) TIF is used for the next dwell time map optimization to attack the residual error map. This sequential process is repeated, usually using successively smaller tools (*i.e.* TIFs) until the target specification is achieved.

In contrast, the non-sequential optimization approach uses various TIFs in a single optimization, simultaneously. Each TIF has its own dwell time map. Thus, multiple dwell time maps are brought into the non-sequential optimization engine, and optimized to achieve the target removal map. The total removal comes from the combination of all different TIFs and their own dwell time maps. Unlike the conventional technique using TIFs sequentially, different TIFs are used together to support each other in a single optimization. Non-linear optimization allows TIFs with low significance (*i.e.* ignorable dwell time or removal) to be extracted from the TIF library during the optimization. However, the key difference of the non-sequential technique from the conventional one is not the number of utilized TIFs. The conventional case may use as many TIFs as the non-sequential case in sequential manner. The major improvement comes from considering all TIFs at the same time, so that the optimal combinations of TIFs are used in a constructive manner to improve the performance of the CCOS process.

For instance, a large square tool with orbital tool motion may be selected to remove most of the low spatial frequency errors on the workpiece. A small TIF from a circular tool with spin tool motion may be chosen with the large square tool TIF as an optimal set to achieve high figuring efficiency by removing localized small errors. As a result, the mid-spatial frequency error on the workpiece, often caused by the small tool, can be minimized because the small tool was used only for a short time. Some specialized TIFs such as the parametric edge TIFs may be utilized for an edge figuring optimization.

In summary, both conventional and non-sequential optimization techniques can be used to find an optimal dwell time map solution. However, there are significant differences, which make the non-sequential technique more powerful than the conventional one. The optimization engine now has wider search space, including tool shape, tool size, tool motion, and so forth. These various tool configuration parameters were formerly the human's decision in the conventional CCOS technique. Many different combinations of the various TIFs are simulated to find an optimal TIF set. This technical advance leads to improvements in figuring efficiency and mid-spatial frequency error reduction.

2.4.2 Merit functions for the non-sequential optimization technique

The non-sequential optimization technique provides an optimal solution which suppresses the mid-spatial frequency error while still maintaining the high figuring efficiency. In order to find the optimal solution, the merit functions must completely represent the residual error map in terms of the RMS of the error map, mid-spatial frequency error, and newly generated local error features. Also, the computational load for the merit function calculations should be minimized, because the calculations are placed in the optimization loop.

The figure of merit (*FOM*) used for this work combines six different merit functions using RSS (root-sum-square) as follows:

$$FOM_{total} \equiv RSS_{RMS\_errors} = \sqrt{\sum_{i=1}^{6} C_i \cdot FOM_i^{\,2}} \tag{25}$$

where $C_{1\text{-}6}$ are the weighting factors for $FOM_{1\text{-}6}$. Each FOM_i is defined as

$$FOM_1 \equiv RMS\ of\ \ Positive\ Error\ Map = \sqrt{\iint_{M+} \{error\_map(x,y)\}^2\, dxdy \Big/ \iint_{M} dxdy} \tag{26}$$

$$FOM_2 \equiv RMS\ of\ \ Negative\ Error\ Map = \sqrt{\iint_{M-} \{error\_map(x,y)\}^2\, dxdy \Big/ \iint_{M} dxdy} \tag{27}$$

$$FOM_3 \equiv RMS\ of\ \ x\,Slope\ Map = \sqrt{\iint_{M} \{\frac{\partial}{\partial x} error\_map(x,y)\}^2\, dxdy \Big/ \iint_{M} dxdy} \tag{28}$$

$$FOM_4 \equiv RMS\ of\ \ y\,Slope\ Map = \sqrt{\iint_{M} \{\frac{\partial}{\partial y} error\_map(x,y)\}^2\, dxdy \Big/ \iint_{M} dxdy} \tag{29}$$

$$FOM_5 \equiv RMS\ of\ \ x\,Curvature\ \ Map = \sqrt{\iint_{M} \{\frac{\partial^2}{\partial x^2} error\_map(x,y)\}^2\, dxdy \Big/ \iint_{M} dxdy} \tag{30}$$

$$FOM_6 \equiv RMS\ of\ \ y\,Curvature\ Map = \sqrt{\iint_{M} \{\frac{\partial^2}{\partial y^2} error\_map(x,y)\}^2\, dxdy \Big/ \iint_{M} dxdy} \tag{31}$$

where the surface integral limit M represents the error map surface. $M+$ and $M-$ are the error map areas with positive and negative residual error values, respectively. The six weighting factors can be adjusted as design parameters, depending on a specific purpose of a CCOS run.

The RMS deviation of the error map is calculated using FOM_1 and FOM_2. FOM_1 is the RMS of the positive error map, where the final surface is still higher than the target surface. FOM_2 is the RMS of the negative error map, where the final surface is lower than the target surface. Because the polishing process can only remove material from the workpiece, the surface often needs to be kept higher than the target surface to a certain extent during the polishing process. This can be achieved by increasing the weighting factor C_2 for FOM_2. At the final polishing run to finish the project, both FOM_1 and FOM_2

may need to be minimized with the same weightings (C_1=C_2) to minimize the conventional RMS of the error map.

The RMS deviation of the surface slope map (*i.e.* FOM_3 & FOM_4 in Eq. (28) and (29)) and the RMS deviation of the surface curvature map (*i.e.* FOM_5 & FOM_6 in Eq. (30) and (31)) are used to quantify the mid-spatial frequency error and localized small errors. The approaches using Fourier transform or PSD based figure of merits were excluded due to their computing power requirements. In contrast, the differential calculations in FOM_3, FOM_4, FOM_5 and FOM_6 can be easily done for a numerical data set (*e.g.* matrix for a pixelized error map) in most computing language platforms, such as MATLAB™.

The total figure of merit FOM_{total} combines the functions $FOM_{1\text{-}6}$ with appropriate weighting coefficients depending on the purpose of a CCOS run, and provides a good criterion to optimize a CCOS run using a TIF library. For instance, if large C_3 and C_4 values were entered, the optimization engine would try to minimize the slope errors on the final workpiece. By minimizing FOM_{total}, the non-sequential optimization engine prevents the unwanted mid-spatial frequency error and localized small errors, while it achieves a small RMS of the residual error map.

2.4.3 Non-sequential optimization engine

The non-sequential optimization engine was developed using the gradient search (*a.k.a.* steepest descent) method [34]. The method is known as one of the most simple and straightforward optimization technique which works in search spaces of any number of dimensions. This method presupposes that the gradient of the merit function space at a given point can be computed. It starts at a point, and moves to the next point by minimizing a figure of merit along the line extending from the initial point in the direction of the downhill gradient. This procedure is repeated as many times as required. Because the search space for the non-sequential optimization also has multiple dimensions (*i.e.* many TIFs with various tool configuration parameters), the gradient descent method is suitable for our application.

The schematic flow chart for the non-sequential optimization technique is shown in Fig. 16. The TIF library is fed into the non-sequential optimization engine to calculate the optimal dwell time maps for each TIF. In order to calculate the local gradient in the multi-dimensional search space, the optimization engine begins to perturb the dwell time maps, which have a constant value initially. A minimum dwell time is applied during the perturbations to avoid an impractically small dwell time at a position on the workpiece. Because an actual computer controlled polishing machine (CCPM) has its mechanical limitations (*e.g.* maximum acceleration), the minimum dwell time is set by the CCPM specification. The optimization engine evaluates each TIF to achieve the target removal map for all possible TIF locations on the workpiece. For each trial, the change in the total figure of merit FOM_{total} in Section 2.4.2 is recorded to determine the steepest descent case as follows. Using the TIFs with their own dwell time maps for each perturbation case, the expected removal maps are calculated. The difference between the total expected removal map (*i.e.* sum of all expected removal maps from each TIF) and the target removal map is the residual error map. This residual error map is used to evaluate the FOM_{total}. After all TIFs (*i.e.* dimensions of the search space) have been tried, the optimization engine updates the dwell time maps with the optimal trial, which recorded the steepest improvements in FOM_{total}.

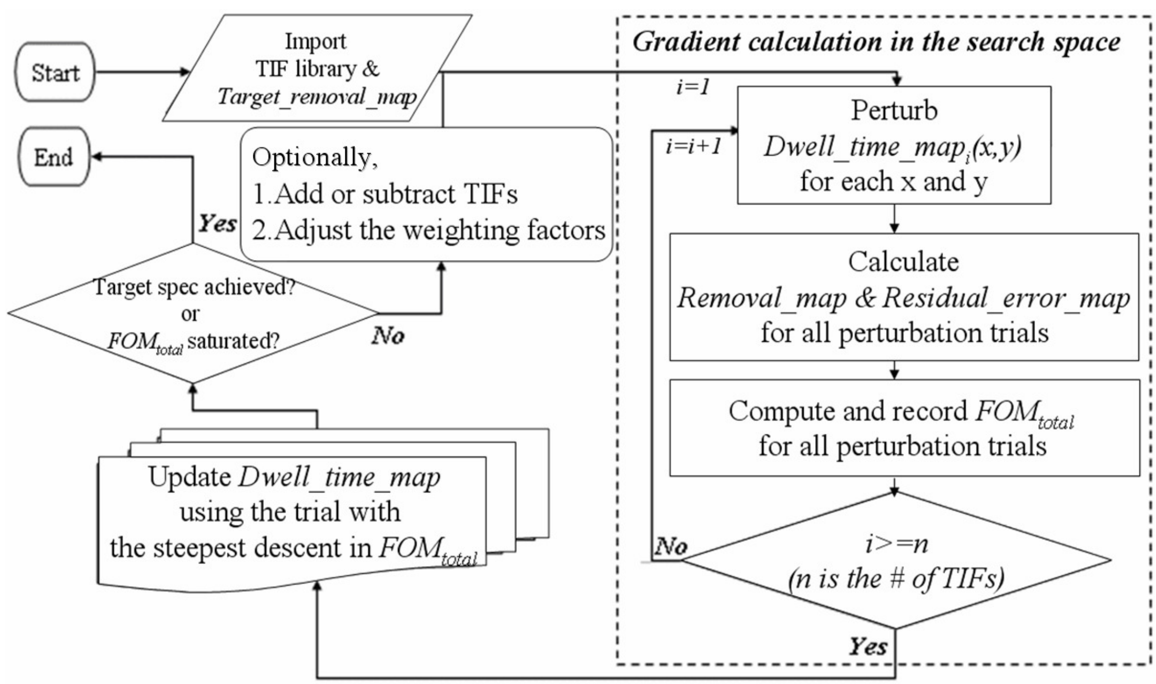

Fig. 16. Flow chart for the non-sequential optimization technique using the gradient descent method

The optimization engine repeats this procedure in a loop until FOM_{total} reaches the specification or does not decrease anymore. The current dwell time maps for each TIF become the optimization result. If these conditions are not met, more TIFs are fed into the TIF library. The TIFs which were hardly used are extracted from the TIF library. By performing more rounds of optimization using the updated TIF library, the optimal TIF set with their dwell time maps is determined eventually.

2.4.4 Performance of the non-sequential optimization technique

2.4.4.1 High figuring efficiency

The figuring efficiency of a CCOS process can be maximized when an optimal TIF set is used for a given target removal. Four cases were simulated to demonstrate the performance of the non-sequential optimization. The figuring efficiency (*FE*) is defined by

$$FE \equiv \frac{RMS_{initial\_error\_map} - RMS_{residual\_error\_map}}{RMS_{initial\_error\_map}} \cdot 100 \qquad [\%]. \tag{32}$$

The advantage of performing the simultaneous optimization was demonstrated by comparing two case studies, Case 1.1 and 1.2. A 1μm piston target removal profile for a 2m radius workpiece was used. The piston target removal is often desired when one tries to remove sub-surface damages on a workpiece without changing the figure of the surface. A TIF using an 84cm circular tool with orbital tool motion was used as a primary TIF to achieve the target removal inside the workpiece edge. An 84cm sector tool was given for a secondary edge TIF. Only these two TIFs were used for both cases for a fair comparison, even though the non-sequential case may use other edge TIF as an optimal set with the primary TIF. The simulation results are presented in Fig. 17.

Case No.	NS mode [d]	Utilized polishing tools (with tool motion) and radial profiles	RMS_{ini}, RMS_{res}, FE [e]
1.1	off (2)	A: 84cm circular tool (orbital), B: 84cm sector tool (orbital) 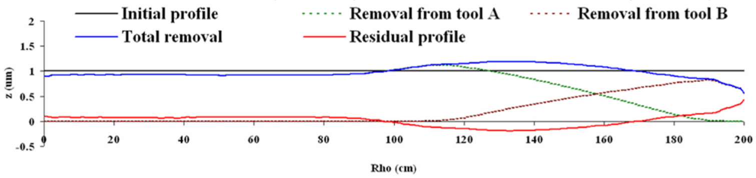	1μm 0.12μm 88%
1.2	on (2)	A: 84cm circular tool (orbital), B: 84cm sector tool (orbital) 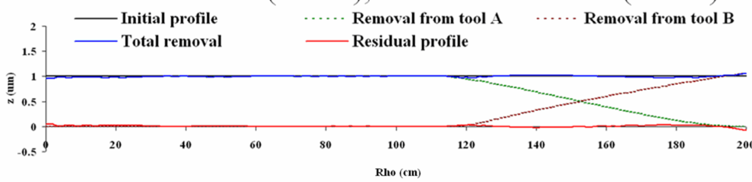	1μm 0.016μm 98.4%
1.3	on (2)	A:30cm circular tool (spin), B:50cm square tool (orbital) 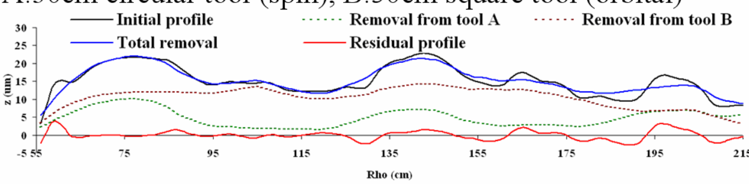	15.71μm 1.30μm 91.7%
1.4	on (5)	A: 20cm circular tool (spin), B: 50cm square tool (orbital) 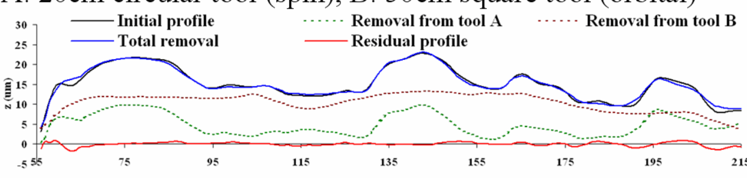	15.71μm 0.50μm 96.8%

[d] NS mode means the non-sequential optimization mode. The number in the parenthesis refers the number of TIFs in the library.
[e] RMS_{ini} and RMS_{res} is the RMS of the initial and residual profile, respectively. FE is the figuring efficiency in Eq. (32).

Fig. 17. Optimization results for Case 1.1-1.4

Case 1.1 did not use the non-sequential optimization technique. The given piston target removal was optimized using the primary TIF first. Then, the residual removal profile was optimized using the secondary edge TIF. The removal profile using the primary TIF (green dotted line in Case 1.1, Fig. 17) removed the target error to the edge as much as possible at the expense of having a bump around 100-120cm radial region. Also, the residual removal profile was not matched well with the removal using the secondary TIF (brown dotted line in Case 1.1, Fig. 17), so that the secondary TIF could not perform its role well. This is because the first optimization using the primary TIF did not consider the possible removal using the secondary TIF in the following optimization. This is a good example to show the fundamental limitation of the sequential approach. Finally, the residual profile shows relatively low figuring efficiency, *FE*=88%, since those two TIFs were not utilized in a constructive manner.

Case 1.2 was optimized using the non-sequential optimization technique, where both the primary and secondary TIFs were considered simultaneously during the optimization process. Thus, the primary TIF intentionally left the edge side error, which was fit with the secondary edge TIF from the 84cm sector tool. As a result, a high figuring efficiency (*FE*=98.4%) was accomplished. The two removal profiles from both TIFs (green and brown dotted lines in Case 1.2, Fig. 17) matched well, so that the total removal (blue solid lines in Case 1.2, Fig. 17) is almost a constant (*i.e.* piston) removal profile. The residual error (red solid line in Case 1.2, Fig. 17) shows flat profile, which is much improved over Case 1.1.

Two more case studies were conducted to show the value of an optimal TIF set. For Case 1.3 and 1.4, a target removal profile for a 4.3m diameter surface was randomly generated. It has a 0.55m in radius circular hole at the center. This profile is shown as black solid lines (*i.e.* initial profile) in Case 1.3 and 1.4, Fig. 17. The TIF from 50cm square tool with orbital tool motion was given as a common primary TIF.

Case 1.3 was optimized using a secondary TIF from a 30cm circular tool with spin tool motion. The TIF library only had these two TIFs (using the 50cm primary square tool and 30cm circular tool), so that the optimization engine was not allowed to use other TIFs. Case 1.3 in Fig. 17 shows the optimized removal profiles using the 30cm circular tool (green dotted line) and the 50cm square tool (brown dotted line), which was not a good TIF set for the given target error profile. As shown in the residual profile (red solid line in Case 1.3, Fig. 17), most of the localized small errors in the target error profile were not removed since the secondary TIF from the 30cm circular tool was too large to remove them. The un-matched TIFs results in the relatively low figuring efficiency (*FE*=91.7%) with hard-to-correct bumpy features on the residual error profile.

Case 1.4 was optimized using five TIFs (using the 50cm primary square tool and 10, 20, 30, 40cm circular tools) in the TIF library. For the direct comparison with Case 1.3 the final number of utilized TIFs was limited to two. As the result of the optimization, a TIF from a 20cm circular tool with spin tool motion was used as the secondary TIF. As you see in the removal profile using the 50cm tool (brown dotted line), the large tool removes most of the low-spatial frequency errors in the target error profile efficiently. Then, the removal profile from the 20cm tool (green dotted line) covers the localized small errors only. Most of the target errors were successfully removed with high figuring efficiency, *FE*=96.8%.

The comparison between Case 1.1 and 1.2 clearly shows the importance of the simultaneous optimization to achieve high figuring efficiency. Also, Case 1.4 highlights the advantage of utilizing an optimal TIF set for a given target removal.

2.4.4.2 Mid-spatial frequency error suppression with high time-efficiency

The performance of the non-sequential optimization technique was evaluated in a two-dimensional simulation of polishing the 1.6m New Solar Telescope (NST) primary mirror [35]. A 1.6m optical surface map with 701nm RMS of irregular errors was simulated as shown in Fig. 18. The target specification for the residual error map was set as <20nm RMS, the NST primary final optical surface specification [35].

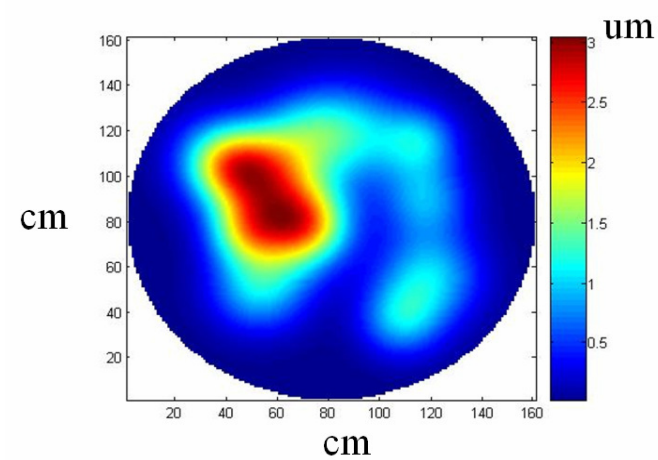

Fig. 18. Randomly generated 1.6m target removal map (surface RMS: 701nm, slope error RMS: 0.522arcsed, error volume: 1.31cm^3)

Due to uncertainties in the actual TIF shapes (including magnitude) and the tool positioning accuracy of the CCPM, the difference between the ideal removal and actual removal tends to produce mid-spatial frequency error (*i.e.* tool marks) on the finished optical surface. Large TIFs, which usually have less total dwell time with shorter tool path, are less sensitive to those uncertainties, so that the residual tool marks are limited. However, small TIFs are required to correct localized small errors. Thus, the key for the mid-spatial frequency error suppression is using the proper size of TIFs for various spatial frequency error components on the workpiece. The non-sequential optimization engine utilizes large and small TIFs for the low-spatial frequency errors and localized small errors, respectively.

For a realistic polishing simulation, we assumed random positioning errors and TIF magnitude variation. Tool positioning error of up to 0.5% of the workpiece size was used. This positioning error may come from a measured target removal map which may have errors in absolute coordinates, or a limited positioning accuracy of the CCPM itself. Up to ±2.5% random variation in the TIF magnitude was applied during the simulations. This variation is a function of TIF stability, which is a characteristic of each tool. An actual laboratory environment may cause other errors which may degrade the simulation result. The simulation parameters are listed in Table 7.

Table 7. Parameters for the polishing simulation

Parameter	Values	Note
Target form accuracy	<20nm RMS	NST Spec. [35]
Available tool sizes	100~300mm	Circular tools
Variation of TIF magnitude	±2.5%	
Positioning error	±4mm	0.5% of 1.6m

Three simulations were compared to show the performance of the non-sequential optimization technique in suppressing the mid-spatial frequency error. For the first two cases, Cases 2.1 and 2.2, the non-sequential optimization technique was not used. Only a single TIF from the largest tool (300mm in diameter) or the smallest tool (100mm in diameter) was used during the polishing simulations. Case 2.3 utilized multiple TIFs simultaneously. The residual error maps and optimization results are summarized in Fig. 19 and Table 8. (These simulation results are provided as movie clips, Media 1-3, in Appendix F.)

The largest TIF, Case 2.1, left localized small errors on the final surface as shown in Fig. 19. There was a limitation caused by the small features (>3cycles/m in the PSD graph) which were smaller than the TIF size. In contrast, for the Case 2.2, almost 99.5% of the form error volume was removed using the smallest TIF. However, it caused significant mid-spatial frequency error on the final optical surface. This is easily observed by comparing the initial and final PSD graphs in Case 2.2, Fig. 19. Even though the low-spatial frequency errors (<5 cycles/m) were removed, there was a significant generation of mid-spatial frequency error (5-30 cycles/m). As a result, the final RMS slope error was 0.277arcsec which was the worst among three cases in Table 8.

The non-sequential optimization result, Case 2.3, showed the best performance in terms of both preventing the mid-spatial frequency error and achieving the high figuring efficiency. The optimization engine used four different TIF diameters, 100, 140, 210 and

300mm, among the available TIF sizes between 100 and 300mm. The PSD graph (in Case 2.3, Fig. 19) shows good suppression (*i.e.* no increase from the initial PSD) in the mid-spatial frequency range (5- 30cycles/m) during the polishing process. The final surface had 0.057arcsec RMS slope variation and 10nm RMS surface irregularity, which meets the target specification. About 99.6% of the initial error volume was removed.

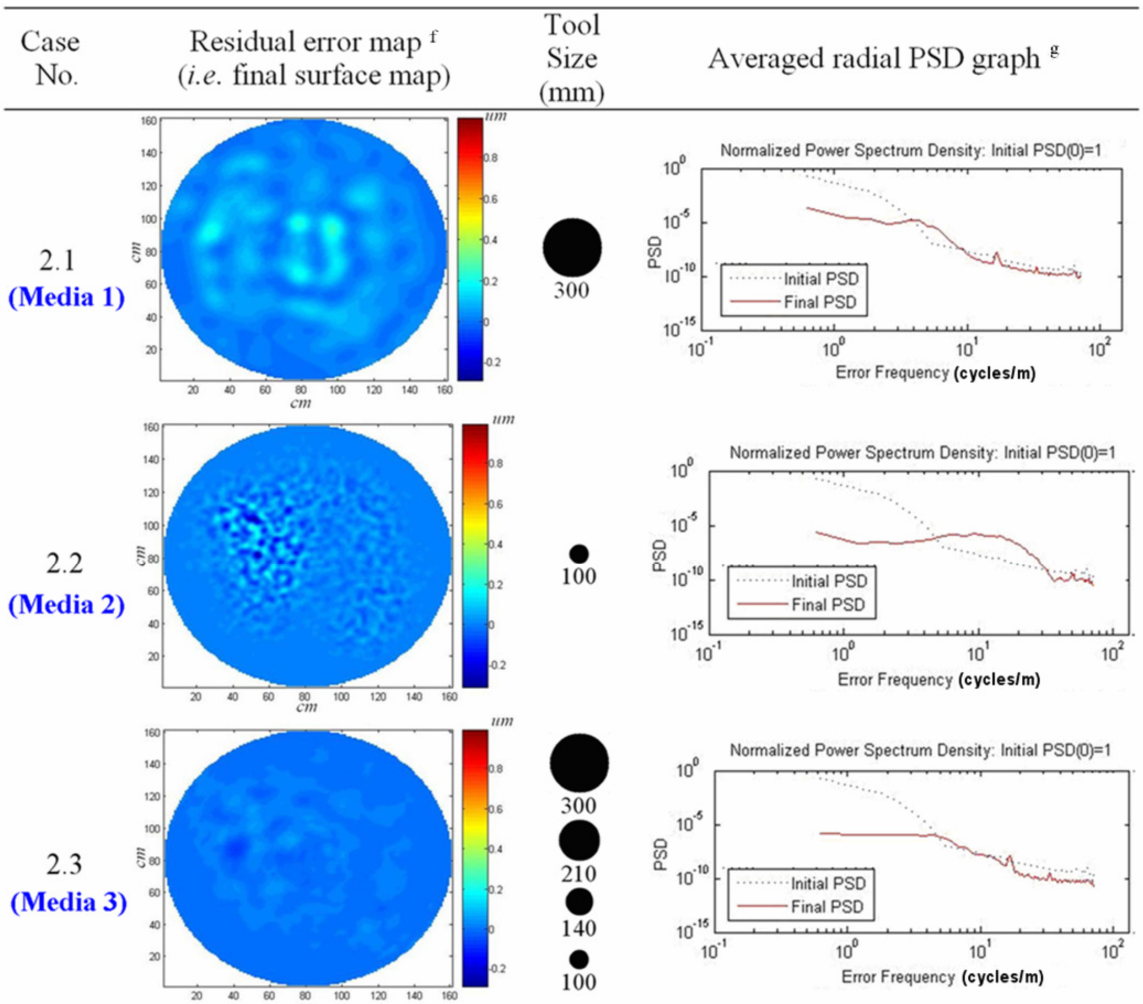

[f] The accompanying movie clips (Media 1-3) show the evolution of the optical surface during the polishing process.
[g] The PSD is unitless due to the normalization.

Fig. 19. Three simulation results for 1.6m NST target removal map

This demonstrates that the non-sequential optimization technique successfully balanced between various size TIFs by selecting the large TIFs for most of the error volume and the small TIFs only for the localized small errors. The final surface error map is shown in Case 2.3, Fig. 19.

Table 8. Surface errors before and after polishing process for Case 2.1-2.3 [h]

Case No.	Initial surface errors (*i.e.* target error map spec.)			Final surface errors (*i.e.* residual error map spec.)			Total polishing time (unit time [i])
	Surface error RMS (nm)	Slope error RMS (arcsec)	Error volume (cm^3)	Surface error RMS (nm)	Slope error RMS (arcsec)	Error volume (cm^3)	
2.1	701	0.522	1.31	36 *94.9%*	0.1 *80.8%*	0.072 *94.5%*	82
2.2	701	0.522	1.31	31 *95.6%*	0.277 *46.9%*	0.006 *99.5%*	774
2.3	701	0.522	1.31	10 *98.6%*	0.057 *89.1%*	0.005 *99.6%*	100

[h] Percentage in *italics* represents the improvement ratio with respect to the initial surface specification for the surface error RMS, slope error RMS, and error volume. This is same as the figuring efficiency *FE* for the surface error RMS case.

[i] The 'unit time' was used for the relative comparison between cases.

As shown in Table 8, the total polishing time for non-sequential optimization Case 2.3 (100 unit time) was much smaller compared to the 774 unit time of Case 2.2. While both Case 2.1 and 2.3 show significantly shorter total polishing time, Case 2.3 which used multiple TIFs resulted in superior performance. Thus, the non-sequential optimization technique provides a time-efficient CCOS process with both high figuring efficiency and good mid-spatial frequency error suppression.

3. CONCLUDING REMARKS

Extensive studies and experimental demonstrations were performed to develop next generation CCOS processes. The RC lap (*i.e.* polishing tool) using visco-elastic non-Newtonian fluids was developed. The RC lap has the advantages of both rigid and compliant tools for different time scales. It can be used just like a rigid tool, which has natural smoothing effects, for relatively fast tool motion (*e.g.* orbital) time scales. As it moves along the tool path on a workpiece, the non-Newtonian fluid flows to fit the slowly varying local curvatures under the tool. Highly deterministic TIFs and removal rate were experimentally demonstrated. The measured data showed TIF stability of <10% and superb surface finish with <10Å roughness on a ULE substrate. In addition to its good performance, the ease with which a large tool can be made in a cost-effective manner makes the RC lap an attractive solution for large aspheric precision optics manufacturing.

In order to quantitatively describe the smoothing characteristics of the RC lap, the parametric smoothing model based on the Bridging model and dynamic modulus of visco-elastic materials was introduced. The smoothing effect which naturally removes mid-to-high spatial frequency errors on the workpiece by rubbing the highs of ripples with high pressure was modeled and verified with experiments. This smoothing model may greatly enhance the CCOS convergence rate by predicting the smoothing effects in a CCOS simulation. The smoothing effect of the RC lap was experimentally measured and compared with the conventional pitch tool case. The measured data successfully demonstrated the validity of the parametric smoothing model.

A general concept to generate theoretical TIFs based on the Preston's equation was introduced. This TIF model was further developed to describe a non-linear edge removal process using a parametric edge TIF model. Unlike other approaches using analytical pressure distributions to develop edge TIF models, we used a parametric approach using a κ map, which represents the spatial distribution of the Preston coefficient. In this way, we were able to express the net effects of many entangled factors affecting the edge removal process in terms of a parametric κ map. Experimental verification was successfully performed. The normalized fit residual, Δ, for the simulated removal using the parametric edge TIF model stayed in the 5~20% range for all overhang cases, which allows us to correct about 80% of the surface errors (with an assumption that everything else is ideal) in a single CCOS process using the parametric edge TIFs. It means that more than 99% of the initial surface errors can be corrected in 3 CCOS runs. Improvement in convergence rate for the residual surface form error is directly related to more efficient time management and lower cost for large optics fabrication projects. Also the TIF library based on the parametric edge TIF model was provided. This parametric edge TIF library can be used to optimize (or simulate) the edge figuring processes.

Using the TIF library which accurately represents the measured TIFs, a non-sequential optimization technique utilizing multiple TIFs was developed and its performance was demonstrated. This technique benefits from the use of a wider search space (including the tool shape, tool size, and so forth) than that of conventional optimization techniques. As the optimization was modified from the classical method to the comprehensive non-sequential algorithm, the performance improvement was significant. For representative polishing runs we showed figuring efficiency *FE* improvement from ~88% to ~98% in terms of residual RMS surface error. Also, the simulations showed that a CCOS process equipped with the new optimization technique effectively suppressed the mid-spatial frequency error. About 89% reduction in the slope error RMS was successfully demonstrated in the simulation. The high time-efficiency (*i.e.* short polishing time) of the CCOS process using the new technique was also demonstrated. The CCOS aided with this new optimization technique enables mass fabrication processes for high quality optical surfaces.

These new advanced techniques and approaches including the RC lap, parametric models for the smoothing effect and edge removal effect, and non-sequential optimization technique, provide more degrees of freedom to tailor a CCOS process according to a given purpose. For instance, a highly aspheric large optical surface can be fabricated using only a few different sizes of RC laps, without tool-workpiece misfit. Since the RC lap's smoothing effects and TIFs were well characterized, highly deterministic CCOS runs including the edge figuring can be performed. Thus, these enhanced features promise not only superb final optical surface qualities, but also improved convergence rate. Also, the non-sequential optimization technique, which fully utilizes these wider degrees of freedom, simulates and optimizes CCOS runs using the enhanced merit functions. The total polishing time and mid-spatial frequency errors can be effectively controlled.

Some interesting future work is suggested from the results of this dissertation. In order to improve the smoothing effects of the RC lap, placing a locally stiff plate between the contacting interface and visco-elastic material may open new possibilities for more customizable RC laps. Trying some other visco-elastic non-Newtonian fluids will be interesting, too. Verifying the additional modalities for the parametric smoothing model in Section 2.2.4 will be another research topic. For instance, performing more smoothing experiments for different elastic material thickness or applied stress frequencies may further develop the presented smoothing model. For the edge TIF modeling, more experimental data using various tool types will provides a useful look-up table with sets of parameter values for different tool types. For instance, edge removal using a pitch tool backed with rigid aluminum plate may be well described with certain parameter values in the edge TIF model. Also, as briefly mentioned in Appendix F, we acknowledge the possibility of undesired optimization results from the non-sequential technique. For example, the total *FOM* is not a linear function in the search space (*i.e.* optimization parameter space), and TIFs are not orthogonal functions. Consequently, the sequential application of TIFs for the optimization engine may not lead to the global minimum, but to a local minimum. Finding a more rigorous global optimization algorithm will be a valuable work package. Another important topic for the process control intelligence is the tool path optimization. This was briefly investigated in another article (with conference presentation) [36]. The current optimization techniques usually provide a dwell time map. However, in practice, a dwell time map can be realized in many possible tool paths. Depending on the tool path optimization, the actually realized dwell time map may be more robust against various environmental errors such as tool positioning tolerance. Future work would find the best compromise between the ideal dwell time map and the practically executable dwell time map including real tolerances.

Finally, the advanced CCOS process using the components and techniques developed in this dissertation will contribute to the realization of the next generation optical systems, which usually have hundreds of precision aspheric optical surfaces (*e.g.* Thirty Meter Telescope [10], European ELT [11] and Laser Inertial Fusion Engine [12]) or state-of-the-art large off axis mirrors (*e.g.* Giant Magellan Telescope [13]).

REFERENCES

1. R. A. Jones, "Computer control for grinding and polishing," Photonics Spectra, 34-39 (August 1963).

2. R. Aspden, R. McDonough, and F. R. Nitchie, Jr, "Computer assisted optical surfacing," Applied Optics. **11,** 2739-2747 (1972).

3. R. E. Wagner and R. R. Shannon, "Fabrication of aspherics using a mathematical model for material removal," Applied Optics. **13,** 1683-1689 (1974).

4. R. A. Jones, "Computer-controlled polishing of telescope mirror segments," Optical Engineering. **22,** 236-240 (1983).

5. R. A. Jones, "Computer-controlled optical surfacing with orbital tool motion," Optical Engineering. **25,** 785-790 (1986).

6. J. R. Johnson and E. Waluschka, "Optical fabrication-process modeling-analysis tool box," in *Manufacturing and metrology tooling for the Solar-A Soft X-Ray Telescope*, W.R. Sigman, L.V. Burns, C.G. Hull-Allen, A.F. Slomba, and R.G. Kusha, eds., Proc. SPIE **1333,** 106-117 (1990).

7. D. D. Walker, D. Brooks, A. King, R. Freeman, R. Morton, G. McCavana, and S.W. Kim, "The 'Precessions' tooling for polishing and figuring flat, spherical and aspheric surfaces", Opt. Express, **11**, 958-964 (2003).

8. H. M. Pollicove, E. M. Fess, and J. M. Schoen, "Deterministic manufacturing processes for precision optical surfaces," in *Window and Dome Technologies VIII*, R. W. Tustison, eds., Proc. SPIE **5078**, 90-96 (2003).

9. J. H. Burge, S. Benjamin, D. Caywood, C. Noble, M. Novak, C. Oh, R. Parks, B. Smith, P. Su, M. Valente, and C. Zhao, "Fabrication and testing of 1.4-m convex off-axis aspheric optical surfaces," in Optical Manufacturing and Testing VIII, J. H. Burge; O. W. Fähnle and R. Williamson, eds., Proc. SPIE 7426, 74260L1-12 (2009).

10. J. Nelson and G. H. Sanders, "The status of the Thirty Meter Telescope project," in *Ground-based and Airborne Telescopes II*, L. M. Stepp and R. Gilmozzi, eds., Proc. SPIE **7012**, 70121A1-18 (2008).

11. A. Ardeberg, T. Andersen, J. Beckers, M. Browne, A. Enmark, P. Knutsson and M. Owner-Petersen, “From Euro50 towards a European ELT,” in *Ground-based and Airborne Telescopes*, L. M. Stepp, eds., Proc. SPIE **6267**, 626725 1-10 (2006).

12. A. Heller, “Safe and sustainable energy with LIFE” (2009), https://str.llnl.gov/AprMay09/pdfs/05.09.02.pdf.

13. M. Johns, “The Giant Magellan Telescope (GMT),” in *Extremely Large Telescopes: Which Wavelengths?*, T. E. Andersen, eds., Proc. SPIE **6986**, 698603 1-12 (2008).

14. D. D. Walker, A. P. Doel, R. G. Bingham, D. Brooks, A. M. King, G. Peggs, B. Hughes, S. Oldfield, C. Dorn, H. McAndrews, G. Dando, and D. Riley, “Design Study Report: The Primary and Secondary Mirrors for the Proposed Euro50 Telescope” (2002), http://www.zeeko.co.uk/papers/dl/New%20Study%20Report%20V%2026.pdf.\

15. T. Andersen, A. L. Ardeberg, J. Beckers, A. Goncharov, M. Owner-Petersen, H. Riewaldt, R. Snel, and D. Walker, “The Euro50 Extremely Large Telescope,” in *Future Giant Telescopes*, J.R.P. Angel and R. Gilmozzi, eds., Proc. SPIE **4840**, 214-225 (2003).

16. R. E. Parks, “Specifications: Figure and Finish are not enough,” in *An optical Believe It or Not: Key Lessons Learned*, M. A. Kahan, eds., Proc. SPIE **7071**, 70710B1-9 (2008).

17. J. M. Hill, “Optical Design, Error Budget and Specifications for the Columbus Project Telescope,” in *Advanced Technology Optical Telescopes IV*, L. D. Barr, eds., Proc. SPIE **1236**, 86-107 (1990).

18. M. T. Tuell, “Novel tooling for production of aspheric surfaces,” M.S. Thesis (2002).

19. N. J. Brown and R. E. Parks, “The polishing-to-figuring transition in turned optics,” SPIE’s 25th Annual International Technical Symposium, (SPIE, 1981).

20. P. K. Mehta and P. B. Reid, “A mathematical model for optical smoothing prediction of high-spatial frequency surface errors,” in *Optomechanical Engineering and Vibration Control*, E. A. Derby, C. G. Gordon, D. Vukobratovich, P. R. Yoder Jr., and C. H. Zweben, eds., Proc. SPIE **3786**, 447 (1999).

21. M. T. Tuell, J. H. Burge, and B. Anderson, “Aspheric optics: smoothing the ripples with semi-flexible tools,” Opt. Eng., **41**, 1473-1474 (2002).

22. Luna-Aguilar E., Cordero-Davila A., Gonzalez Garcia J., Nunez-Alfonso M., Cabrera-Pelaez V.H., Robledo-Sanchez C., Cuautle-Cortez J., and Pedrayes-Lopez M. H., “Edge effects with Preston equation,” Proc. SPIE **4840**, 598-603 (2003).

23. Alberto Cordero-Davila, Jorge Gonzalez-Garcia, Maria Pedrayes-Lopez, Luis Alberto Aguilar-Chiu, Jorge Cuautle-Cortes, and Carlos Robledo-Sanchez, "Edge effects with the Preston equation for a circular tool and workpiece," Appl. Opt. **43**, 1250-1254 (2004).

24. A. P. Bogodanov, "Optimizing the technological process of automated grinding and polishing of high-precision large optical elements with a small tool," Sov. J. Opt. Technol. **52**, 409-413 (1985).

25. C. L. Carnal, C. M. Egert and K. W. Hylton, "Advanced matrix-based algorithms for ion beam milling of optical components," in *Current Developments in Optical Design and Optical Engineering II*, R. E. Fischer and W. J. Smith, eds., Proc. SPIE **1752**, 54-62 (1992).

26. M. Negishi, M. Ando, M. Takimoto, A. Deguchi, and N. Nakamura, "Studies on super-smooth polishing (2nd report)," J. Jpn. Soc. Precis. Eng. **62**, 408-412 (1996).

27. H. Lee and M. Yang, "Dwell time algorithm for computer-controlled polishing of small axis-symmetrical aspherical lens mold," Optical Engineering. **40,** 1936-1943 (2001).

28. R. P. Chhabra and J. F. Richardson, *Non-Newtonian Flow and Applied Rheology (2nd edition)* (Elsevier Ltd, 2008), Chap. 1.

29. R. E. Parks, "Alignment of off-axis conic mirrors," in *Optical Fabrication and Testing*, OSA Technical Digest Series (Optical Society of America, 1980), paper TuB4.

30. Bellofram Corporation, "Bellofram rolling diaphragm design manual" (2009), http://www.atcdiversified.com/Diaphragm/PDF/design_manual.pdf.

31. M. A. Meyers and K. K. Chawla, *Mechanical Behavior of Materials (2nd edition)* (Cambridge University Press, 2009), 124-125.

32. A. C. Fischer-Cripps, "Multiple-frequency dynamic nanoindentation testing," J. Mater. Res. **19,** 2981-2988 (2004).

33. N. J. Brown, "Optical polishing pitch," in *Optical Fabrication and Testing*, Optical Society of America Workshop (Optical Society of America, 1977).

34. W. H. Press, B. P. Flannery, S. A. Teukolsky and W. T. Vetterling, *Numerical recipes in C* (Cambridge, 1988).

35. P. R. Goode, C. J. Denker, L. I. Didkovsky, J. R. Kuhn, and H. Wang, "1.6 m Solar Telescope in Big Bear – the NST," Journal of the Korean Astronomical Society. **35**, 1-8 (2002).

36. D. W. Kim, J. H. Burge and S. W. Kim, "Optimization of Bulged Precessing Tool Polishing for Efficient Mass-Fabrication of Large Optical Surfaces," in *Frontiers in Optics 2005/Laser Science XXI* (Optical Society of America, Washington, DC), **FTuS2** (2005).

APPENDIX A

Rigid Conformal Polishing Tool using Non-linear Visco-elastic Effect

Dae Wook Kim and James H. Burge

Journal article submitted to ***Optics Express***

2009

Copyright Transfer Agreement

The Optical Society of America considers this requested use of its copyrighted materials to be allowed under the OSA Author Agreement submitted by the requester on acceptance for publication of his/her manuscript. It is requested that a complete citation of the original material be included in any publication.

Delois Millner November 25, 2009
Delois Millner Date
Authorized Agent, Optical Society of America

Rigid conformal polishing tool using non-linear visco-elastic effect

Dae Wook Kim[1,*] and James H. Burge[1]

[1]*College of Optical Sciences, University of Arizona, 1630 E. University Blvd, Tucson, Arizona 85721, USA*
[*]*letter2dwk@hotmail.com*

Abstract: Computer controlled optical surfacing (CCOS) relies on a stable and predictable tool influence function (TIF), which is the shape of the wear function created by the machine. For a polishing lap, which is stroked on the surface, both the TIF stability and surface finish rely on the polishing interface maintaining intimate contact with the workpiece. Pitch tools serve this function for surfaces that are near spherical, where the curvature has small variation across the part. The rigidity of such tools provides natural smoothing of the surface, but limits the application for aspheric surfaces. Highly flexible tools, such as those created with an air bonnet or magnetorheological fluid, conform to the surface, but lack intrinsic stiffness, so they provide little natural smoothing. We present a rigid conformal polishing tool that uses a non-linear visco-elastic medium (*i.e.* non-Newtonian fluid) that conforms to the aspheric shape, yet maintains stability to provide natural smoothing. The analysis, design, and performance of such a polishing tool is presented, showing TIF stability of <10% and providing surface finish with <10Å roughness.

OCIS codes: (220.0220) Optics design and fabrication; (220.4610) Optics fabrication; (220.5450) Polishing

References and links

1. R.A. Jones, "Computer control for grinding and polishing," Photonics Spectra, 34-39 (August 1963).
2. R. E. Wagner and R. R. Shannon, "Fabrication of asphberics using a mathematical model for material removal," Applied Optics. **13,** 1683-1689 (1974).
3. R.A. Jones, "Computer-controlled polishing of telescope mirror segments," Optical Engineering. **22,** 236-240 (1983).
4. D.D. Walker, D. Brooks, A. King, R. Freeman, R. Morton, G. McCavana, and S.W. Kim, "The 'Precessions' tooling for polishing and figuring flat, spherical and aspheric surfaces," Opt. Express, **11**, 958-964 (2003).
5. H. M. Pollicove, E. M. Fess, and J. M. Schoen, "Deterministic manufacturing processes for precision optical surfaces," in *Window and Dome Technologies VIII*, R. W. Tustison, eds., Proc. SPIE **5078**, 90-96 (2003).
6. J. H. Burge, S. Benjamin, D. Caywood, C. Noble, M. Novak, C. Oh, R. Parks, B. Smith, P. Su, M. Valente, and C. Zhao, "Fabrication and testing of 1.4-m convex off-axis aspheric optical surfaces," in *Optical Manufacturing and Testing VIII*, J. H. Burge; O. W. Fähnle and R. Williamson, eds., Proc. SPIE **7426**, 74260L1-12 (2009).
7. C. L. Carnal, C. M. Egert and K. W. Hylton, "Advanced matrix-based algorithms for ion beam milling of optical components," in *Current Developments in Optical Design and Optical Engineering II*, R. E. Fischer and W. J. Smith, eds., Proc. SPIE **1752**, 54-62 (1992).
8. H. Lee and M. Yang, "Dwell time algorithm for computer-controlled polishing of small axis-symmetrical aspherical lens mold," Optical Engineering. **40,** 1936-1943 (2001).
9. D.W. Kim, S.W. Kim and J. H. Burge, "Non-sequential optimization technique for a computer controlled optical surfacing process using multiple tool influence functions," Optics Express. (to be published).
10. M. T. Tuell, "Novel tooling for production of aspheric surfaces," M.S. Thesis (2002).
11. R.P. Chhabra and J.F. Richardson, *Non-Newtonian Flow and Applied Rheology (2nd edition)* (Elsevier Ltd, 2008), Chap. 1.

12. Don Loomis, Bob C. Crawford, Norm Schenck, and Bill Anderson, Optical Engineering and Fabrication Facility, University of Arizona, 1630 E. University Blvd, Tucson, Arizona 85721, (personal communication, 2009).
13. M. A. Meyers and K. K. Chawla, *Mechanical Behavior of Materials (2nd edition)* (Cambridge University Press, 2009), 124-125.
14. A. C. Fischer-Cripps, "Multiple-frequency dynamic nanoindentation testing," J. Mater. Res. **19,** 2981-2988 (2004).
15. D. W. Kim, College of Optical Sciences, University of Arizona, 1630 East University Boulevard, Tucson, AZ 85721, and J. H. Burge are preparing a manuscript to be called "Parametric smoothing model for rigid conformal lap using visco-elastic effect."
16. M. Johns, "The Giant Magellan Telescope (GMT)," in *Extremely Large Telescopes: Which Wavelengths?*, T. E. Andersen, eds., Proc. SPIE **6986**, 698603 1-12 (2008).
17. H. M. Martin, D. S. Anderson, J. R. P. Angel, R. H. Nagel, S. C. West, and R. S. Young, "Progress in the stressed-lap polishing of a 1.8-m f/1 mirror," in *Advanced Technology Optical Telescopes IV*, L. D. Barr, eds., Proc. SPIE **1236**, 682-690 (1990).
18. D.W. Kim, W.H. Park, S.W. Kim and J.H. Burge, "Parametric modeling of edge effects for polishing tool influence functions," Optics Express. **17,** 5656-5665 (2009).
19. D.W. Kim, W.H. Park, S.W. Kim and J.H. Burge, "Edge tool influence function library using the parametric edge model for computer controlled optical surfacing," in *Optical Manufacturing and Testing VIII*, J. H. Burge; O. W. Fähnle and R. Williamson, Proc. SPIE **7426**, 74260G1-12 (2009).
20. R. E. Parks, "Alignment of off-axis conic mirrors," in *Optical Fabrication and Testing*, OSA Technical Digest Series (Optical Society of America, 1980), paper TuB4.
21. Bellofram Corporation, "Bellofram rolling diaphragm design manual" (2009), http://www.atcdiversified.com/Diaphragm/PDF/design_manual.pdf.
22. S. Benjamin, Optical Engineering and Fabrication Facility, University of Arizona, 1630 E. University Blvd, Tucson, Arizona 85721, (personal communication, 2009).
23. J. H. Burge, College of Optical Sciences, University of Arizona, 1630 East University Boulevard, Tucson, AZ 85721, is preparing a manuscript to be called "High speed polishing lap for efficient computer controlled optical surfacing."
24. J. Nelson and G. H. Sanders, "The status of the Thirty Meter Telescope project," in *Ground-based and Airborne Telescopes II*, L. M. Stepp and R. Gilmozzi, eds., Proc. SPIE **7012**, 70121A1-18 (2008).
25. A. Heller, "Safe and sustainable energy with LIFE" (2009), https://str.llnl.gov/AprMay09/pdfs/05.09.02.pdf.

---

1. Introduction

Various computer controlled optical surfacing (CCOS) processes have been developed since the 1960s [1-6]. CCOS processes can provide good solutions for fabrication of precision optics because of their high convergence rate based on deterministic removal processes. Many large aspheric optical surfaces and off-axis segments have been successfully fabricated using these techniques [4-6].

Most CCOS processes are based on three main components, i) a numerically controlled (NC) polishing machine, ii) embedded process control intelligence (*i.e.* process optimization software) and iii) a polishing tool. The NC polishing machine provides a stable and repeatable control environment to move the polishing tool on a workpiece. The embedded process control intelligence designs polishing run parameters, such as tool rpm, tool pressure, and dwell time map (*i.e.* tool ablation time as a function of tool position on a workpiece) to achieve a target removal (*e.g.* measured surface error) map. For an optimal polishing run, there have been many studies about optimization techniques used in embedded intelligence [7-9]. The last component, the polishing tool, makes the actual contact and removes material from the workpiece.

In general, a dwell time map is the main optimization result from the process control intelligence to achieve a given target removal map. This optimization is mainly based on a de-convolution process of the target removal map using a tool influence function (TIF). The TIF is the instantaneous material removal under the polishing tool for a given tool motion. Then, the control intelligence uses the TIF as a building block to achieve the target removal map by spatially distributing and accumulating the TIF blocks on the workpiece. Thus, having a well defined (*i.e.* stable and deterministic) TIF is a critical element for a successful CCOS process.

The TIF is a direct function of tool properties, such as pressure distribution under the tool, tool contact area shape, tool motion, and so forth. Thus, developing a well-behaved tool is an essential component to achieve a deterministic TIF. Tool development for aspheric (or freeform) optics production is an especially complex problem. Because local curvatures of an aspheric surface vary as a function of position on a workpiece, a tool with a rigid surface shape cannot be used. Instead, flexibility is required to maintain good contact with the workpiece surface, and not leave zones in the workpiece surface figure due to the tool-workpiece misfit. However, the smoothing effect that automatically compensates for high spatial frequency errors on the workpiece by a rigid tool hitting high portions with higher pressure on a rough surface disappears as a tool becomes too compliant [10]. Thus, tool development is the art of balancing between flexibility and rigidity.

There are three general types of polishing tools, i) rigid tools, ii) semi-flexible tools, and iii) compliant tools. Each type has its own optimal flexibility and rigidity for its major purpose as a polishing tool. (A general comparison between different tool types is given in Section 2.3.) However, it is very difficult to achieve both flexibility and rigidity at the same time due to their conflicting characteristics.

The present work introduces a rigid conformal (RC) tool, that uses a non-Newtonian fluid (*a.k.a.* solid-liquid) that has both flexibility and rigidity at the same time, but for different time scales. (*Note*: A US provisional patent was filed for the RC lap.) Section 2 provides a theoretical background including a brief introduction about the properties of the non-Newtonian fluid. An actual RC lap along with its schematic structural design is presented in Section 3. Some experimental performance demonstrations of the RC lap are given in Section 4.

2. Theoretical background

2.1 Non-Newtonian fluid

Since the days of Sir Isaac Newton, opticians have relied on the visco-elastic properties of pitch to create effective polishing tools. Pitch acts as a highly viscous Newtonian fluid for long time scales – it undergoes shear motion that is proportional to the shear stress, so it flows to conform to the shape of the workpiece. At constant temperature, this flow is characterized by the viscosity and is described by the Navier-Stokes equations [11]. Pitch has two principal limitations for polishing: the TIF tends to be unstable, and it does not flow fast enough to accommodate the use of large tools on steep aspheric surfaces [12].

In order to insure that the tool conforms to the surface, we desire a lap made from a material that will flow much more quickly than pitch. Yet we wish to maintain the tool's rigid behavior to preserve the natural smoothing abilities. Such a tool can be made by replacing the pitch with a visco-elastic non-Newtonian fluid. The visco-elastic fluid will act like a solid for a short time period under stress. If stress is applied over a long time period, it flows like a liquid.

A bar made of non-Newtonian silastic polymer (SP) (~2×2×15cm pink bar) was hand-molded as shown in Fig. 1.

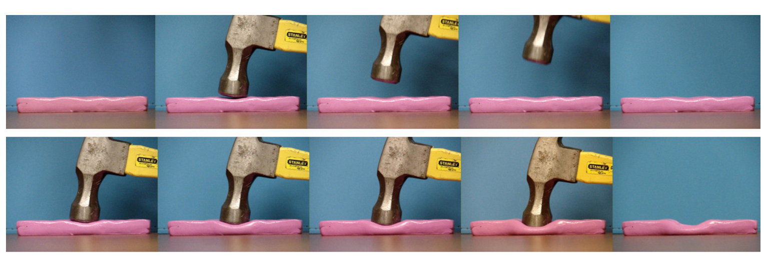

Fig. 1. Two phases of a visco-elastic non-Newtonian silastic polymer: solid-like phase for <~0.1 seconds hammering impulse (top), and liquid-like phase for ~17 seconds long stress by hammer's weight (bottom), (Note: These pictures are edited to contrast the two phases. A more comprehensive view is provided in the accompanying movie clip, Media 1.)

In the upper figure, the bar was hammered for less than ~0.1 seconds time (*i.e.* impact duration). The bar was deformed by a small amount after the harsh impact. This is the solid-like behavior of the non-Newtonian fluid. The lower figure shows a large deformation of the bar. When the hammer was gently placed on the bar loaded by only its weight, the bar started to flow just like a liquid. The duration of the load was ~17 seconds, much longer than the hammer strike case. The accompanying movie clip (Media 1) clearly contrasts these two opposite phases. (The time duration threshold that distinguishes the two phases varies for different non-Newtonian fluids.)

2.2 Dynamic modulus and smoothing effect of non-Newtonian fluid

Non-Newtonian fluids can resist deformation in a solid-like or fluid-like (i.e. viscous) manner depending on the applied frequencies of stress. In order to quantitatively understand these characteristics, the dynamic modulus is used. The dynamic modulus is defined as the ratio of the stress to strain under an oscillating stress condition. These oscillating strain and stress relationships can be expressed as

$$\varepsilon = \varepsilon_0 \sin(t\omega) \tag{1}$$

$$\sigma = \sigma_0 \sin(t\omega + \delta) \tag{2}$$

where ε is time dependent strain, ε_0 is magnitude of the strain, t is time, ω is angular frequency of oscillation, σ is time dependent stress, σ_0 is magnitude of the stress, and δ is phase lag between the stress and strain.

For an ideal solid, the strain and stress are oscillating in phase (*i.e.* δ=0°). For instance, strain has its largest value when the stress also becomes the largest. If the material is an ideal viscous fluid, the stress is 90° out of phase (*i.e.* δ=90°) with the strain.

For these oscillating stress and strain, the tensile storage modulus and loss modulus are defined to quantify the solid-like and fluid-like properties as below [13].

$$Storage\ modulus: E' = \frac{\sigma_0}{\varepsilon_0}\cos\delta \tag{3}$$

$$Loss\ modulus: E'' = \frac{\sigma_0}{\varepsilon_0}\sin\delta \tag{4}$$

The storage modulus is related to the elastic deformation, and the loss modulus is related to the time-dependent viscous behavior of a non-Newtonian fluid. For instance, the storage modulus of an ideal solid (*i.e.* δ=0°) is the same as the classical Young's modulus.

A loss tangent, the ratio between the storage and loss modulus, is a convenient measure of the relative contribution of the solid-like to fluid-like mechanical responses [13]. The loss tangent is defined as

$$\tan\delta = \frac{E''}{E'} \tag{5}$$

where $\tan\delta$ is the loss factor. For instance, $\tan\delta$ >1 indicates a fluid-like behavior of the material. If $\tan\delta$ <1, it means that the solid-like response is predominant over the fluid-like response.

Some measured storage modulus and loss tangent values for fused silica and Silly-Putty™ (Silly-Putty is a trademark of Crayola LLC.) were obtained from the literature, and are shown in Fig. 2 [14]. Fused silica can be regarded as an elastic solid, so that the loss tangent is almost zero. Also, the storage modulus is almost a constant ~70GPa over the 0-10Hz frequency range of the oscillating stress. In contrast, the Silly-Putty™ is a non-Newtonian fluid, which has an inorganic polymer with visco-elastic agent (polydimethylsiloxane) in it. The frequency-dependent behavior is clearly shown in Fig. 2

(right). Based on the loss tangent values, Silly-Putty™ begins to act like a solid when the applied stress is oscillating at more than ~1Hz [14]. Also, the storage modulus E' in the high frequency range (*i.e.* >5Hz) is ~30 times larger than the low frequency range (*i.e.* <0.2Hz) values.

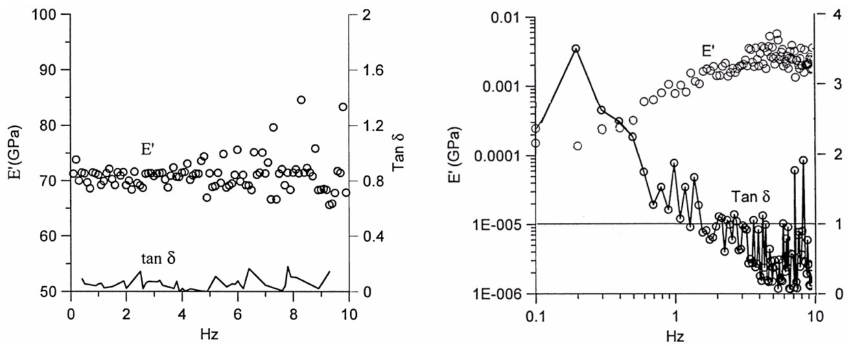

Fig. 2. Storage modulus E' and loss factor $tan\delta$ for fused silica (left) and Silly-Putty™ (right) as a function of applied stress frequency from the literature [14]

The storage modulus plays an important role in estimating the smoothing effect of a tool. The storage modulus defines how much local pressure is required for a tool to be deformed by a local bump on the workpiece as shown in Fig. 3. If an elastic material has a thickness L and storage modulus E', the additional local pressure (on top of the nominal polishing pressure) due to ΔL bump deformation can be calculated from Eq. (3) as

$$P_{add} = \sigma_0 = \varepsilon_0 \cdot \frac{E'}{\cos\delta} = \frac{\Delta L}{L} \cdot \frac{E'}{\cos\delta} \tag{6}$$

where P_{add} is the additional local pressure.

If the deformed local area is small enough compared to the whole tool area, the change in the nominal pressure due to the induced local pressure may be ignored. Then, this additional local pressure can be added to the nominal polishing pressure. The higher local polishing pressure on the bump is

$$P_{bump} = P_{nominal} + P_{add} \tag{7}$$

where $P_{nominal}$ is the nominal polishing pressure without the bump.

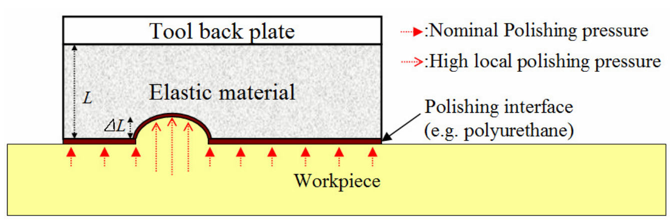

Fig. 3. Locally deformed elastic material due to a bump

For instance, if a tool using L=1cm thick elastic material with 0.003GPa storage modulus material (*e.g.* Silly-Putty™ with ~10Hz tool motion relative to the surface features) meets a ΔL=1μm bump, and is locally deformed by it, then the additional local pressure on the bump is 0.043psi using Eq. (6). (The phase lag δ is assumed as 0, because the loss tangent was ~0 at around 10Hz.) Thus, if the nominal pressure under the tool is 0.4psi, the bump feels an additional ~0.04psi, which results in increased removal, which wears down the bump.

As mentioned above, the storage modulus of a non-Newtonian fluid is a very important clue to understanding the smoothing characteristics of the RC lap. However, the actual smoothing process by a tool is entangled with many other factors, such as the actual tool structure, polishing pad property, and so forth. Also, the fluid dynamics of polishing compounds may play a role in the smoothing process. An in-depth smoothing model with more detailed discussion about the smoothing process will be reported in another paper with some experimental results [15].

2.3 Comparison between RC lap and other tools

As briefly mentioned in Section 1 there are three general types of polishing tools: i) rigid tools, ii) semi-flexible tools, iii) compliant tools. The schematic structures for different tool types are depicted in Fig. 4. Some general advantages and disadvantages of each type are summarized in Table 1. However, we duly acknowledge that the actual characteristics for a specific tool may not agree with this generalized comparison.

The most conventional and common polishing tools are rigid tools (*e.g.* a pitch tool on a thick aluminum back plate). These tools are usually built with a hard (stiff) material like a thick aluminum plate as a tool base structure. A polishing material, such as pitch or a polyurethane pad is placed under the base plate as a polishing interface. Because the polishing surface shape of the tool is fixed (or changes very slowly) during the polishing run, it needs to be conditioned to fit a workpiece before using it. Otherwise, a misfit may cause radial zones in the workpiece surface figure. It is clear that this type of tool is very good for spherical surface polishing, which has same curvature everywhere on the workpiece. It is relatively easy to make a large tool (*e.g.* 2m diameter tool), and the tool manufacturing cost is usually low. Availability of a large tool is especially important for large optics production (*e.g.* >4m diameter), because the tool size is directly related to the speed of material removal. For instance, the 8.4m Giant Magellan Telescope primary segment [16] cannot be fabricated using a 10cm tool. A 10cm tool would take ~350 hours to polish a 1um thickness of material from the ~55m^2 workpiece area assuming nominal polishing condition values such as 1psi tool pressure, 1m/sec relative speed between the tool and workpiece, and 20um/psi(m/sec)hr Preston constant. Because rigid tools have very small local compliance, they show a good smoothing effect [10, 12]. However, these rigid tools need to be customized for each workpiece. Also, the polishing surface of the tool needs to be carefully maintained once it fits to the workpiece. It has, however, an intrinsic limitation in fabricating aspheric (or freeform) workpieces. The rigid tool cannot follow the local curvature changes as the tool moves on the workpiece.

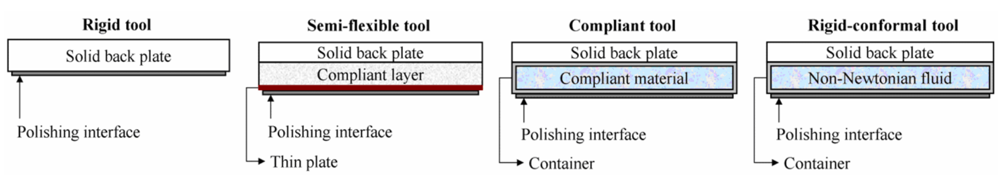

Fig. 4. Schematic tool structures of four different tool types

The semi-flexible tool is carefully designed to fit the varying low order curvature changes while the tool moves on the workpiece. It usually uses a relatively thin metal plate as a tool base, so that the plate's low order bending modes fit the workpiece local curvatures. A foam layer may be placed between the thin plate and another base structure (*e.g.* thick plate). A polishing pad or pitch is used under the semi-flexible thin plate as a polishing interface. The bending modes can be utilized actively (*e.g.* stress-lap [17] using actuators) or passively (*e.g.* membrane tool [10] using tool's self weight under the gravity). Because these tools try to balance flexibility and rigidity, they can be used for various workpieces including aspheric surfaces. These tools can fit to a workpiece surface, while still providing excellent smoothing effects. Also, a large tool can be manufactured without great difficulty. However, for a passive semi-flexible tool, it must be designed for a specific workpiece by means of a careful and usually time consuming finite element analysis. The actual performance of a new tool needs to be verified and calibrated before use, which is not a trivial task. For an active semi-flexible tool, complex structures to control the bending modes are required. For instance, the stress-lap has many actuators to control the tension on metal wires that are connected to the posts around the perimeter of the circular metal plate [17]. (Because this metal plate is relatively thicker than the thin metal plate in the membrane tool, the stress-lap is often regarded as an actively controlled rigid tool.) By actively pulling or releasing the wires, the metal plate's shape can be controlled. However, the actual bending or pressure distribution under the tool is not easily predicted, so the removal prediction becomes complicated.

The compliant tool can be regarded as the extreme opposite to the rigid tool. This type of tool utilizes compliant materials, such as a liquid or air. Those materials are often sealed in a container (*e.g.* Zeeko's Precessions™ using an inflated membrane polisher [4]) or they make direct contact with the workpiece (*e.g.* QED's MRF™ using a magneto-rheological fluid on a spinning wheel [5]). These polishing tools can conform to virtually any type of workpiece including aspheric and freeform surfaces. Because the tool always maintains a perfect fit, the material removal (*i.e.* TIF) is very deterministic and stable. However, these tools are usually equipped with complex structures to control liquid or air with high accuracy. Making a large tool (*e.g.* >30cm wide contact spot size) can be a very difficult and expensive task. An expensive high performance NC machine is usually required to control the position and motion of the relatively small tool accurately. Small mis-positioning of the small tool may cause tool marks on the finished workpiece surface, and decrease the process convergence rate. Because the tool will conform to the edge of the workpiece, it cannot go over the edge (*i.e.* overhang) for the edge figuring process. As a result, the edge figuring requires a more delicate technique, such as lifting up the tool for smaller and smaller contact spot sizes as it approaches the edge of the workpiece. It has almost no smoothing effect since it fits to all spatial frequency components of the workpiece surface.

Table 1. General comparison between different tool types [a, b]

	Rigid tool	Semi-flexible tool	Compliant tool	Rigid conformal tool
Making large tool (*e.g.* >30cm)	Easy	Easy	Difficult	Easy
Cost (including a NC machine)	Inexpensive	Medium	Expensive	Inexpensive
A tool for different workpieces	No	Limited	Yes	Yes
Smoothing	Good	Good	Poor	Medium
Predictability	Low	Fair	Excellent	Good
Fitting to workpiece surface	Poor	Fair	Good	Good
Working on aspheric workpiece	Difficult	Good	Easy	Easy
Working on freeform workpiece	Difficult	Hard	Easy	Easy
Working over the edge	Yes	Yes	No	Yes
Tool maintenance	Difficult	Easy	Medium	Easy

[a] Blue items are usually regarded as advantages.

[b] This is just a general comparison. These characteristics may vary for a specific tool.

The new RC lap takes the advantages from both the rigid and compliant tool in two different time scales. Because the tool motion (*e.g.* orbital motion [18]) is usually fast (*e.g.* >10Hz) relative to the local features under the motion (*e.g.* bumps), the RC lap acts like a high storage modulus rigid tool with respect to that time scale as mentioned in Section 2.2. For instance, if the tool is orbiting at 100rpm on a bumpy area on the workpiece, the tool rubs on the bumps with high local pressure. Thus, it can smooth the bumpy surface. Also, the RC lap can go over the edge of the workpiece because the tool does not conform to the edge as long as the tool spins or orbits at high speed. The edge removal characteristic of RC lap was reported in another paper [18-19]. However, the tool still fits to the local curvature changes of the workpiece since the RC lap moves on the workpiece relatively slowly (*e.g.* ~1 rpm workpiece rotation) along the tool path. (This local curvature characteristic is well described in a literature by Parks [20].) For instance, for an off-axis parabolic workpiece, the tool may travel around the workpiece once a minute. The tool will fit to the slowly varying local curvature of the off-axis part. The non-Newtonian fluid flows like a liquid for this long time scale motion as mentioned in Section 2.2. Thus, a RC lap can be used for many different workpieces (including aspheric and freeform surfaces) like a compliant tool. Also, it is not difficult to make a large tool (*e.g.* >30cm diameter tool) because the non-Newtonian fluid is more easily handled (or contained) than a liquid or air. A manufactured 330mm diameter RC lap working on the 8.4m diameter Giant Magellan Telescope (GMT) off axis segment is presented in Section 3.3. The tool manufacturing cost is also low.

3. Rigid conformal lap using non-Newtonian fluid

3.1 Schematic RC lap structure

A schematic 3D model for a RC lap is depicted in Fig. 5. It is a polishing tool filled with a non-Newtonian silastic polymer. The SP is contained between a back plate and a diaphragm. The diaphragm provides a tough and flexible seal to contain the non-Newtonian fluid during polishing runs. It is made out of a layer of woven fabric impregnated with a thin layer of elastomer [21], and the total thickness is between 0.38-1.14mm. The polishing pad is placed on the diaphragm. This is the actual contact interface with the workpiece. The polishing pad can be polyurethane, polishing cloth, and so forth. The polishing pad may be tiled as shown in Fig. 8 (left and middle) in order to create channels for uniform polishing compound distribution under the tool.

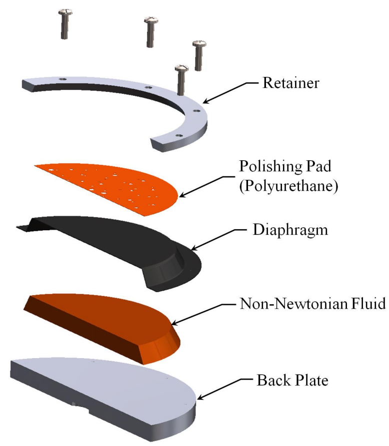

Fig. 5. 3D schematic RC lap structure (exploded and cut in half)

3.2 Forcer design for RC lap

A forcer is usually a drive pin used to provide tool motion as shown in Fig. 6. The interface between the forcer and tool needs to be designed carefully. An over-constrained forcer may apply un-wanted force or moment to a workpiece, which may result in unstable removal due to the disturbed pressure distribution. The workpiece may even be broken. Ideally, the forcer only gives tangential tool motions without any vertical force with respect to the workpiece surface. Polishing pressure comes from the tool's self weight as shown in Fig. 6 (left).

The most common forcer is a drive pin with a ball at the end. The ball goes into the spherical hole on the back plate of a tool as shown in Fig. 6 (middle). By preventing the ball from hitting the bottom of the hole, the forcer does not apply any vertical force to the tool. However, as the drive pin moves, the induced moment from the shear force on the workpiece surface causes a moment and a gradient (*i.e.* linearly varying) polishing pressure distribution. This gradient pressure distribution is shown in Fig. 6 (right).

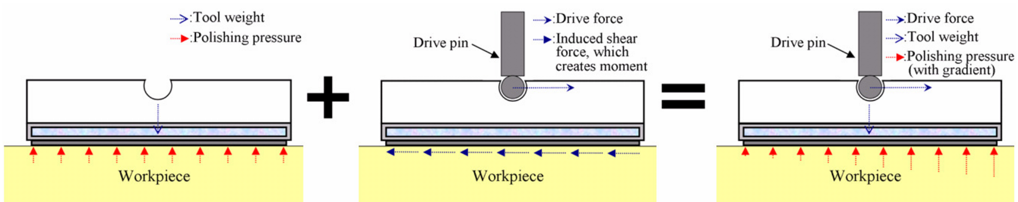

Fig. 6. The gradient net polishing pressure distribution due to the tool weight and the induced moment from the drive force

The forcer for the RC lap was carefully designed to mitigate this unwanted gradient pressure effect. Two different approaches were developed. The first approach was bringing the ball down as closely as possible to the polishing surface, so that the moment from the shear force is minimized. The schematic design is shown in Fig. 7 (left). An actual RC lap with a lowered drive pin hole is shown in Fig. 8 (right). Another approach was a forcer providing a virtual pivot using a number of linkages [22]. The linkages provide a virtual pivot on a workpiece, so that the induced moment becomes zero in theory. This can be very useful for small size tools, which usually have relatively low aspect ratios (*i.e.* thick tools), because they have a steeper pressure gradient. Each end of a linkage is connected to the forcer plate and tool with a ball interface, which allows free rotation in all directions. The schematic configuration for the linkage forcer is presented in Fig. 7 (right).

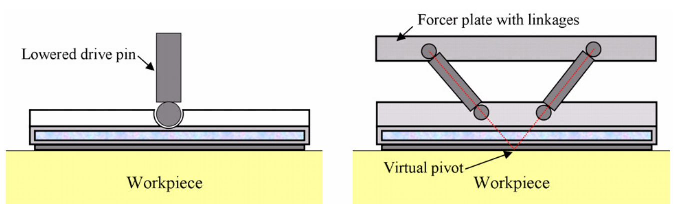

Fig. 7. Schematic forcer designs, which solve the gradient polishing pressure problem in Fig. 6: Lowered drive pin approach (left) and linkage forcer plate approach to provide a virtual pivot (right)

3.3 Manufactured RC lap

Three RC laps (110, 220, and 330mm in diameter) were manufactured. Among many non-Newtonian visco-elastic fluids, Silly Putty™ was used in these RC laps. The 220mm RC lap and 330mm RC lap are presented as an example in Fig. 8 and 9, respectively. The 330mm RC lap was used on the 8.4m diameter GMT off axis segment at the Steward Observatory Mirror Lab [16].

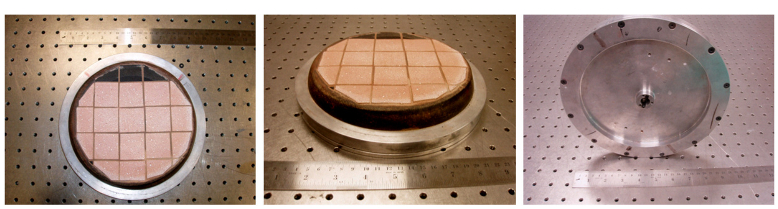

Fig. 8. Manufactured 220mm diameter RC lap (bottom, side, top view from left to right) Three of the polishing pad tiles were intentionally removed to show the structure below. The black seen is the diaphragm shown in Fig.5.

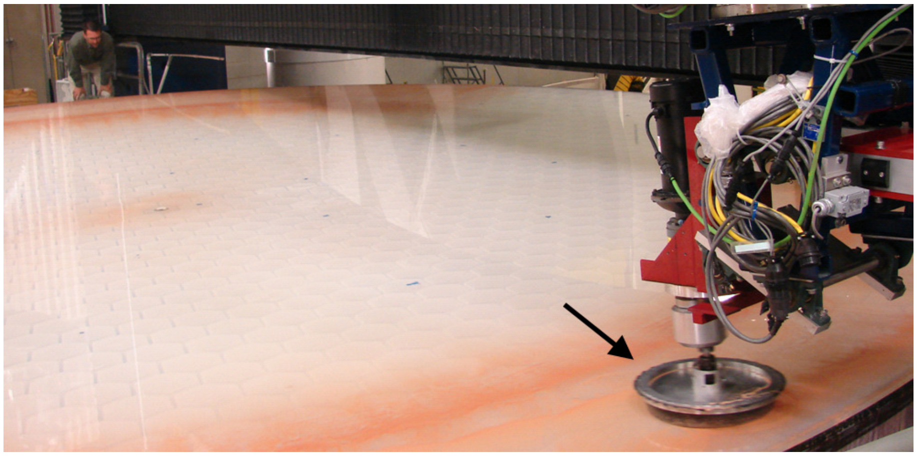

Fig. 9. 330mm diameter RC lap (black arrow) on the 8.4m diameter GMT off axis segment at the Steward Observatory Mirror Lab [16]. (Note: The orbital tool motion is shown in the accompanying movie clip, Media 2.)

A machined aluminum back plate and a Bellofram^{TM} diaphragm [21] were used with a polyurethane polishing pad. A Cerium doped polyurethane polishing pad LP-66 was tiled for channels. (LP-66 is a polyurethane polishing pad sold by Universal Photonics INC.) Detailed specification of the RC laps is listed in Table. 2.

Table 2. Specification of three RC laps

Tool diameter	110, 220, 330mm
Aluminum back plate thickness	10mm
Non-Newtonian fluid	Silly-Putty^{TM}
Non-Newtonian fluid thickness	10-20mm
Diaphragm	Bellofram^{TM} diaphragm
Polyurethane polishing pad	LP-66 (Cerium doped pad)
Polyurethane polishing pad thickness	0.5mm

4. Performance of rigid conformal lap

4.1 Measured TIF vs. theoretical TIF

One of the most powerful characteristics of the RC lap is highly stable theory-like TIF. The theoretical TIF can be calculated based on the Preston's equation [9]. This stable characteristic mainly comes from the fact that the RC lap always fits to a local workpiece surface and provides a uniform pressure distribution under it. As a result, the TIF does not depend on the shape of the workpiece surface. A measured and theoretical TIF using the 220mm RC lap with an orbital tool motion is shown in Fig. 10.

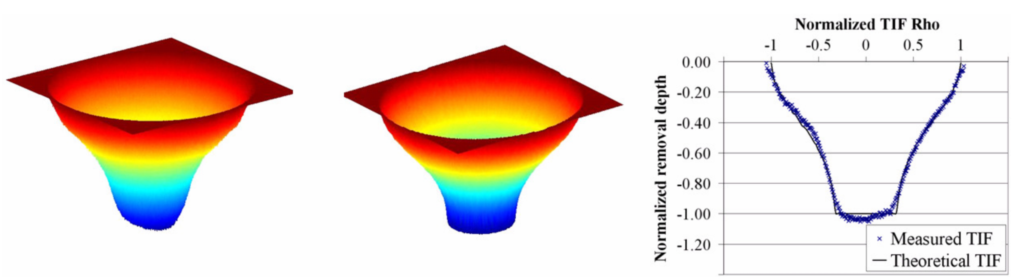

Fig. 10. The TIFs using the RC lap with an orbital tool motion: measured 3D TIF (left), theoretical 3D TIF (middle), and averaged radial profiles of them (right)

The good matching between the measured and theoretical TIFs proves that the removal process can be precisely modeled and predicted using Preston's equation. The deterministic TIFs of the RC lap form good building blocks for the CCOS process. Qualitative results using the measured TIF data (*e.g.* Preston constant variation *vs.* tool age) are given in Section 4.2-4.4.

4.2 Optimal operation range of RC lap

A series of experiments was conducted to determine the optimal operation range of the RC lap. The optimal operation range was defined as: i) Higher Preston constant (*i.e.* removal rate) is better since it means shorter total polishing time. ii) Preston constant needs to be a constant (or a well characterized function such as a linear function) in the optimal range. iii) Surface roughness after the polishing run needs to be ~2nm RMS. As a reference, a typical pitch tool, which is well known for its superb surface finish, usually gives ~1nm RMS surface roughness.

The TIFs were measured as the tool pressure and tool motion speed were varied. A total of 50 experiments were performed, and the removal rates (*i.e.* Preston constant) were calculated from the measured TIFs. Also, the surface roughness values were measured for all experiments. Detailed information about the surface roughness measuring device is presented in Section 4.5. The overall experiment conditions are provided in Table. 3.

Table 3. Overall TIF experiment conditions

Workpiece	10inch Pyrex
RC lap diameter	110mm
Tool motion	Orbital tool motion
Polishing compound	Rhodite 906 (Cerium based)
Polishing compound particle size	~2μm
Tool pressure range	0.20-0.57psi
Tool motion speed range	0.05-0.22m/sec

The experiment results are plotted in Fig. 11. Each marker represents the averaged value, and the standard deviation of the value is given as a vertical error bar.

For tool pressure variation (0.2-0.57psi), the data showed slightly increasing Preston constant values with increasing pressure as shown in Fig. 11 (left). The surface roughness values in this pressure range were almost constant at ~2nm RMS. Because of the higher Preston constant, we defined 0.3-0.6psi as the optimal operation range of the tool pressure.

The orbital tool motion speed was varied 0.05-0.22m/sec as shown in Fig. 11 (right). A non-linear Preston constant change over the tool speeds range was measured. The Preston constant was stable in the 0.15-0.22m/sec range. The surface roughness was ~2nm RMS for all cases. Thus, 0.15-0.22m/sec was chosen as the optimal tool speed range. However, there is still a good chance to get a stable Preston constant value in even higher speed ranges. This will be evaluated in another investigation [23].

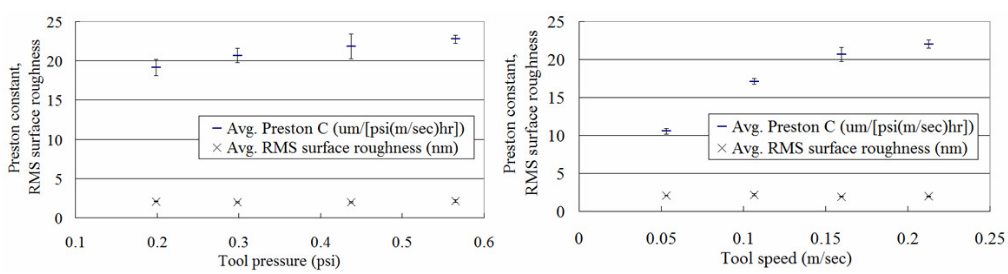

Fig. 11. Preston constant and RMS surface roughness vs. tool pressure (left) or speed (right), (Note: Error-bars represent the standard deviation of the data)

In summary, the optimal RC lap operation range is, i) 0.3-0.6psi for tool pressure, and ii) 0.15-0.22m/sec for tool speed.

4.3 Dwell time linearity

Most CCOS processes assume that the Preston constant is a fixed value over dwell time. In other words, if a polishing tool stays on a workpiece for twice the time, the material removal from the workpiece should be twice also. This is often called the dwell time linearity.

Two different dwell time values (15 and 30 minutes) were tried for 30 experiments, and the results are presented in Fig. 12. The tool was operating within the optimal operation range in Section 4.2. The Preston constant was not changed as we doubled the dwell time. The RC lap shows a good dwell time linearity, which enables a scalable CCOS process (*i.e.* double the dwell time to double the removal).

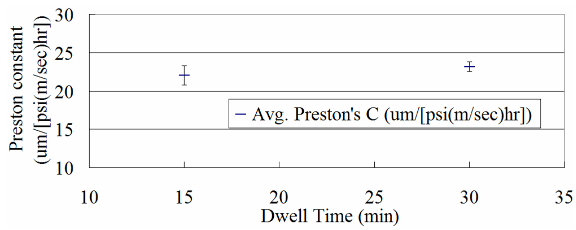

Fig. 12. Preston constant vs. dwell time (Note: Error-bars represent the standard deviation of the data)

4.4 Preston constant vs. tool age

A polyurethane polishing pad (*e.g.* LP-66) needs to be conditioned (*i.e.* breaking down the rough pad surface) on a conditioning workpiece (*i.e.* the dummy workpiece) before its first polishing run. In order to qualitatively analyze the conditioning process and the performance of the RC lap after conditioning, the Preston constant and surface roughness values were measured as a function of tool age. The tool age was set to zero when a new polyurethane pad was attached to the RC lap.

Approximately 100 experiments using the 110mm RC lap were conducted on five Pyrex workpieces. The RC lap was run within the optimal RC lap operation range of Section 4.2. The experimental results are plotted in Fig. 13.

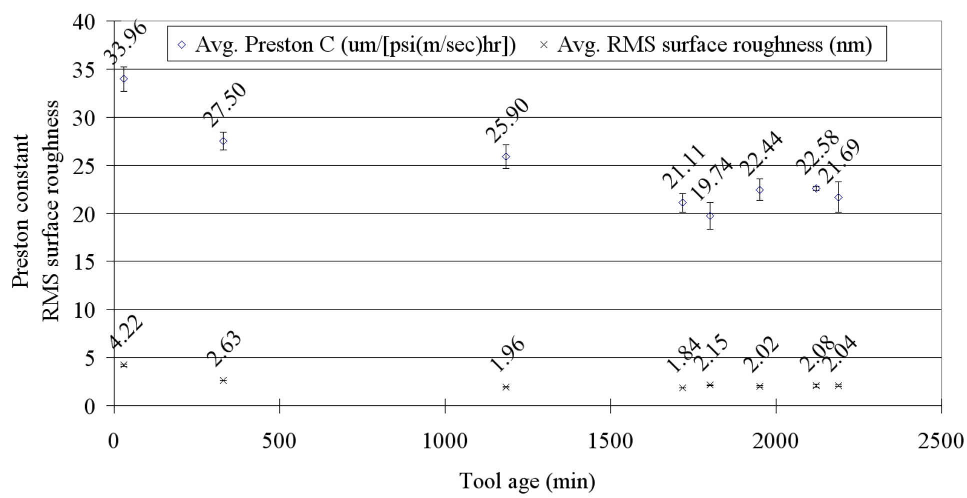

Fig. 13. Preston's constant and RMS surface roughness vs. tool age (Note: Error-bars represent the standard deviation of the value)

The Preston constant values (diamond marker in Fig. 13) were ~34um/[psi(m/sec)hr] when the RC lap was used for the first time. As the tool age approached ~1700minutes, the Preston constant stabilized at ~21um/[psi(m/sec)hr]. The surface roughness values were stable at ~2nm RMS after ~1200minutes tool age. Of course, the tool age axis can be scaled depending on the initial surface roughness of the conditioning workpiece, tool pressure, and tool speed. For instance, higher tool speed and pressure may reduce the conditioning time due to the higher removal per unit time.

Once the RC lap was conditioned (*e.g.* >1700minutes tool age in this case), the Preston constant varied with only ~10% standard deviation. The conditioning process and stable Preston constant after conditioning were successfully demonstrated for the RC lap.

4.5 Surface roughness

The surface roughness after a polishing run is one of the most important criteria used to estimate a tool's performance. If a tool leaves a smooth surface which meets a target specification, the workpiece can be finished using the tool. Otherwise, additional processes using other tools (*e.g.* pitch tools) are required for the final touch-up process to improve the surface roughness [12]. This increases the complexity and time of the CCOS process, so a tool giving a good surface finish is highly desirable.

The surface roughness is a function of many parameters, such as glass material, polishing compound type, and so forth. It is, therefore, invalid to say a tool always gives a certain value for RMS surface roughness. Instead, a tool should be compared to another tool in a similar condition. We set a classical pitch tool as our reference for this study. The pitch tool is well known for its excellent surface finish as mentioned earlier in Section 4.2.

A ULE substrate was used as a common workpiece. The surface roughness after each run was measured using a Wyko NT9800^{TM} interferometer. (Wyko NT9800^{TM} is a trademark of Veeco.) More information about the surface roughness experiment set-up is provided in Table. 4.

Table 4. Two surface roughness experiment set-ups

	110mm RC lap	110mm pitch tool
Polishing Compound	Hastilite ZD	Rhodite 906
Tool Motion	Orbital	Orbital
Workpiece	ULE	ULE
Measurement area	~0.2 by 0.3mm	~0.2 by 0.3mm
Sampling interval	484.11nm	484.11nm

The results from 40 experiments are presented in Fig. 14 and 15. Two example surface roughness profiles measured by the Wyko NT9800^{TM} interferometer are presented in Fig. 14. The reference target surface roughness was set as ~0.9nm RMS, which was an average value from the experiments using a pitch tool with Rhodite 906 polishing compound as shown in Fig. 15.

The surface finish from the RC lap with Hastilite ZD polishing compound was superb. For 10 repeated experiments, the average surface roughness was ~0.75nm RMS with ~0.1nm standard deviation, which is similar or even slightly better than the pitch tool case. (We acknowledge that there may be a better polishing compound for the pitch tool for this specific set-up, which could have given better surface finish. We use this result only as a brief reference for comparison purposes.)

We have demonstrated that the RC lap, with appropriate polishing compound which depends on a given polishing configuration, can provide a <1nm RMS super smooth surface finish. This may eliminate the need for an extra final touch-up step for most CCOS processes, which usually have <2nm RMS surface roughness target specifications.

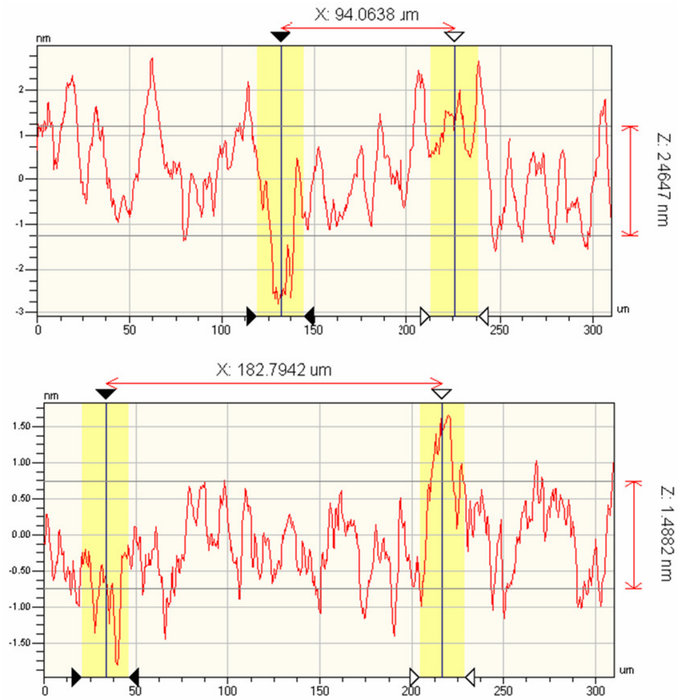

Fig. 14. Two example surface roughness profiles from Wyko NT9800^{TM}: pitch tool with Rhodite 906 (top), and RC lap with Hastilite ZD (bottom) (Note: Averaged (in yellow region) peak-to-valley values are provided as additional information.)

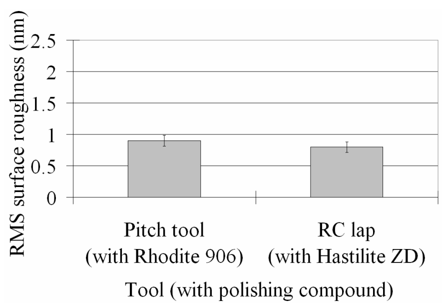

Fig. 15. Surface roughness using a pitch tool and RC lap on a ULE substrate (Note: Error-bars represent the standard deviation of the value)

5. Concluding remarks

The RC lap exhibits the advantages of rigid and compliant tools in two different time scales using a non-Newtonian fluid. It can be used just like a rigid tool, which has a smoothing effect, with respect to the tool motion (*e.g.* orbital) time scale. As it moves along the tool path on the workpiece, the non-Newtonian fluid flows to fit the slowly varying local curvatures under the tool. The highly deterministic TIF and removal rate was experimentally demonstrated and verified. Also superb surface finish with <1nm RMS surface roughness was achieved on a ULE substrate. In addition to its good performance, the ease with which a large tool can be made in a cost-effective manner makes the RC lap an attractive solution for large precision optics manufacturing CCOS processes. It can also contribute to the realization of some next generation optical systems, which usually have hundreds of aspheric mirrors (*e.g.* Thirty Meter Telescope [24] and Laser Inertial Fusion Engine [25]) or large off axis mirrors (*e.g.* Giant Magellan Telescope [16]).

Acknowledgments

We acknowledge that this work was supported by the Optical Engineering and Fabrication Facility of the College of Optical Sciences at the University of Arizona.

We thank Marty Valente (Optical Engineering and Fabrication Facility), Robert Parks (College of Optical Sciences) and Brian Cuerden (Steward Observatory) at the Univ. of Arizona for assistance in the final manuscript preparation. Also, we thank Bill Anderson (Optical Engineering and Fabrication Facility) for performing the experiments and Won Hyun Park (College of Optical Sciences) for providing an idea about the non-Newtonian fluids.

The measured data in Fig. 4 was available in this manuscript with the permission of Journal of Materials Research. We thank the journal and A. C. Fischer-Cripps, the author of the original manuscript.

Note: A US provisional patent was filed for the RC lap in this journal article.

APPENDIX B

Parametric Smoothing Model for Rigid Conformal Lap using Visco-elastic Effect

Dae Wook Kim, Won Hyun Park, Hyun Kyoung An

and James H. Burge

Journal article submitted to ***Optics Express***

2009

Copyright Transfer Agreement

The Optical Society of America considers this requested use of its copyrighted materials to be allowed under the OSA Author Agreement submitted by the requester on acceptance for publication of his/her manuscript. It is requested that a complete citation of the original material be included in any publication.

Delois Millner November 25, 2009
Delois Millner Date
Authorized Agent, Optical Society of America

Parametric smoothing model for rigid conformal polishing laps that use visco-elastic materials

Dae Wook Kim*, Won Hyun Park, Hyun Kyoung An, and James H. Burge

College of Optical Sciences, University of Arizona, 1630 E. University Blvd, Tucson, Arizona 85721, USA
*letter2dwk@hotmail.com

Abstract: A parametric smoothing model was developed to quantitatively describe the smoothing action of a rigid conformal (RC) polishing lap that uses special visco-elastic materials. These materials flow to conform to the aspheric shape of the workpieces, yet behave as a rigid solid for short duration caused by tool motion over surface irregularities. The smoothing effect naturally corrects the mid-to-high frequency errors on the workpiece while a large RC lap still removes large scale errors effectively in a short time. Quantifying the smoothing effect allows improvements in efficiency for finishing large precision optics. We define normalized smoothing factor *SF* which can be described with two parameters. A series of experiments using a conventional pitch tool and the RC lap was performed and compared to verify the parametric smoothing model. The linear trend of the *SF* function was clearly verified. Also, the limiting minimum ripple magnitude PV_{min} from the smoothing actions and *SF* function slope change due to the total compressive stiffness of the whole tool were measured. These data were successfully fit using the parametric smoothing model.

OCIS codes: (220.0220) Optics design and fabrication; (220.4610) Optics fabrication; (220.5450) Polishing

References and links

1. R.A. Jones, "Computer control for grinding and polishing," Photonics Spectra, 34-39 (August 1963).
2. R. E. Wagner and R. R. Shannon, "Fabrication of aspherics using a mathematical model for material removal," Applied Optics. **13,** 1683-1689 (1974).
3. D.D. Walker, D. Brooks, A. King, R. Freeman, R. Morton, G. McCavana, and S.W. Kim, "The 'Precessions' tooling for polishing and figuring flat, spherical and aspheric surfaces," Opt. Express, **11**, 958-964 (2003).
4. H. M. Pollicove, E. M. Fess, and J. M. Schoen, "Deterministic manufacturing processes for precision optical surfaces," in *Window and Dome Technologies VIII*, R. W. Tustison, eds., Proc. SPIE **5078**, 90-96 (2003).
5. J. H. Burge, S. Benjamin, D. Caywood, C. Noble, M. Novak, C. Oh, R. Parks, B. Smith, P. Su, M. Valente, and C. Zhao, "Fabrication and testing of 1.4-m convex off-axis aspheric optical surfaces," in *Optical Manufacturing and Testing VIII*, J. H. Burge; O. W. Fähnle and R. Williamson, eds., Proc. SPIE **7426**, 74260L1-12 (2009).
6. D.W. Kim, S.W. Kim and J. H. Burge, "Non-sequential optimization technique for a computer controlled optical surfacing process using multiple tool influence functions," Optics Express. **17,** 21850-21866 (2009).
7. R. E. Parks, "Alignment of off-axis conic mirrors," in *Optical Fabrication and Testing*, OSA Technical Digest Series (Optical Society of America, 1980), paper TuB4.
8. N. J. Brown and R. E. Parks, "The polishing-to-figuring transition in turned optics," SPIE's 25th Annual International Technical Symposium, (SPIE, 1981)
9. P. K. Mehta and P. B. Reid, "A mathematical model for optical smoothing prediction of high-spatial frequency surface errors," in *Optomechanical Engineering and Vibration Control*, E. A. Derby, C. G. Gordon, D. Vukobratovich, P. R. Yoder Jr., and C. H. Zweben, eds., Proc. SPIE **3786**, 447 (1999).
10. M. T. Tuell, J. H. Burge, and B. Anderson, "Aspheric optics: smoothing the ripples with semi-flexible tools," Opt. Eng., **41**, 1473-1474 (2002).
11. M. T. Tuell, "Novel tooling for production of aspheric surfaces," M.S. Thesis (2002).
12. M. Johns, "The Giant Magellan Telescope (GMT)," in *Extremely Large Telescopes: Which Wavelengths?*, T. E. Andersen, eds., Proc. SPIE **6986**, 698603 1-12 (2008).

13. J. Nelson and G. H. Sanders, “The status of the Thirty Meter Telescope project,” in *Ground-based and Airborne Telescopes II*, L. M. Stepp and R. Gilmozzi, eds., Proc. SPIE **7012**, 70121A1-18 (2008).
14. A. Ardeberg, T. Andersen, J. Beckers, M. Browne, A. Enmark, P. Knutsson and M. Owner-Petersen, “From Euro50 towards a European ELT,” in *Ground-based and Airborne Telescopes*, L. M. Stepp, eds., Proc. SPIE **6267**, 626725 1-10 (2006).
15. A. Heller, “Safe and sustainable energy with LIFE” (2009), https://str.llnl.gov/AprMay09/pdfs/05.09.02.pdf.
16. R. E. Parks, “Specifications: Figure and Finish are not enough,” in *An optical Believe It or Not: Key Lessons Learned*, M. A. Kahan, eds., Proc. SPIE **7071**, 70710B1-9 (2008).
17. J. M. Hill, “Optical Design, Error Budget and Specifications for the Columbus Project Telescope,” in *Advanced Technology Optical Telescopes IV*, L. D. Barr, eds., Proc. SPIE **1236**, 86-107 (1990).
18. D.W. Kim, and J. H. Burge, “Rigid conformal polishing tool using non-linear visco-elastic effect,” Optics Express. (to be published).
19. R.P. Chhabra and J.F. Richardson, *Non-Newtonian Flow and Applied Rheology (2nd edition)* (Elsevier Ltd, 2008), Chap. 1.
20. D.W. Kim, W.H. Park, S.W. Kim and J.H. Burge, “Parametric modeling of edge effects for polishing tool influence functions,” Optics Express. **17,** 5656-5665 (2009).
21. M. A. Meyers and K. K. Chawla, *Mechanical Behavior of Materials (2nd edition)* (Cambridge University Press, 2009), 124-125.
22. A. C. Fischer-Cripps, “Multiple-frequency dynamic nanoindentation testing,” J. Mater. Res. **19,** 2981-2988 (2004).
23. Don Loomis, Bob C. Crawford, Norm Schenck, and Bill Anderson, Optical Engineering and Fabrication Facility, University of Arizona, 1630 E. University Blvd, Tucson, Arizona 85721, (personal communication, 2009).
24. N. J. Brown, “Optical polishing pitch,” in *Optical Fabrication and Testing*, Optical Society of America Workshop (Optical Society of America, 1977).
25. D. W. Kim, College of Optical Sciences, University of Arizona, 1630 East University Boulevard, Tucson, AZ 85721, and J. H. Burge are preparing a manuscript to be called "Parametric smoothing model for rigid conformal polishing laps that use visco-elastic materials II."

---

1. Introduction

Various computer controlled optical surfacing (CCOS) processes have been developed since the 1960s [1-5]. These CCOS processes provide attractive solutions for fabrication of precision optics including large aspheric optical surfaces and off-axis segments by exhibiting high convergence rates based on deterministic material removal processes [3-5].

One of the key components for a CCOS process is the polishing tools, which make the physical contact with the workpiece and removes material from it. A tool influence function (TIF) is the shape of the wear function created by the polishing tool motion (*e.g.* spin or orbital motion) on the workpiece. In general, a dwell time map optimization approach is used to achieve a given target removal map [3-6]. Optimization intelligence (*i.e.* software) uses TIFs as building blocks to achieve the target removal map by spatially distributing and accumulating them [6]. Thus, having stable and deterministic TIFs is a critical part to achieving successful CCOS processes.

The TIF is a strong function of tool properties, such as pressure distribution under the tool, polishing material at the contacting interface, contact area shape, tool motion, and so forth. For instance, developing a tool with a deterministic TIF for aspheric (or freeform) optics fabrication becomes a complex problem. Because local surface shape (*e.g.* curvature) of an aspheric surface varies as a function of position on a workpiece [7], a tool with a fixed surface shape cannot be used. Some flexibility in the tool is required to maintain intimate contact with the workpiece surface. However, rigidity of the tool is also desired to get natural smoothing effects, which removes mid-to-high spatial frequency errors on the workpiece [8-11]. Thus, a well-behaved tool development is a balancing problem between flexibility and rigidity.

The smoothing effect becomes more important for large workpiece fabrications, because it is almost the only way to correct mid-to-high spatial frequency errors smaller than the tool size. Based on the deterministic TIFs of CCOS processes, large errors (*i.e.* low spatial frequency surface errors compared to the tool size) can be corrected by increasing the dwell time on the high error areas. However, this method cannot be used for regions smaller than the tool size unless smaller and smaller tools are utilized. Smaller tools require higher tool positioning accuracy to avoid residual tool marks, which is another source of mid-spatial frequency errors. Also, the use of small tools increases the total fabrication time.

Correcting these mid-to-high spatial frequency errors on optical surfaces is very important for the next generation of extremely large telescopes such as the Giant Magellan Telescope [12-14] and for nuclear fusion energy plants using high power lasers (*e.g.* Laser Inertial Fusion Engine [15]). Because the mid-to-high-spatial frequency errors are directly related to the sharpness of the point spread function (*e.g.* Airy disk radius) or the scattering characteristic of high power laser application optics, the overall performance of those systems may be degraded due to those errors. In fact, most recent large optical surfaces have been polished to a target structure function or power spectrum density, which quantify the target form accuracy as a function of spatial frequencies [16-17].

There have been some quantitative investigations for the smoothing effects by semi-flexible tools. Brown and Parks quantitatively explained the smoothing effects by elastic backed flexible lapping belts in 1981 [8]. The smoothing effect using a large flexible polishing lap was introduced and mathematically studied by Mehta and Reid using the Bridging model [9]. The Bridging model was further developed using Fourier series decomposition approach by Tuell [10-11]. These models were successfully demonstrated with experimental data. More detailed explanation about the Bridging model will be given in Section 2.

A rigid conformal (RC) lap using a visco-elastic non-Newtonian fluid was developed and introduced in a previous study [18]. (*Note:* A US provisional patent was filed for the RC lap.) A schematic structure of the RC lap is compared with other tool types in Fig. 1 [18]. The RC lap has both flexibility and rigidity at the same time, but for different time scales. Because the storage modulus of the visco-elastic fluid is a function of the applied stress frequency, the smoothing effect by the RC lap has to be described by a new smoothing model [18]. Also, the new model needs to include other effects such as the fluid dynamics of the polishing compound and the total effective stiffness of the whole tool structure.

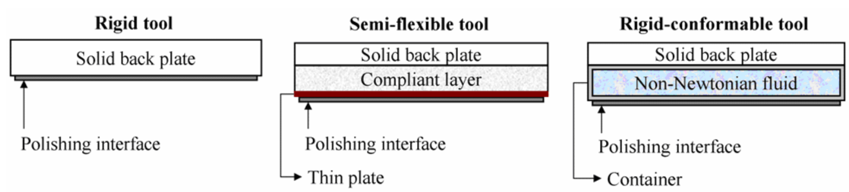

Fig. 1. Schematic tool structures of three different tool types [18]

A parametric smoothing model for the RC lap was developed to quantitatively describe the smoothing effects. Some theoretical backgrounds about the RC lap and Bridging model for semi-flexible tools are provided in Section 2. The parametric smoothing model modified and developed based on the Bridging model is introduced in Section 3. Experimental results for the smoothing effects by a conventional pitch tool and the RC lap are provided and compared in Section 4.

2. Theoretical background

2.1 Rigid conformal lap

The RC lap, which takes advantages from both rigid and compliant tools in two different time scales using a visco-elastic non-Newtonian fluid, has been introduced [18]. The detailed overall structure is shown in Fig 2. Unlike Newtonian fluids (*e.g.* water), the non-Newtonian fluids have varying apparent viscosity values. Their flow characteristics may depend on various conditions like frequency of applied stress [19]. For instance, a visco-elastic non-Newtonian fluid will act like a solid for a short time period under stress. If a long time period stress is applied, it flows like a liquid.

Because the tool motion (*e.g.* orbital motion [20]) is usually fast (*e.g.* 60 RPM) relative to the local features (*e.g.* bumps or ripples) under the motion, the RC lap acts like a rigid tool with respect to that time scale. For instance, if the tool is orbiting at 60 RPM on a bumpy area, the tool quickly smoothes out the bumps with high local pressures on the bump peaks.

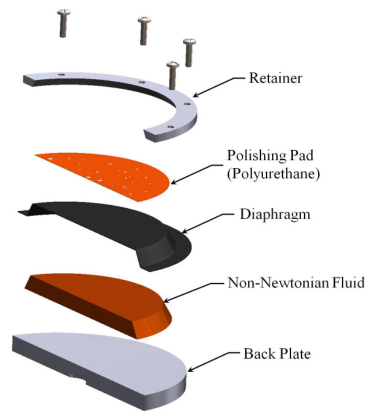

Fig. 2. 3D RC lap structure (exploded and cut in half) [18]

However, the tool will fit the overall local curvature changes on the workpiece since the RC lap moves slowly on the workpiece (*e.g.* ~1 rpm workpiece rotation) along the tool path. For instance, for an off-axis parabolic workpiece, the tool will fit to the slowly varying local curvature of the off-axis part as the tool travels around the workpiece once a minute. The non-Newtonian fluid flows like a liquid for this long time scale motion.

2.2 Smoothing by a rigid tool

The smoothing effects by a rigid tool in Fig. 1 (left) can be understood in a simple way. If we assume the tool does not fit to the surface irregularity under the tool (*i.e.* infinite rigidity), and maintains its shape, the tool only rubs the highs on the surface as shown in Fig. 3 (left). As the tool runs on the workpiece, it will wear down the highs, and eventually the surface will be smoothed out. The spatial frequency of the final surface will be directly related to the tool size of the rigid tool as shown in Fig. 3 (right). This process is clearly shown in the accompanying movie clip (Media 1).

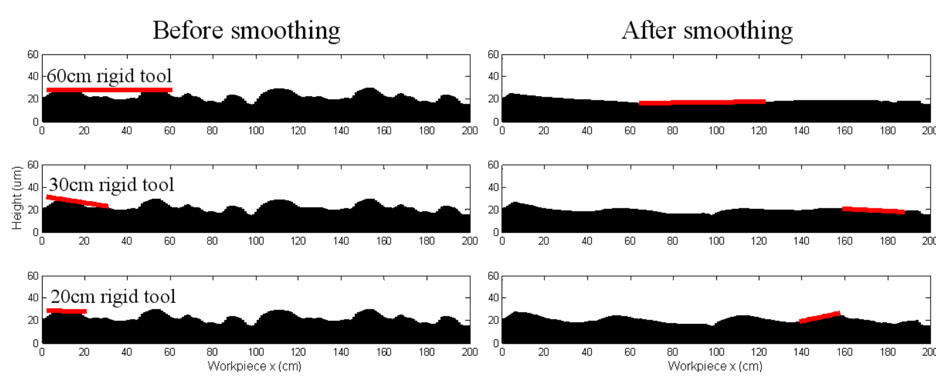

Fig. 3. Smoothing effect simulation using an infinitely rigid tool (Media 1).

Actual polishing tools, however, always require a certain amount of flexibility to fit the overall surface as briefly mention in Section 1. Also, no tool is infinitely rigid, for instance, pitch, which is highly rigid on short time scales, may deform to the small magnitude ripples during a polishing run. These facts lead us to a more comprehensive smoothing model for the flexible tools in Section 2.3.

2.3 Bridging model for smoothing effects by flexible tools

One of the most common approaches to achieving a balance between flexibility and rigidity is using semi-flexible tools as shown in Fig. 1 (middle). It usually uses a relatively thin metal plate as a tool base, so that the plate's low order bending modes are used to fit the workpiece local curvatures. A foam layer is often placed between the thin plate and another base structure (*e.g.* thick plate). A polishing pad (*e.g.* polyurethane pad) or pitch is used under the semi-flexible thin plate as a polishing interface material.

In order to describe the smoothing effects by semi-flexible tools, the Bridging model was introduced [9]. As the tool moves on the workpiece, it continuously bends by different amounts to fit the local curvature, resulting in continuous changes in the pressure distribution under the tool. If a semi-flexible tool meets mid-spatial frequency ripples, the tool contacts the ridges of highs in the surface with higher pressure, and begins to smooth them out. The lap may be imagined to form a bridge across the ridges known as the bridging effect [9].

For a semi-flexible tool, the strains induced from the thin plate bending influence the polishing pressure distribution. Kirchhoff's thin plate equations were modified to include the effect of transverse shear strain. For the one-dimensional case, the polishing pressure distribution *p(x)* due to the sinusoidal error *error(x)* on the surface can be derived based on the theory of elasticity as

$$error(x) = PV(1 - \sin(2\pi \cdot \xi \cdot x)) \tag{1}$$

$$P(x) = P_{nominal} + \frac{error(x)}{\dfrac{1}{D_{plate} \cdot (2\pi\xi)^4} + \dfrac{1}{D_{s\_plate} \cdot (2\pi\xi)^2} + \dfrac{1}{\kappa_{total}}} \tag{2}$$

where PV is the peak-to-valley magnitude of the sinusoidal error, ξ is the spatial frequency of the surface error, $P_{nominal}$ is the nominal pressure under the tool, D_{plate} is the flexural rigidity of the plate, D_{s_plate} is the transverse shear stiffness of the plate, and κ_{total} is the compressive stiffness of the whole tool including elastic material (*e.g.* pitch) and polishing interface material (*e.g.* polyurethane pad) [9]. The flexural rigidity and transverse shear stiffness of the flexible thin plate are defined as

$$D_{plate} = E_{plate} \cdot t_{plate}^{\ 3} / 12(1 - \nu_{plate}^{\ 2}) \tag{3}$$

$$D_{s\_plate} = E_{plate} \cdot t_{plate} / 2(1 - \nu_{plate}) \tag{4}$$

where E_{plate} is the Young's modulus of the plate material, t_{plate} is the plate thickness, and ν_{plate} is the Poisson's ratio of the plate.

The Bridging model in Eq. (2) describing the smoothing effects by a semi-flexible tool was successfully demonstrated by comparison with experimental results [9].

3. Parametric smoothing model

3.1 Dynamic modulus of non-Newtonian fluid

Non-Newtonian fluids can resist deformation in a solid-like or fluid-like (*i.e.* viscous) manner depending on the frequency of the applied stress. In order to quantitatively describe these time-dependent characteristics, the dynamic modulus is used. The dynamic modulus is defined as the ratio of the stress to strain under an oscillating stress condition

Two dynamic modulus values, tensile storage modulus and loss modulus, are defined as Eq. (5) and (6). The storage modulus is related to the elastic deformation, and the loss modulus is related to the time-dependent viscous behavior of a non-Newtonian fluid.

$$Storage\ modulus: E' = \frac{\sigma_0}{\varepsilon_0}\cos\delta \tag{5}$$

$$Loss\,modulus: E'' = \frac{\sigma_0}{\varepsilon_0}\sin\delta \tag{6}$$

where the oscillating stress and strain are expressed as

$$\varepsilon = \varepsilon_0 \sin(t\omega) \tag{7}$$

$$\sigma = \sigma_0 \sin(t\omega + \delta) \tag{8}$$

The ε is the time dependent strain, ε_0 is magnitude of the strain, t is time, ω is angular frequency of the oscillation, σ is the time dependent stress, σ_0 is magnitude of the stress, and δ is phase lag between the stress and strain [21].

The phase lag δ is a function of the angular frequency ω for the non-Newtonian fluid. For an ideal solid, the strain and stress are oscillating in phase (*i.e.* δ=0°). If the material is an ideal viscous fluid, the stress is 90° out of phase (*i.e.* δ=90°) with the strain. A loss tangent, which is the ratio between the storage and loss modulus, is a convenient measure of the relative contribution of the solid-like and fluid-like mechanical responses [22]. The loss factor $\tan\delta$ is defined as

$$\tan\delta = \frac{E''}{E'}\ . \tag{9}$$

For instance, $\tan\delta>1$ indicates a fluid-like behavior of the non-Newtonian material. If $\tan\delta<1$, it means that the solid-like response is dominant over the fluid-like response. Thus, for efficient smoothing actions, the RC lap needs to be run under conditions where $\tan\delta<1$.

Some measured storage modulus and loss tangent values for fused silica and Silly-Putty™ (SP) by Crayola LLC were obtained from the literature, and are presented in Fig. 4 [22]. Because Fused silica can be regarded as an elastic solid, the loss tangent is almost zero. Also, the storage modulus is almost a constant ~70GPa over the 0-10Hz oscillating stress frequencies. In contrast, the SP is a non-Newtonian fluid, which contains a visco-elastic agent (polydimethylsiloxane). The frequency dependence of the storage modulus is clearly shown in Fig. 4 (right). The SP begins to act like a solid (*i.e.* $\tan\delta<1$) when the applied stress frequency is larger than ~1Hz [22].

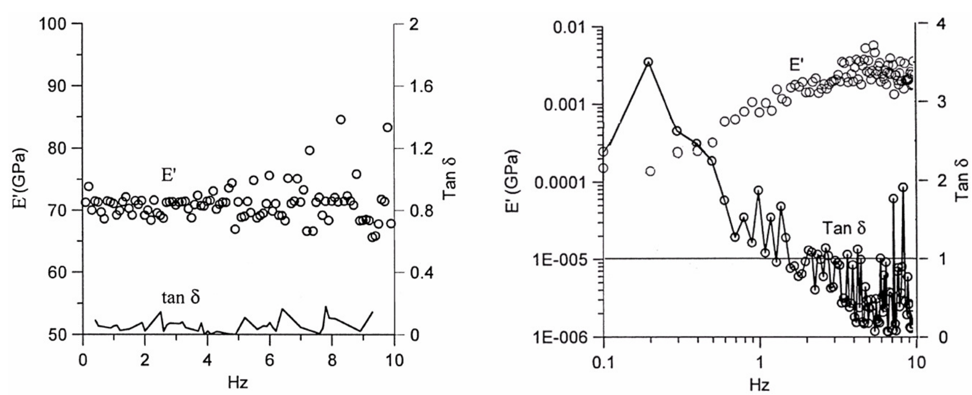

Fig. 4. Storage modulus E' and loss factor $\tan\delta$ for fused silica (left) and Silly-Putty™ (right) as a function of applied stress frequency from the literature [22]

3.2 Polishing pressure distribution under RC lap

The smoothing action by the RC lap can be described using the storage modulus of the non-Newtonian fluid. Because there is no flexible thin plate in the RC lap, the Bridging model in Eq. (2) can be simplified as

$$P(x) = P_{nominal} + \kappa_{total} \cdot error(x) \ . \tag{10}$$

Because the elastic material behavior (*i.e.* visco-elastic material under the tanδ<1 condition) in the RC lap is a main source of the total compressive stiffness of the tool, the κ_{total} can be approximated by two springs connected in series as

$$\frac{1}{\kappa_{total}} = \frac{1}{\kappa_{elastic}} + \frac{1}{\kappa_{others}} \tag{11}$$

where $\kappa_{elastic}$ is the stiffness of the elastic material and κ_{others} is the combined stiffness of all other structures including polishing pad, polishing compound fluid, wrapping material, and so forth. Because the elastic material is a non-Newtonian fluid in the RC lap, the compressive stiffness $\kappa_{elastic}$ is a function of applied stress frequency ω.

By combining Eq. (10) and (11) the pressure distribution under the RC lap is expressed as

$$P(x) = P_{nominal} + \kappa_{total} \cdot error(x) = P_{nominal} + \frac{1}{\frac{1}{\kappa_{elastic}} + \frac{1}{\kappa_{others}}} \cdot error(x) \ . \tag{12}$$

The stiffness of the elastic material $\kappa_{elastic}$ can be expressed in terms of the storage modulus from Section 3.1, which defines the local pressure caused by the deformation from a bump on the workpiece. If an elastic material with storage modulus E' has a thickness L and is compressed by a ΔL tall bump, the compressive stiffness $\kappa_{elastic}$ is

$$\kappa_{elastic} = \frac{\sigma_0}{\Delta L} = \frac{\varepsilon_0 \cdot E'/\cos\delta}{\Delta L} = \frac{\{\Delta L/L\} \cdot E'/\cos\delta}{\Delta L} = \frac{E'}{L \cdot \cos\delta} \tag{13}$$

based on Eq. (5).

The applied angular frequency ω is determined by the spatial frequency of the surface error ξ and the speed of the tool motion V_{tool_motion} as

$$\omega = \frac{2\pi}{T} = \frac{2\pi}{(1/\xi \cdot V_{tool\_motion})} = 2\pi \cdot \xi \cdot V_{tool\_motion} \tag{14}$$

where T is the time interval between a position under the tool sees two adjacent peaks in the sinusoidal ripple and V_{tool_motion} is the speed of the tool motion.

For example, a RC lap with L=8mm thick SP may rub on a sinusoidal ripple with spatial frequency ξ=0.085mm^{-1} and ripple magnitude PV=1μm. A typical 2500Pascal (*i.e.* ~0.36PSI) nominal pressure is assumed. If a very thin polyurethane polishing pad and wrapping material are assumed, the compressive stiffness κ_{others} will be much larger than $\kappa_{elastic}$. Thus, κ_{total} in Eq. (11) is almost equal to $\kappa_{elastic}$. If the tool motion was a 30RPM orbital motion with 30mm orbital radius, the speed V_{tool_motion} is

$$V_{tool\_motion} = \frac{2\pi \cdot 30 \cdot 30}{60} = 94.2 \ [mm/\sec] \ . \tag{15}$$

Then, the applied stress frequency ω in Eq. (14) becomes

$$\omega = 2\pi \cdot \xi \cdot V_{tool\_motion} = 2\pi \cdot 0.083 \cdot 94.2 = 49.13 \ [radians / sec] \quad . \tag{16}$$

From the measured storage modulus values in Fig. 4 (right), SP has E'=~0.003GPa storage modulus at $f=\omega/2\pi$=49.13/2π=~8Hz. The phase lag δ is almost zero, because the loss tangent $\tan\delta$ is ~0 at 8Hz. Thus, using Eq. (12) and (13), the polishing pressure under the RC lap is

$$\begin{aligned} P(x) = P_{nominal} + \frac{E'}{L \cdot \cos\delta} \cdot error(x) &\approx 2500 + \frac{0.003\times10^{9}}{8\times10^{-3}\cdot 1} \cdot 1\times10^{-6} \cdot (1-\sin(2\pi \cdot 0.085 \cdot x)) \\ &= 2500 + 375 \cdot (1-\sin(2\pi \cdot 0.085 \cdot x)) \ [Pascal] \end{aligned} \tag{17}$$

where $\cos\delta$ was approximated as 1 for δ=~0.

Thus, the high peaks on the sinusoidal surface feel an additional 375Pascal polishing pressure, which results in smoothing on the peaks.

3.3 Parametric smoothing model for RC lap

In most smoothing cases, the practical interest is not in the polishing pressure distribution itself, but in the speed of the smoothing action using the pressure distribution on a given ripple as shown in Fig. 5. This can be modeled by using the pressure distribution in the well-known Preston's equation

$$\Delta z(x) = R_{Preston} \cdot P(x) \cdot V_{tool\_workpiece}(x) \cdot \Delta t(x) \tag{18}$$

where Δz is the integrated material removal from the workpiece surface, $R_{Preston}$ is the Preston coefficient (*i.e.* removal rate), P is the polishing pressure, $V_{tool\_workpiece}$ is the relative speed between the tool and workpiece and Δt is the dwell time.

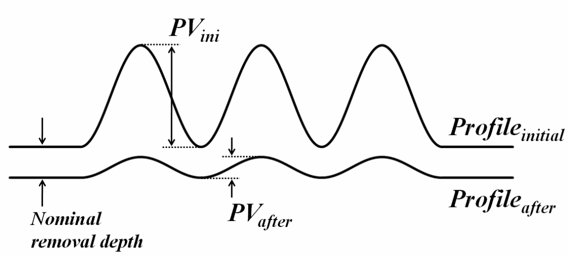

Fig. 5. The sinusoidal ripple profiles (before and after smoothing), which shows the values to determine the smoothing factor *SF* in Eq. (22)

For a given initial sinusoidal ripple magnitude PV_{ini}, the additional polishing pressure P_{add} on the peak is

$$P_{add} = P - P_{nominal} = \frac{1}{\frac{1}{\kappa_{elastic}} + \frac{1}{\kappa_{others}}} \cdot PV_{ini} \tag{19}$$

from Eq. (12). Then, for a dwell time Δt, the decrease in the ripple magnitude ΔPV is calculated using Eq. (18) as

$$\Delta PV = PV_{ini} - PV_{after} = R_{Preston} \cdot P_{add} \cdot V_{tool\_workpiece} \cdot \Delta t \quad . \tag{20}$$

In order to normalize ΔPV, the nominal removal depth (*i.e.* removal depth from the nominal pressure) is used as

$$nominal\_removal\_depth = R_{Preston} \cdot P_{nominal} \cdot V_{tool\_workpiece} \cdot \Delta t \ . \tag{21}$$

Using Eq. (19), (20) and (21), the smoothing factor *SF* is defined as

$$SF \equiv \frac{\Delta PV}{nominal\_removal\_depth} = \frac{1}{P_{nominal} \cdot (\frac{1}{\kappa_{elastic}(\omega)} + \frac{1}{\kappa_{others}})} \cdot PV_{ini} \ . \tag{22}$$

This definition for the smoothing factor in Eq. (22) turns out to be very useful, because it can be expressed as a linear function in *SF vs.* PV_{ini} space. For instance, the smoothing speed (*i.e.* the ripple magnitude decrease per unit nominal removal depth) can be easily calculated for a given initial ripple magnitude.

Because the real smoothing effect may be affected by other complex factors such as the shear stiffness characteristics of polishing pads and wrapping materials (*e.g.* the diaphragm in Fig. 2) and the fluid dynamics of polishing compounds, the theoretical smoothing model in Eq. (22) was parameterized using two parameters, C_1 and C_2, to fit the measured data. The first parameter C_1 represents κ_{others} and other unknown effects which may change the slope of the linear *SF* function. As the PV_{ini} becomes smaller and smaller the fluid dynamics of the polishing compound may begin to limit the smoothing action. This can give a limiting minimum ripple magnitude PV_{min} of the ripple, which means no more smoothing occurs below PV_{min}. This can be represented as an x-intercept C_2 in *SF vs.* PV_{ini} space.

The resulting parametric smoothing model for the RC lap is

$$SF \equiv \frac{1}{P_{nominal} \cdot (\frac{1}{\kappa_{elastic}(\omega)} + \frac{1}{C_1})} \cdot (PV_{ini} - C_2) \tag{23}$$

where C_1 is the slope correction parameter and C_2 is the x-intercept parameter. Because this is a linear function, these two parameters can be easily determined in practice by performing a few smoothing runs using a given polishing tool.

We acknowledge that, at the other extreme range where the *PV* becomes large, the RC lap may not fully deform to the ripple (*i.e.* partial contact [9]) and only touch some high portions of the ripple. Thus, beyond a certain PV_{max}, *SF* function is not a function of PV_{ini} anymore, but will be a constant.

In summary, the smoothing factor *SF* was defined to describe the smoothing effect of the RC lap. For a given RC lap structure the smoothing action is conveniently represented by a linear function in *SF vs.* PV_{ini} space. In order to include other unknown factors, which affect the smoothing action, the smoothing model was parameterized with two parameters.

4. Experimental verification of the parametric smoothing model

4.1 Experimental set-up

Two identical sets of experiments using a conventional pitch tool and RC lap were designed to verify the parametric smoothing model. Because a pitch tool is known for its superb smoothing effect, it is a good reference for the smoothing action comparison [23]. Pitch can also be regarded as an extreme of visco-elastic non-Newtonian fluids. It almost acts like a solid during the tool motion time period (*e.g.* ~seconds). However, for very long time periods (*e.g.* ~hours), it flows to fit the surface. Details of the experimental set-up are provided in Table. 1.

Table 1. Experimental set-up for the smoothing experiment

	Pitch tool	RC lap
Tool diameter	100mm	100mm
Aluminum back plate thickness	20mm	20mm
Elastic material	Pitch	Silly-Putty™
Elastic material thickness, *L*	8mm	8mm
Wrapping material	N/A	Bellofram™ diaphragm
Polishing interface	Pitch itself	0.5mm thick LP-66 (polyurethane pad)

A sinusoidal ripple with spatial frequency ξ=1/12=0.085mm^{-1} and *PV*=~0.4μm was generated on 250mm diameter Pyrex workpieces as shown in Fig. 6 (right). A specially designed pitch tool was used to generate the ripples as shown in Fig. 6 (left). This ripple generating pitch tool was made by pressing the warm pitch tool on a plastic mandrel board with many grid holes. By gently stroking the ripple generating pitch tool on the workpieces, sinusoidal ripples were generated without sharp cliff-like features in the ripple, which could have limited the measurement accuracy (*e.g.* the unwrapping problem of a phase shifting interferometric test).

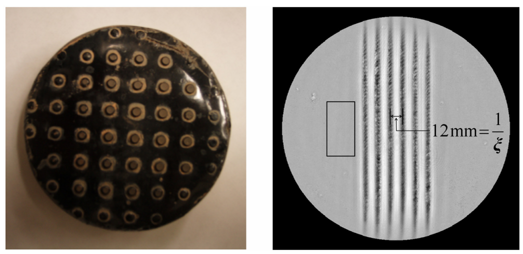

Fig. 6. The ripple generating pitch tool with a grid of circles (left) and a grey scale surface map of the Pyrex substrate with sinusoidal ripples and reference area to measure the nominal removal depth in a rectangular box (right).

The pitch tool and RC lap were run with an orbital tool motion on the workpieces. The change of the ripple magnitude, *ΔPV,* and the nominal removal depth in the rectangular reference area in Fig. 6 (right) were measured. These experiments were repeated until the magnitude of the ripples did not decrease anymore (*i.e.* the end of the smoothing effect). More detail of the tool operating condition is presented in Table. 2.

Table 2. Operating condition for the pitch tool and RC lap

Workpiece	250mm diameter Pyrex
Tool motion	Orbital tool motion (w/ 30mm orbital radius)
Tool motion speed	94.2mm/sec (*i.e.* 30RPM)
Nominal tool pressure	2500 Pascal (*i.e.* 0.36PSI)
Polishing compound	Rhodite 906 (Cerium based)
Polishing compound particle size	~2μm

Based on the pitch tool and RC lap information in Table 1 and 2, the compressive stiffness $\kappa_{elastic}$ for the parametric smoothing model was calculated using Eq. (13) as

$$Pitch\ tool: \quad \kappa_{elastic}(\omega) = \frac{E'(\omega)}{L \cdot \cos\delta(\omega)} = \frac{2.5\times10^{9}}{8\times10^{3}\cdot 1} = 312500\ [Pa/\mu m] \tag{24}$$

$$RC\ lap: \quad \kappa_{elastic}(\omega) = \frac{E'(\omega)}{L \cdot \cos\delta(\omega)} = \frac{0.003\times10^{9}}{8\times10^{3}\cdot 1} = 375\ [Pa/\mu m] \tag{25}$$

and used in the parametric smoothing model, Eq. (23). For the storage modulus (*i.e.* Young's modulus) of the pitch tool, a typical value 2.5 GPa was assumed [24]. The actual storage modulus of the pitch is a function of many factors such as the temperature of pitch. This uncertainty becomes a part of the first parameter C_1 in the parametric smoothing model. Also, pitch is practically a solid within the orbital tool motion time scale. Thus, the phase lag δ was assumed as 0. For the RC lap, as shown in Section 3.2, storage modulus E' =0.003GPa and phase lag δ=0 was used.

4.2 Measured smoothing factor for pitch tool and RC lap

The ripples were measured using an Intellium™ Fizeau interferometer by ESDI. Because the actual ripples were not ideal sinusoidal curves, an averaged peak-to-valley value using >90% and <90% height values was used to calculate the *PV*. Some measured profiles are presented in Fig. 7 as an example. The decrease in ripple magnitude as the smoothing time gets longer is clearly shown. The pitch tool (left) smoothes out the ripples much quicker than the RC lap (right).

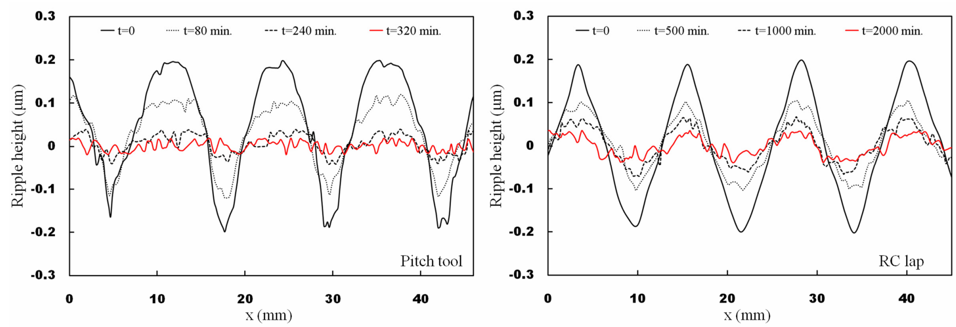

Fig. 7. Measured ripple profiles as tool smoothes out the ripples: pitch tool (left) and RC lap (right) (*Note:* The initial ripple magnitude *PV* was about 0.4µm for both cases.)

Approximately 100 smoothing experiments were performed. The measured ΔPV values were normalized by the measured nominal removal depth to calculate the smoothing factor *SF* as explained in Section 3.3. The experiments were performed until no more reduction in the ripple magnitude (*i.e.* smoothing factor *SF*=~0) was observed. The experimental results are plotted in Fig. 8.

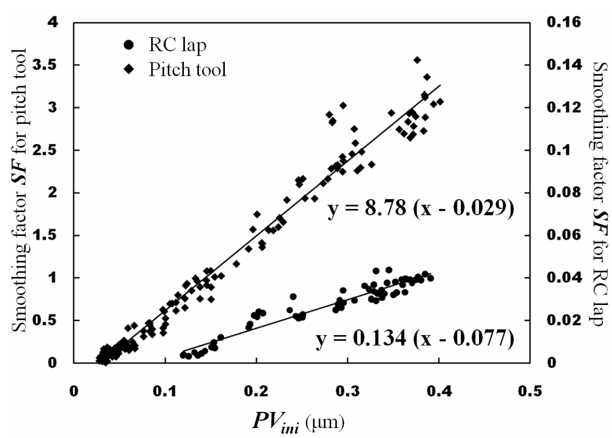

Fig. 8. Measured smoothing factor *SF vs.* initial ripple magnitude P_{ini} for pitch tool and RC lap. (*Note:* The solid line represents the linear fit using the parametric smoothing model. Two parameters C_1 and C_2 were used to fit the measured data as shown in Table. 3.)

Two parameters C_1 and C_2 in the parametric smoothing model were used to fit the measured data as shown in Fig. 8. The first parameter C_1 was used to match the slope of the data. The second parameter C_2 was used to match the x-intercept of the data, which is the parametric representation of the smoothing limit PV_{min} mentioned in Section 3.3. The fitted parameter values are presented in Table 3 with the calculated compressive stiffness $\kappa_{elastic}$ values from Eq. (24) and (25).

Table 3. Compressive stiffness $\kappa_{elastic}$ and two parameter values for parametric smoothing model

	$\kappa_{elastic}$ (Pa/μm)	C_1 (Pa/μm)	C_2 (μm)
Pitch tool	312500	23608	0.029
RC lap	375	3141	0.077

The linear trend predicted by the parametric smoothing model in Eq. (23) was successfully verified. The C_1 for the pitch tool case was much smaller (~0.08 times) than the compressive stiffness $\kappa_{elastic}$ of the pitch, so that the slope of the parametric *SF* function was smaller than the slope solely based on the pitch stiffness itself. One possible explanation for this result may be the polishing compound liquid layer between the pitch surface and the workpiece, which may change the total compressive stiffness. However, the pitch tool still shows ~66 times faster (*i.e.* ~66 times steeper *SF* slope) smoothing action than the RC lap. The limiting magnitude of the ripple PV_{min} was measured experimentally and fitted using the second parameter C_2. The pitch tool was able to smooth out the ripples down to PV_{min} =~0.029μm.

In contrast, the C_1 for the RC lap was much larger (~8.4 times) compared to the compressive stiffness of the Silly-Putty™, so that the slope of the *SF* graph was almost entirely determined by the compressive stiffness of the SP. This may result from the fact that the contributions to the total stiffness κ_{total} from the relatively very thin (0.5mm) polyurethane pad and wrapping material were much smaller than the contribution from the SP. Also, the PV_{min} was measured and fitted using C_2. The RC lap smoothed out the ripples down to PV_{min} =~0.077μm. A steeper slope for faster smoothing action can be achieved simply by using different non-Newtonian fluids with higher storage modulus values. Also, changing the thickness L of the elastic material is expected to result in a steeper *SF* function, because $\kappa_{elastic}$ is a direct function of L as shown in Eq. (13). These additional modalities, including the ripple spatial frequency, which changes the applied stress frequency, are planned to be investigated in future studies [25].

5. Concluding remarks

A parametric smoothing model was developed to quantitatively describe the smoothing effects of the RC laps [18]. A convenient normalized smoothing factor *SF* was defined using two parameters for the parametric smoothing model. A series of experiments were performed to verify the parametric smoothing model. The linear trend of the *SF* function was clearly verified by the experimental results. The limiting ripple magnitude PV_{min} from the smoothing actions and change of slope due to the total compressive stiffness of the whole tool structure were also measured and successfully fitted using those two parameters.

The RC lap, which showed a highly deterministic removal rate (*i.e.* <10% stability) and superb surface finish (*e.g.* <1nm RMS surface roughness) [18], can be used efficiently and deterministically for large precision optics fabrications. It will contribute to the realization of some next generation optical systems which usually have hundreds of meter-class aspheric mirrors (*e.g.* Thirty Meter Telescope [13] and Laser Inertial Fusion Engine [15]) or large off axis mirrors (*e.g.* 8.4meter Giant Magellan Telescope mirrors [12]).

Acknowledgments

We acknowledge that this work was supported by the Optical Engineering and Fabrication Facility of the College of Optical Sciences at the University of Arizona. We thank Marty Valente (Optical Engineering and Fabrication Facility), Anastacia Manuel (College of Optical Sciences), Anoopoma Bhowmik (College of Optical Sciences) and Brian Cuerden (Steward Observatory) at the Univ. of Arizona for assistance in the final manuscript preparation.

The measured data in Fig. 4 was available in this manuscript with the permission of Journal of Materials Research. We thank the journal and A. C. Fischer-Cripps, the author of the original manuscript.

Note: A US provisional patent was filed for the RC lap in this journal article.

APPENDIX C

Static Tool Influence Function for Fabrication Simulation of Hexagonal Mirror Segments for Extremely Large Telescopes

Dae Wook Kim and Sug-Whan Kim

Journal article published in ***Optics Express***

2005

Copyright Transfer Agreement

The Optical Society of America considers this requested use of its copyrighted materials to be allowed under the OSA Author Agreement submitted by the requester on acceptance for publication of his/her manuscript. It is requested that a complete citation of the original material be included in any publication.

Delois Millner October 22, 2009
Delois Millner Date
Authorized Agent, Optical Society of America

Static tool influence function for fabrication simulation of hexagonal mirror segments for extremely large telescopes

Dae Wook Kim and Sug-Whan Kim

Space Optics Laboratory, Department of Astronomy, Yonsei University, Seoul, Republic of Korea
Institute of Space Science and Technology, Yonsei University, Seoul, Republic of Korea
Center for Space Astrophysics, Yonsei University, Seoul, Republic of Korea
letter2dwk@hotmail.com, skim@galaxy.yonsei.ac.kr

Abstract: We present a novel simulation technique that offers efficient mass fabrication strategies for 2m class hexagonal mirror segments of extremely large telescopes. As the first of two studies in series, we establish the theoretical basis of the tool influence function (TIF) for precessing tool polishing simulation for non-rotating workpieces. These theoretical TIFs were then used to confirm the reproducibility of the material removal foot-prints (measured TIFs) of the bulged precessing tooling reported elsewhere. This is followed by the reverse-computation technique that traces, employing the simplex search method, the real polishing pressure from the empirical TIF. The technical details, together with the results and implications described here, provide the theoretical tool for material removal essential to the successful polishing simulation which will be reported in the second study.

OCIS codes: (220.0220) Optics design and fabrication; (220.1250) Aspherics; (220.4610) Optics fabrication; (220.5450) Polishing

References and links

1. T. Andersen, A. L. Ardeberg, J. Beckers, A. Goncharov, M. Owner-Petersen, H. Riewaldt, R. Snel, and D. D. Walker, “The Euro50 Extremely Large Telescope,” in *Future Giant Telescopes*, J. R. P. Angel and R. Gilmozzi, eds., Proc. SPIE **4840**, 214-225 (2003).
2. D. D. Walker, A. P. Doel, R. G. Bingham, D. Brooks, A. M. King, G. Peggs, B. Hughes, S. Oldfield, C. Dorn, H. McAndrews, G. Dando, and D. Riley, “Design Study Report: The Primary and Secondary Mirrors for the Proposed Euro50 Telescope” (2002), http://www.zeeko.co.uk/papers/dl/New%20Study%20Report%20V%2026.pdf.
3. T. Anderson, A. Ardeberg, and M. Owner-Perterson, “EURO50: Design study of a 50m adaptive optics telescope” (2003), http://www.astro.lu.se/~torben/euro50/publications/white_book80.pdf.
4. P. Dierickx, “Optical fabrication in the large,” in *Proceedings of the Backaskog workshop on extremely large telescopes*, T. Andersen, A. Ardeberg, and R. Gilmozzi, eds., no. 57 of ESO conference and workshop proceedings (Lund Observatory and European Southern Observatory, Munchen, 2000), pp. 224-236.
5. H. M. Martin, D. S. Anderson, J. R. P. Angel, R. H. Nagel, S. C. West, and R. S. Young, "Progress in the stressed-lap polishing of a 1.8-m f/1 mirror," in *Advanced Technology Optical Telescopes IV*, L. D. Barr, Ed., Proc. SPIE **1236**, 682-690 (1990).
6. A. R. Jones and J. W. Rupp, "Rapid optical fabrication with computer-controlled optical surfacing," Opt. Eng. **30**, 1962-1967 (1991).
7. T. S. Mast and J. E. Nelson, "Fabrication of large optical surfaces using a combination of polishing and mirror bending," in *Advanced Technology Optical Telescopes IV*, L. D. Barr, Ed., Proc. SPIE **1236**, 670-681 (1990).
8. L. N. Allen, "Progress in ion figuring large optics," in *Laser-Induced Damage in Optical Materials*, H. E. Bennett, A. H. Guenther, M. R. Kozlowski, B. E. Newnam, and M. J. Soileau, Eds., Proc. SPIE **2428**, 237-247 (1995).
9. F. A. Carbone and D. A. Markle, "Combining ion figuring and SPSI testing to produce a high-quality aspheric 18-inch-diameter f/2 mirror," in *Optical Manufacturing and Testing*, V. J. Doherty D. V. M. and H. P. Stahl, Eds., Proc. SPIE **2536**, 89-98 (1995).
10. K. Beckstette, M. Küchel, and E. Heynacher, "Large mirror figuring and testing," Astrophys Space Sci. **160**, 207-214 (1989).

#6258 - $15.00 US Received 10 January 2005; revised 27 January 2005; accepted 27 January 2005

11. T. K. Korhonen and T. Lappalainen, "Computer-controlled figuring and testing," in *Advanced Technology Optical Telescopes IV*, L. D. Barr, Ed., Proc. SPIE **1236**, 691-694 (1990).
12. T. S. Mast, J. E. Nelson, and G. E. Sommargren, "Primary mirror segment fabrication for CELT," in *Optical Design, Materials, Fabrication, and Maintenance*, P. Dierickx, ed., Proc. SPIE **4003**, 43-58 (2000).
13. D. D. Walker, A. T. Beaucamp, R. G. Bingham, D. Brooks, R. Freeman, S. W. Kim, A. King, G. McCavana, R. Morton, D. Riley, and J. Simms, "Precessions aspheric polishing : - new results from the development programme," in *Optical Manufacturing and Testing V*, H. P. Stahl, ed., Proc. SPIE **5180**, 15-28 (2004).
14. D. D. Walker, D. Brooks, A. King, R. Freeman, R. Morton, G. McCavana, and S. W. Kim, "The 'Precessions' tooling for polishing and figuring flat, spherical and aspheric surfaces", Opt. Express, **11**, 958-964 (2003).
15. D. D. Walker, A. T. Beaucamp, D. Brooks, V. Doubrovski, M. D. Cassie, C. Dunn, R. R. Freeman, A. King, M. Libert, G. McCavana, R. Morton, D. Riley, and J. Simms, "New results from the Precessions polishing process scaled to larger sizes," in *Optical Fabrication, Metrology, and Material Advancements for Telescopes*, E. Atad-Ettedgui and P. Dierickx, eds., Proc. SPIE **5494**, 71-80 (2004).
16. D. D. Walker, A. T. Beaucamp, D. Brooks, V. Doubrovski, M. D. Cassie, C. Dunn, R. R. Freeman, A. King, M. Libert, G. McCavana, R. Morton, D. Riley, and J. Simms, "Recent developments of Precessions polishing for larger components and free-form surfaces," in *Current Developments in Lens Design and Optical Engineering V*, P. Z. Mouroulis, W. J. Smith, and R. B. Johnson, eds., Proc. SPIE **5523**, 281-289 (2004).
17. D. W. Kim, Space Optics Laboratory, Yonsei University, 134 Shinchon-dong, Sudaemun-gu, Seoul, Republic of Korea and S. W. Kim are preparing a manuscript to be called "Novel polishing algorithm for fabrication simulation of 2m class hexagonal mirror segments for extremely large telescopes."
18. H. Lee, Space Optics Laboratory, Yonsei University, 134 Shinchon-dong, Sudaemun-gu, Seoul, Republic of Korea and S. W. Kim are preparing a manuscript to be called "Non-linear variation of tool influence function in precessing sub-diameter tool polishing."
19. J. C. Lagarias, J. A. Reeds, M. H. Wright, and P. E. Wright, "Convergence Properties of the Nelder-Mead Simplex Method in Low Dimensions," SIAM Journal of Optimization, **9**, 112-147 (1998).

1. Introduction

The Extremely Large Telescopes (ELTs), currently being planned, are to have hexagonal segmented primary mirrors of about 1-2m in diameter [1]. The target specifications of these ELT primary mirrors are highly challenging. Examples may include the EURO50 primary mirror system consisted of 618 hexagonal segments. Each segment is to have the surface form accuracy of better than 18nm peak-to-valley [2]. The primary mirror system is to be phased and aligned to the precision of about 10-20nm rms [3]. The continuing change in slope difference between the target shape and the best-fit sphere serves as the primary cause to the fabrication difficulty. This is expressed as fabrication difficulty index *dy* [4] in Table 1. Mathematically, *dy* is defined as

$$dy = \frac{8(f/D)^3}{k}, \tag{1}$$

where k is the conic constant of the primary mirror, f the focal length, and D the diameter of the primary mirror. The table shows that, even without considering mass fabrication requirement, the EURO50 primary segment (dy=4.92) is about 5.3 times more difficult than the KECK primary segment (dy=26.1).

In the midst of many fabrication technologies developed over the last few decades [5-11], the ion beam figuring technique [8,9] has demonstrated success at producing large hexagonal mirror of about 15nm rms [4]. However, the technique has extremely low material removal rates and consequently suffers from the long delivery schedule. A study indicated that using 6 ion figuring chambers would take about 8 years to complete the 1080 0.5m diameter segments for CELT [12]. This does not even include the requirement of a number of the precision grinding and pre-polishing machines for producing the input mirror surfaces, of sub-micron accuracy, to the ion figuring machines. This demonstrates the critical limitation of its general applicability to the mass fabrication requirement for ELT primary mirror segments of up to 2m in diameter, within the reasonable delivery time of 2-3 years.

#6258 - $15.00 US Received 10 January 2005; revised 27 January 2005; accepted 27 January 2005

Table 1. Specifications of three ELTs and KECK primary mirrors

Telescope	Primary Mirror Diameter (m)	Primary Mirror f-ratio	Segment Size (m)	Conic Constant	No. of Segments	*dy*	Segment Shape
EURO50	50.4	f/0.85	2	-0.9994	618	4.92	Hexagonal
OWL	100	f/1.82 or f/1.5	1.6	0	3048	n/a	Hexagonal
CELT	30	f/1.50	0.5	-1.525	1080	17.7	Hexagonal
KECK	10	f/1.75	1.8	-1.644	36	26.1	Hexagonal

Among the many process elements, three are crucial for the successful deployment of efficient mass fabrication technique for ELT segmented mirrors. They are: i) low tooling overhead, ii) deterministic material removal and iii) embedded process control intelligence. The bulged precessing polishing process [13,14], recently introduced, may have potentials to bring greater improvement than earlier methods [5-11] for the three elements defined above. In particular, as it moves across the workpiece, the bulged precessing tool tends to conform its shape to the local surface. Additionally, by changing the tool pressure, a wide range of surface contact area is achieved between the tool and the workpiece using a single bonnet. Such flexible tooling ability, aided with a precision 7-axis (including workpiece rotation) CNC capability and the built-in process intelligence, demonstrated the p-v form accuracy of about 1μm for an on-axis ellipsoid of 500mm in diameter [15,16].

This process, as is of today, exhibits its limitation to immediate applicability for the fabrication of ELT primary mirror segments in terms of their size, the aforementioned target surface specification and the hexagonal shape. The production is further complicated with the mass fabrication requirement within the reasonable delivery schedule of 2-3 years. This gives rise to the need of an improved fabrication technique capable of processing the axially non-symmetric workpieces with even higher deterministic material removal controllability, added to the existing bulged precessing tooling.

Section 2 deals with the theoretical background of the static tool influence function (sTIF) for non-rotating workpieces and its experimental verification. This is followed by the reverse computation technique for the real polishing pressure exerted from the precessing tool bonnet system in Section 3. Section 4 summarizes the implications of this study in view of polishing simulation of hexagonal mirror segments for ELT. To this extent, the present technical development, reported here, lay the theoretical foundation for a new precession polishing simulation technique [17] that may offer an attractive solution to the challenging problems of mass fabrication of segmented mirrors for the ELT projects.

2. sTIF generation and verification

2.1. sTIF

For circularly symmetric rotating workpieces, the generalized equation of material removal (EMR) and the variable tool influence function (vTIF) are soon to be reported [18]. EMR is derived from the well-known Preston's relation expressed as

$$\Delta z = \kappa P V_T \Delta t, \tag{2}$$

where Δz is the integrated material removal from the workpiece surface, κ the removal coefficient of the segment material, P the polishing pressure, V_T the magnitude of relative speed between the tool and workpiece surface, and Δt the dwell time.

Earlier studies [13-16] showed that the precessing polishing process currently in service uses the measured TIFs of near Gaussian shapes to compute the required dwell time. That

Received 10 January 2005; revised 27 January 2005; accepted 27 January 2005
7 February 2005 / Vol. 13, No. 3 / OPTICS EXPRESS 912

method bypasses the need for prior knowledge of the relationship among the material removal (i.e., TIF), polishing pressure, and velocity inside the tool-workpiece contact area (polishing spot). Nevertheless, we note that the relationship serves as an invaluable aid to further the process development for the precessing tool polishing.

The very shape of measured TIFs supports speculation that the polishing pressure exerted by the bonnet system is likely to be near Gaussian. This view is further strengthened with the integrated velocity field that tends to be randomized by the tool precessing action over the dwell time. Thus, we take the approach, as depicted in Fig. 1(a), that the construction of theoretical TIF starts with a modified Gaussian function with standard deviation σ and maximum pressure P_T, such that

$$P = P_T(\exp(-\frac{\lambda^2}{2\sigma^2}))^{\psi}, \tag{3}$$

where λ is the distance between A and C, and ψ the modification coefficient. For non-rotating workpiece surfaces, the total relative speed V_T is the magnitude of the vector sum of the tool rotation $\overrightarrow{\mathbf{V_{TR}}}$ and the feed rate $\overrightarrow{\mathbf{V_{TF}}}$ shown in Fig. 1(b). This can be expressed as Eq. (4).

$$V_T = [(V_{TRx} + V_{TFx})^2 + (V_{TRy} + V_{TFy})^2]^{1/2} \tag{4}$$

Substituting Eq. (3) and (4) for P and V_T of Eq. (2), EMR for non-rotating workpieces is obtained as Eq. (5).

$$\Delta z = \kappa P_T(\exp(-\frac{\lambda^2}{2\sigma^2}))^{\psi}[(V_{TRx} + V_{TFx})^2 + (V_{TRy} + V_{TFy})^2]^{1/2}\Delta t \tag{5}$$

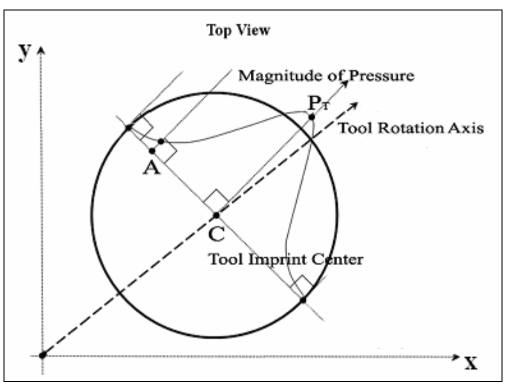

(a)

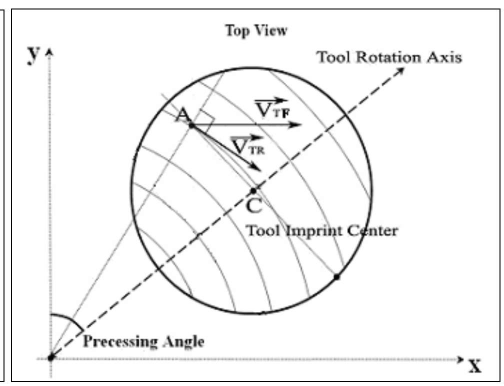

(b)

Fig. 1. (a) Gaussian pressure distribution and (b) velocity components overlaid onto concentric speed contours of tool rotation inside the polishing spot (tool-workpiece contact area)

Eq. (5) can produce a wide variety of sTIF depending on the input polishing parameters, including tool rpm (W_T), inclination angle (α) and tool pressure (P_T). A typical example of sTIF is shown in Fig. 2. Here we note the shape difference between the two sTIF cross-sectional profiles shown in Fig. 2(b); this being caused by the asymmetric velocity field effect with the fixed precessing angle as depicted in Fig. 1(b). This result re-confirms the report that the asymmetric tool velocity field is strongly tied with changes in precessing angle [18]. For this reason, three precessing angles separated by 120 degrees were used to generate circularly symmetric sTIF throughout this study.

#6258 - $15.00 US Received 10 January 2005; revised 27 January 2005; accepted 27 January 2005

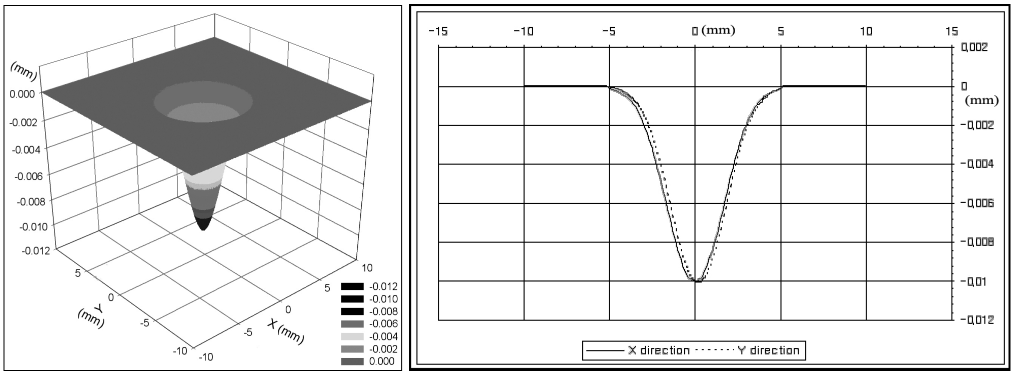

(a) (b)

Fig. 2. (a) Three dimensional view of sTIF and (b) cross-sectioned profiles of sTIF in X and Y axis (Δt=6 sec, W_T=1000 rpm, P_T=0.013 Mpa, α=15 degrees)

2.2. Experimental verification of sTIF

These theoretical TIFs were used to re-produce the characteristics of the measured [13,14] TIFs. First, Fig. 3 shows a family of 10 theoretical TIFs generated with the tool rotation range of 100-1000 rpm, with all other parameters fixed. It re-produced the measured material removal depth [14] versus the tool rotation. This implies that the material removal controllability can be achieved, both in simulation and in actual polishing, by altering the tool rotation.

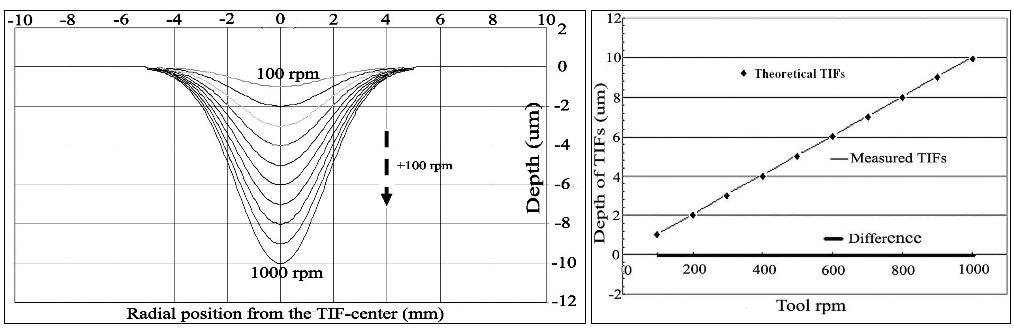

(a) (b)

Fig. 3. (a) Cross-sectional profiles of sTIFs (100 - 1000 tool rpm) and (b) depth of measured [14] and theoretical sTIFs

Second, we then tested the effects of workpiece attack (i.e. inclination) angle onto TIF as shown in Fig. 4. Whilst exhibiting the minor difference of about 30nm over the inclination range of 14-18 degrees, the overall diagram shows the theoretical TIFs following the measurement [13] very closely.

Third, we generated a family of theoretical TIFs with the tool pressure ranging from 0.0130 Mpa to 0.0214 Mpa, while holding the other control parameters fixed. The measured [14] and theoretical TIFs are presented in Fig. 5. Once again, the measured material removal depth and tool imprint radius were well reproduced with the theoretical TIFs. The minor difference in the cross-sectional profile width of both theoretical and experimental TIFs at $P_T \geq 0.0179$ Mpa can be corrected by either adjusting the parameters of the modified Gaussian function in Eq. (3), or altering the tool material (i.e. polishing cloth).

#6258 - $15.00 US Received 10 January 2005; revised 27 January 2005; accepted 27 January 2005

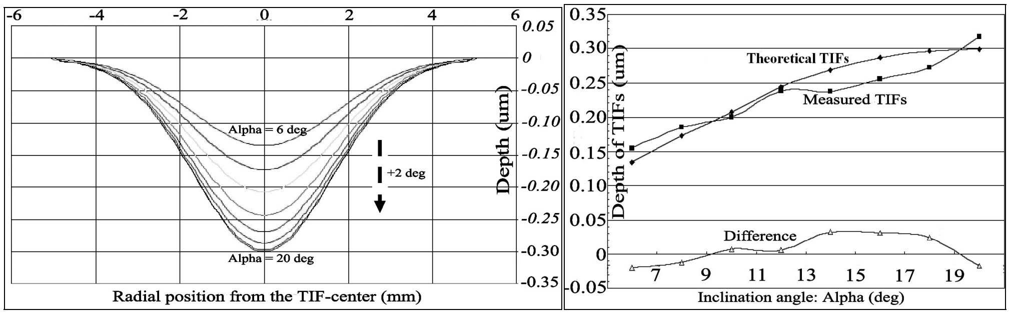

(a) (b)

Fig. 4. (a) Cross-sectional profiles of sTIFs (α: 6 - 20 degrees) and (b) depth of measured [13] and theoretical sTIFs

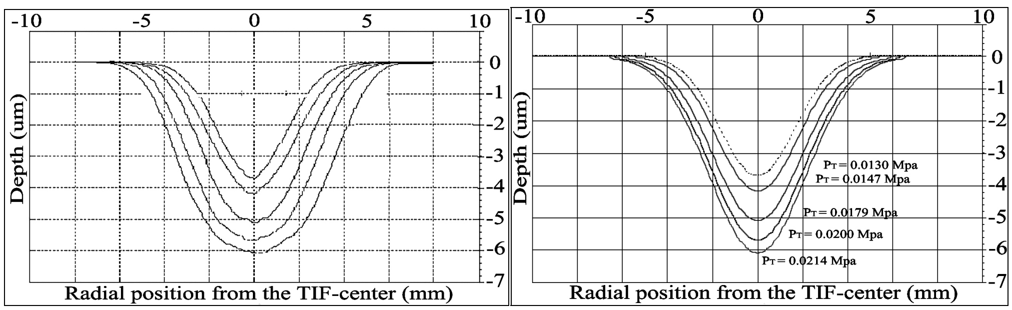

(a) (b)

Fig. 5. (a) Measured sTIFs [14] and (b) theoretical sTIFs (P_T: 0.0130 - 0.0214 Mpa)

3. Reverse computation of actual polishing pressure from TIF

The precessing tool bonnet is a complex mechanical system of pressurized membrane, cement, and polishing cloth. Therefore, an accurate, mechanical model of the bonnet system is not easily obtainable from straightforward integration of its mechanical element characteristics. A simpler way of characterizing and, hence, optimizing the bonnet system, is to establish a computational process to derive the actual polishing pressure distribution for a set of chosen tooling parameters, from combination of the empirical TIFs and theoretical model.

The first step of the computation process for the actual polishing pressure $P_{E(i)}$ starts with Eq. (6) which is a re-arranged form of Eq. (5). $P_{E(i)}$ was calculated for 41 data points (N=41, $0 \leq i \leq 40$) at the interval of $\Delta\lambda$=0.5mm along the TIF cross-sectional profile of 20mm in diameter. This is the actual polishing pressure that the bonnet system exerts inside the polishing spot.

$$P_{E(i)} = \frac{\Delta z_{(i)}}{\kappa[(V_{TRx(i)} + V_{TFx})^2 + (V_{TRy(i)} + V_{TFy})^2]^{1/2}\Delta t} \tag{6}$$

The exact tooling parameters of the measured TIF [14] were not known, but since the shape proximity of both experimental and theoretical TIFs are well demonstrated in Fig. 5, the five theoretical TIFs in Fig. 5(b) were used as input Δz data instead. The resulting (computed) pressure profiles are depicted in Fig 6(a). Here we re-confirm the aforementioned expectation that, after the removal of tool speed and dwell time effects, the real polishing pressure exerted by the bonnet has edgeless near Gaussian shapes. This implies that the Gaussian pressure

#6258 - $15.00 US Received 10 January 2005; revised 27 January 2005; accepted 27 January 2005

distribution inside the polishing spot is a valid approximation for any empirical TIFs of near Gaussian shapes in precessing tool polishing.

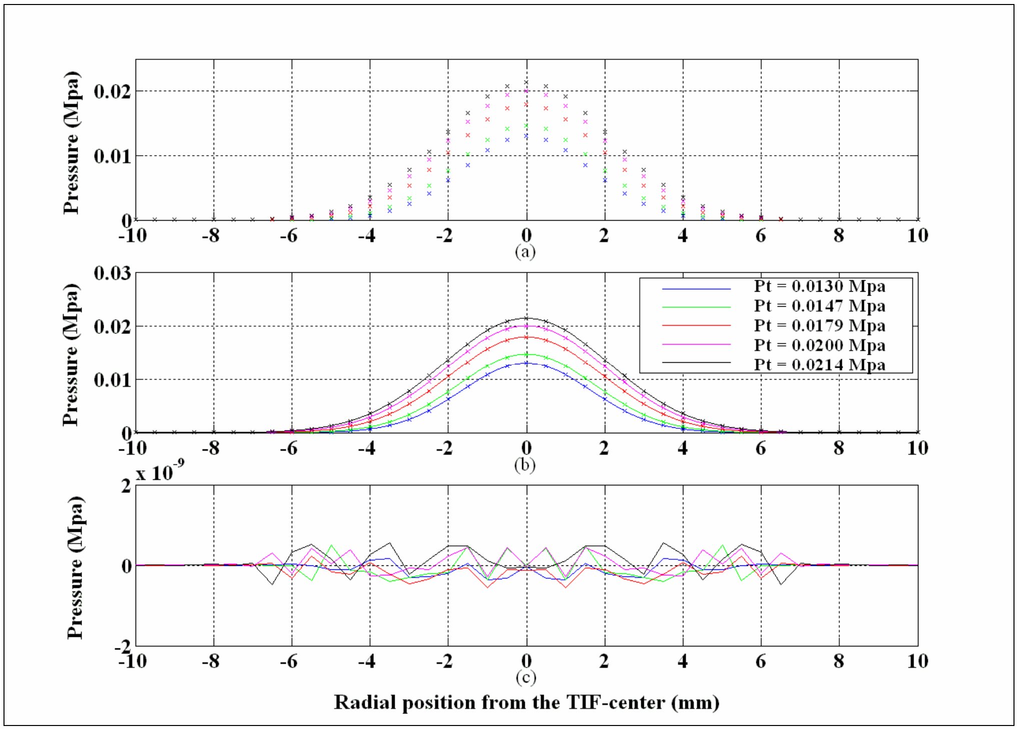

Fig. 6. (a) Empirical polishing pressure data (41 data points) inverse-computed from TIFs, (b) theoretical polishing pressure expressed with modified Gaussian function fitted to the data and (c) residual pressure difference between the data and the fitted functions

The second step is to fit the modified Gaussian function of Eq. (3) to the empirical polishing pressure distributions, $P_{E(i)}$, in Fig. 6(a). For each computation data point of $0 \leq i \leq 40$, the pressure difference $d_{(i)}$ between $P_{E(i)}$ (computed from TIF in Fig. 5(b)) and $P_{(i)}$ (theoretical polishing pressure model as in Eq. (3)), is expressed as Eq. (7). We then defined the standard deviation of the pressure differences σ_d as Eq. (8). The simplex search method [19] was used for the function fitting algorithm, which searches for the optimum parameter set (P_T, σ, and ψ) until it reaches the minimum standard deviation σ_d.

$$d_{(i)}(P_T, \sigma, \psi) = (P_{E(i)} - P_{(i)}) \tag{7}$$

$$\sigma_d(P_T, \sigma, \psi) = [\frac{1}{N}\sum_{i=1}^{N}(d_{(i)} - \bar{d})^2]^{1/2} = \{\frac{1}{N}\sum_{i=1}^{N}[d_{(i)} - (\frac{1}{N}\sum_{i=1}^{N}d_{(i)})]^2\}^{1/2} \tag{8}$$

Table 2 lists the optimum parameter sets for the resulting Gaussian functions shown in Fig. 6(b) and the fitting accuracy in terms of the standard deviation σ_d, which represents the pressure difference plotted in Fig. 6(c). Both Table 2 and Fig. 6(c) show the extreme accuracy of the function fit, since the standard deviation of the pressure differences σ_d is on the order of e-10 Mpa. This shows that this theoretical model can be successfully used to optimize the bonnet system, by unlocking the relationship between TIF, pressure and velocity in precessing tool polishing. It is worth noting that if the TIF shapes depart significantly from the modified Gaussian function used in this study, the accuracy of the function fit may be degraded.

#6258 - $15.00 US
Received 10 January 2005; revised 27 January 2005; accepted 27 January 2005

Table 2. Optimized parameters (P_T, σ, and ψ) and standard deviation σ_d for the modified Gaussian function fitting

Maximum depth of input TIF (Fig. 5(b))	Peak polishing pressure (reverse calculated)	Modified Gaussian function parameters after optimized fitting			Standard deviation representing minimum fitting errors
		P_T	σ	ψ	σ_d
(um)	*(Mpa)*	*(Mpa)*	*(mm)*	*dimensionless*	*(Mpa)*
3.704	0.0130	0.0130	18.356	124.5128	1.8165e-10
4.185	0.0147	0.0147	19.3907	122.9192	2.3265e-10
5.090	0.0179	0.0179	19.4704	101.8420	2.1121e-10
5.682	0.0200	0.0200	17.4415	73.1725	2.2649e-10
6.077	0.0214	0.0214	19.2835	83.6167	2.4838e-10

4. Concluding remarks

As the first of two studies in series, the theoretical basis for a new three dimensional polishing simulation technique is reported for efficient fabrication of 2m class hexagonal segment mirrors for ELT projects. The theoretical static tool influence function (sTIF) of the bulged precessing tooling was established, and its applicability for polishing simulation was verified by comparing the computer generated (theoretical) sTIFs against the measured TIFs [13,14] for various polishing parameters. We then report a reverse computation technique to obtain the actual polishing pressure from the combination of measured TIF and the theoretical model. The results are useful for optimizing the bonnet system by unlocking the relationship between TIF, pressure and velocity in precessing tool polishing. Using the theoretical TIF studied here, a new fabrication simulation technique for 2m class hexagonal segmented mirrors for the EURO50 telescope project will be reported in the second study [17] in the series.

Acknowledgments

We acknowledge the financial support under the KISTEP Grant 2004-02622. We thank Tom Zobrist who guarded us against a number of unclarities in the final manuscript preparation.

APPENDIX D

Parametric Modeling of Edge Effects for Polishing Tool Influence Functions

Dae Wook Kim, Won Hyun Park, Sug-Whan Kim

and James H. Burge

Journal article published in ***Optics Express***

2009

Copyright Transfer Agreement

The Optical Society of America considers this requested use of its copyrighted materials to be allowed under the OSA Author Agreement submitted by the requester on acceptance for publication of his/her manuscript. It is requested that a complete citation of the original material be included in any publication.

Delois Millner October 22, 2009
Delois Millner Date
Authorized Agent, Optical Society of America

Parametric modeling of edge effects for polishing tool influence functions

Dae Wook Kim,[1*] Won Hyun Park,[1,2] Sug-Whan Kim[2] and James H. Burge[1]

[1]*College of Optical Sciences, University of Arizona, 1630 E. University Blvd, Tucson, Arizona 85721, USA*
[2]*Space Optics Laboratory, Dept. of Astronomy, Yonsei University, 134 Sinchon-dong, Seodaemun-gu, Seoul 120-749, Republic of Korea*
[*]*Corresponding author: letter2dwk@hotmail.com*

Abstract: Computer controlled polishing requires accurate knowledge of the tool influence function (TIF) for the polishing tool (i.e. lap). While a linear Preston's model for material removal allows the TIF to be determined for most cases, nonlinear removal behavior as the tool runs over the edge of the part introduces a difficulty in modeling the edge TIF. We provide a new parametric model that fits 5 parameters to measured data to accurately predict the edge TIF for cases of a polishing tool that is either spinning or orbiting over the edge of the workpiece.

OCIS codes: (220.0220) Optics design and fabrication; (220.4610) Optics fabrication; (220.5450) Polishing

References and links

1. M. Johns, "The Giant Magellan Telescope (GMT)," Proc. SPIE **6986**, 698603 (2008).
2. M. Clampin, "Status of the James Webb Space Telescope (JWST)," Proc. SPIE **7010**, 70100L (2008).
3. R. Aspden, R. McDonough, and F. R. Nitchie, Jr, "Computer assisted optical surfacing," Appl. Opt. **11**, 2739-2747 (1972).
4. R. E. Wagner and R. R. Shannon, "Fabrication of aspherics using a mathematical model for material removal," Appl. Opt. **13**, 1683-1689 (1974).
5. D. J. Bajuk, "Computer controlled generation of rotationally symmetric aspheric surfaces," Opt. Eng. **15**, 401-406 (1976).
6. R. A. Jones, "Grinding and polishing with small tools under computer control," Opt. Eng. **18**, 390-393 (1979).
7. R. A. Jones, "Computer-controlled polishing of telescope mirror segments," Opt. Eng. **22**, 236-240 (1983).
8. R. A. Jones, "Computer-controlled optical surfacing with orbital tool motion," Opt. Eng. **25**, 785-790 (1986).
9. J. R. Johnson and E. Waluschka, "Optical fabrication-process modeling-analysis tool box," Proc. SPIE **1333**, 106-117 (1990).
10. R. A. Jones and W. J. Rupp, "Rapid optical fabrication with CCOS," Proc. SPIE **1333**, 34-43 (1990).
11. D. W. Kim and S. W. Kim, "Static tool influence function for fabrication simulation of hexagonal mirror segments for extremely large telescopes," Opt. Express. **13**, 910-917 (2005).
12. D. D. Walker, A. T. Beaucamp, D. Brooks, V. Doubrovski, M. Cassie, C. Dunn, R. Freeman, A. King, M. Libert, G. McCavana, R. Morton, D. Riley, and J. Simms, "New results from the Precessions polishing process scaled to larger sizes," Proc. SPIE **5494**, 71-80 (2004).
13. E. Luna-Aguilar, A. Cordero-Davila, J. Gonzalez Garcia, M. Nunez-Alfonso, V. H. Cabrera-Pelaez, C. Robledo-Sanchez, J. Cuautle-Cortez, and M. H. Pedrayes-Lopez, "Edge effects with Preston equation," Proc. SPIE **4840**, 598-603 (2003).
14. A. Cordero-Davila, J. Gonzalez-Garcia, M. Pedrayes-Lopez, L. A. Aguilar-Chiu, J. Cuautle-Cortes, and C. Robledo-Sanchez, "Edge effects with the Preston equation for a circular tool and workpiece," Appl. Opt. **43**, 1250-1254 (2004).
15. B. C. Crawford, D. Loomis, N. Schenck, and B. Anderson, Optical Engineering and Fabrication Facility, University of Arizona, 1630 E. University Blvd, Tucson, Arizona 85721, (personal communication, 2008).
16. D. W. Kim, College of Optical Sciences, University of Arizona, 1630 E. University Blvd, Tucson, Arizona 85721, W. H. Park, and J. H. Burge are preparing a manuscript to be called "Edge tool influence function model including tool stiffness and bending effects."

#106335 - $15.00 USD Received 13 Jan 2009; revised 3 Mar 2009; accepted 20 Mar 2009; published 25 Mar 2009

17. D. W. Kim, College of Optical Sciences, University of Arizona, 1630 E. University Blvd, Tucson, Arizona 85721, and J. H. Burge are preparing a manuscript to be called "Time scale dependent conformable tool."

1. Introduction

The demand for an efficient workpiece edge figuring process have been increased due to the popularity of segmented optics in many next generation optical systems, such as the Giant Magellan Telescope (GMT) [1] and James Webb Space Telescope (JWST) [2]. Because those systems have multiple mirror segments as their primary or secondary mirrors, i) the total length of edges is much larger than the conventional system with one mirror; ii) the edges are distributed across the whole pupil. Thus, a precise and efficient edge fabrication method is important to ensure the final performance of the optical system (e.g. light collecting power and spatial resolution based on the point spread function) and reasonable delivery time.

Many Computer Controlled Optical Surfacing (CCOS) techniques have been presented and developed since 1972 [3-10]. The CCOS with its superb ability to control material removal is known as an ideal method to fabricate state-of-the-art optical surfaces, such as meter-class optics, segmented mirrors, off-axis mirrors, and so forth [7-9, 11].

The dwell time map of a tool on the workpiece is usually the primary control parameter to achieve a target removal (i.e. form error on the workpiece) as it can be modulated via altering the transverse speed of the tool on the workpiece [3-10, 12]. In order to calculate an optimized dwell time map, the CCOS mainly relies on a de-convolution process of the target removal using a Tool Influence Function (TIF) (i.e. the material removal map for a given tool and workpiece motion). Thus, one of the most important elements for a successful CCOS is to obtain an accurate TIF.

The TIF can be calculated based on the equation of material removal, Δz, which is known as the Preston's equation [11],

$$\Delta z(x, y) = \kappa \cdot P(x, y) \cdot V_T(x, y) \cdot \Delta t(x, y) \tag{1}$$

where Δz is the integrated material removal from the workpiece surface, κ the Preston coefficient (i.e. removal rate), P pressure on the tool-workpiece contact position, V_T magnitude of relative speed between the tool and workpiece surface and Δt dwell time. It assumes that the integrated material removal, Δz, depends on P, V_T and Δt linearly.

It is well known that a nominal TIF calculated by integrating Eq. (1) under a moving tool fits well to experimental (i.e. measured) TIF as long as the tool stays inside the workpiece [11]. However, once the tool overhangs the edge of workpiece, the measured TIF tends to deviate from the nominal behavior due to dramatically varying pressure range, tool bending, and non-linear effects due to tool material (e.g. pitch) flow [15].

Assuming the linearity of Preston's equation the edge effects can be associated with the pressure distribution on the tool-workpiece contact area. R. A. Jones suggested a linear pressure distribution model in 1986 [8]. Luna-Aguilar, et al.(2003) and Cordero-Davila, et al.(2004) developed this approach further using a non-linear high pressure distribution near the edge-side of the workpiece, however they did not report the model's validity by demonstrating it using experimental evidence [13, 14]. These analytical pressure distributions were fed into the Preston's equation, Eq. (1), to calculate edge TIFs.

For any real polishing tool, the actual removal distribution is a complex function of many factors such as tool-workpiece configuration, tool stiffness, polishing compounds, polishing pad, and so forth. The analytical pressure distribution, *p(x,y)*, approaches [8, 13, 14] tend to ignore some of these effects. Also, in the edge TIF cases, the linearity for Preston's equation may need to be re-considered since the pressure distribution changes in wide pressure value range. The linearity is usually valid for a moderate range of pressure, P, values for a given polishing configuration [15].

#106335 - $15.00 USD Received 13 Jan 2009; revised 3 Mar 2009; accepted 20 Mar 2009; published 25 Mar 2009

Rather than assigning the edge effects to a certain type of analytical pressure distribution model, we define a parametric model based on measured data that allows us to create an accurate TIF without the need of identifying the actual cause of the abnormal behavior in edge removal. We then re-defined the Preston coefficient, κ, which has been regarded as a universal constant in the spatial domain as a function of position in the TIF via the parametric approach. By doing so, we can simulate the combined net effect of many complex factors without adding more terms to the original Preston's equation, Eq. (1).

This paper describes the parametric model and provides examples of its application. Section 2 deals with the theoretical background supporting the parametric edge TIF model. We introduce a functional form of the κ map, and show simulated parametric edge TIFs from the model in Section 3. The experimental demonstration and value of the parametric edge TIF model are summarized in Sections 4 and 5, respectively.

2. Theoretical background for the parametric edge TIF model

2.1 Linear pressure distribution model

Assuming the linear pressure distribution and Preston's relation, we determine the resulting TIF analytically. Assume local coordinate system, (x, y), centered at the workpiece edge with the x axis in the overhang direction (i.e. the radial direction from the workpiece center). The pressure distribution under the tool-workpiece contact area should satisfy two conditions [14]. i) The total force, f_0, applied on the tool should be the same as the integral of the pressure distribution, $p(x,y)$, over the tool-workpiece contact area, A. ii) The total sum of the moment on the tool should be zero. It is assumed that the pressure distribution in y direction is constant, and it is symmetric with respect to the x axis. The moment needs to be calculated about the center of mass of the tool, (x', y') [14]. These two conditions are expressed in Eqs. (2) and (3), respectively.

$$\iint_A p(x,y)dxdy = f_0 \tag{2}$$

$$\iint_A (x-x')\cdot p(x-x',y)dxdy = 0 \tag{3}$$

where x' is the x coordinate of the center of mass of the tool.

While we acknowledge the freedom of choosing virtually any form of mathematical function for the analytical expression of pressure distribution, R.A. Jones introduced the linear pressure distribution model, Eq. (4), in 1986 [8] on the tool-workpiece contact area without detailed study of many higher order factors such as tool bending.

$$p(x,y) = c_1 \cdot x + c_2 \tag{4}$$

The pressure distribution, $p(x,y)$, is determined by solving two equations, Eqs. (2) and (3), for two unknown coefficients, c_1 and c_2. Even though this analytical solution yields negative pressures for large overhang cases [14], we can replace it with zero pressure in practice and solve for c_1 and c_2 by iteration. Some examples of the linear pressure distribution, $p(x)$, are plotted in Fig. 1 (left) when a circular tool overhang ratio, S_{tool}, changes from 0 to 0.3. S_{tool} is defined as the ratio of the overhang distance, H, to the tool width in the overhang direction, W_{tool}, in Fig. 1 (left).

This linear pressure model was fed into the Preston's equation, Eq. (1), to generate the basic edge TIF in Section 3.1.

#106335 - $15.00 USD Received 13 Jan 2009; revised 3 Mar 2009; accepted 20 Mar 2009; published 25 Mar 2009

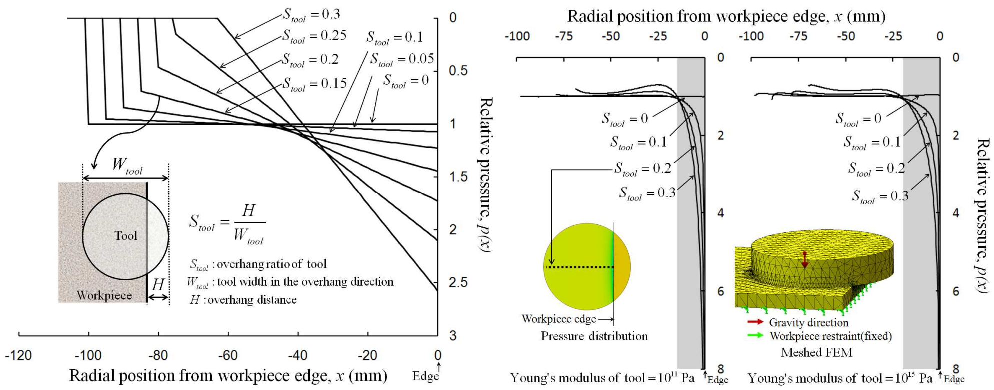

Fig. 1. x-profiles of the pressure distribution, $p(x,y)$, under the tool-workpiece contact area: linear pressure distribution model. (left), static FEA results. (right).

2.2 The first (edge-side) correction

One of the well-known edge removal anomalies is the 'turned-down edge', excessively high removal relative to the target removal near the edge-side [15]. This effect, as shown in the top-right quadrant of Fig. 7 later, cannot be explained by the linear pressure distribution model (i.e. basic edge TIF model). It may result from the non-linear high pressure distribution near the edge-side.

Static Finite Element Analysis (FEA) was performed to characterize a general trend of the edge pressure distribution when tools with different stiffnesses overhang a workpiece. A circular tool and a workpiece were created in a solid model as shown in Fig. 1 (right). For simplicity of the solid model, the effects of the polishing compound between the tool and workpiece were ignored in this study. The polishing compound was assumed as an ideal adhesive, so that the boundary condition at the tool-workpiece interface was set as a 'bonded' case. A next generation edge TIF model based on more comprehensive FEA, that considers the realistic effects of the polishing compound and detailed tool characteristics, will be reported [16]. The Young's modulus of the tool was changed to simulate the effects of the tool stiffness (e.g. 10^{15} Pa: extremely rigid tool and 0.7×10^{11} Pa: typical Aluminum). The tool was deformed by gravity, and the pressure distribution in the gravity direction was calculated under the tool-workpiece contact area.

Two of the FEA results are shown in Fig. 1 (right). There are two major trends in common for most of the FEA results. i) There is a non-linear high pressure distribution in the edge-side, shaded region in Fig. 1 (right). ii) The range of this non-linear distribution remains about same although the overhang ratio, S_{tool}, varies.

The first correction term, f_1, described in detail later in Section 3.2 is formed to correct this edge-side phenomenon.

2.3 The second (workpiece-center-side) correction

Experimentally it was found that the high pressure distribution model used on the edge-side of the tool did not predict the measured behavior at the other side (i.e. workpiece-center-side) of the tool. For an example, more removal than the predicted removal based on the basic edge TIF was observed in the workpiece-center-side of the experimental edge removal profile as shown in the top-right quadrant of Fig. 7. This phenomenon cannot be explained using models which focus only on the edge-side effects. Therefore, we define a second correction term, f_2, to address this discrepancy in Section 3.2. It allows us to increase or decrease the workpiece-center-side removal without considering many factors, such as tool bending effect, non-linearity of the Preston's equation, fluid dynamics of the polishing compound, etc.

#106335 - $15.00 USD Received 13 Jan 2009; revised 3 Mar 2009; accepted 20 Mar 2009; published 25 Mar 2009

3. Parametric edge TIF model

3.1 Generation of the basic edge TIF

For a given tool motion and pressure distribution under the tool-workpiece contact area, a TIF can be calculated using Eq. (1) [11]. The basic edge TIF uses the linear pressure model. Two types of tool motion, orbital and spin, were used in this paper. i) Orbital: The tool orbits around the TIF center with orbital radius, $R_{orbital}$, and does not rotate. ii) Spin: The tool rotates about the center of the tool. These tool motions are depicted in Fig. 2.

The tool overhang ratio, S_{tool}, is fixed for the spin tool motion case, but varies as a function of tool position (A~F in Fig. 2 (left)) for the orbital case while the basic edge TIF calculation is being made.

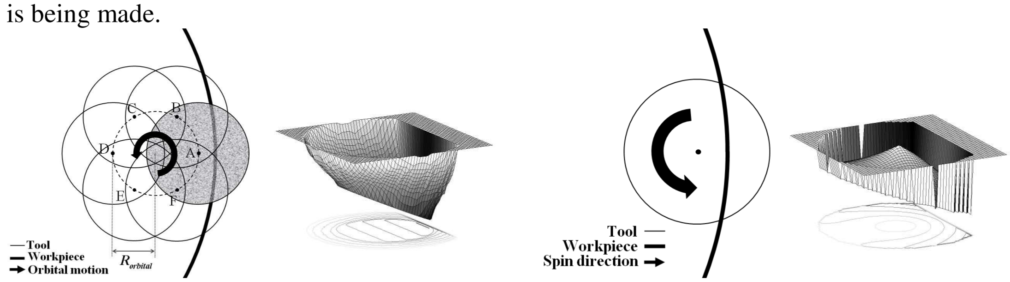

Fig. 2. Orbital (left) and spin (right) tool motion with the basic edge TIF.

3.2 Spatially varying Preston coefficient (κ) map

A new concept using the κ map for the parametric edge TIF model is introduced. The κ map represents the spatial distribution of the Preston coefficient, $\kappa(x,y)$, on the basic edge TIF that already includes the linear pressure gradient. It changes as a function of TIF overhang ratio, S_{TIF}, and five function control parameters (α, β, γ, δ and ε). S_{TIF} is defined as the ratio of the overhang distance, H, to the TIF width in the overhang direction, W_{TIF}, in Fig. 3. The parametric edge TIF can be calculated by multiplying the basic edge TIF by the κ map.

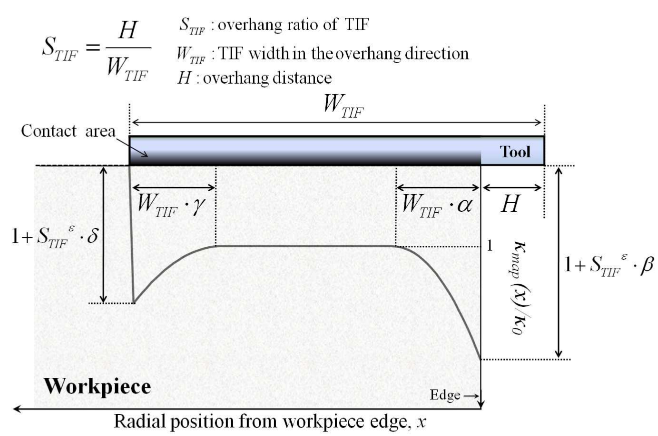

Fig. 3. Degrees of freedom of the κ map (in x-profile) using five parameters.

The TIF width may not be equal to the tool width since it includes the tool motion. For instance, the TIF width is equal to the tool width for the spin motion case. However, for the orbital motion case, the TIF width becomes the sum of the tool width and orbital motion diameter (i.e. $2 \cdot R_{orbital}$).

The virtue of this parametric κ map approach is that it does not require independent understanding of each and every factor affecting the material removal process. Instead, only the combined net effect of them is represented by the κ map. The κ map is defined by a local

#106335 - $15.00 USD Received 13 Jan 2009; revised 3 Mar 2009; accepted 20 Mar 2009; published 25 Mar 2009

coordinate centered at the edge of the workpiece. x represents the radial position from the workpiece edge.

The edge-side high removal, based on the non-linear high pressure distributions near the workpiece edge (mentioned earlier in Section 2.2), is approximated by the first quadratic correction term, f_1, with two parameters, α and β. The first parameter, α, determines the range of the quadratic correction from the edge of the workpiece. The second parameter, β, controls the magnitude of the correction. This degree of freedom using α and β is shown in Fig. 3. This correction is shown graphically in Fig. 3 and defined analytically as

$$f_1(x,\alpha,\beta) = \frac{\beta}{(W_{TIF}\cdot\alpha)^2}\cdot(x+W_{TIF}\cdot\alpha)^2\cdot\Theta(x+W_{TIF}\cdot\alpha) \tag{5}$$

where $\Theta(z)$ is the step function; 1 for $z\geq 0$ and 0 for $z<0$.

The second correction term, f_2, to address the discrepancy between the simulated (i.e. predicted) edge removal using basic edge TIF and measured edge removal in the workpiece-center-side region (mentioned in Section 2.3) is defined by Eq. (6). Similar to f_1, it has two parameters, γ and δ. The third parameter, γ, determines the range of the second correction, and the fourth parameter, δ, controls the magnitude of the correction as shown in Fig. 3.

$$f_2(x,\gamma,\delta) = \frac{\delta}{(W_{TIF}\cdot\gamma)^2}\cdot(-x-W_{TIF}+W_{TIF}\cdot S_{TIF}+W_{TIF}\cdot\gamma)^2\cdot\Theta(-x-W_{TIF}+W_{TIF}\cdot S_{TIF}+W_{TIF}\cdot\gamma) \tag{6}$$

The κ map is defined in Eq. (7). It is a sum of the first and second correction terms, and includes a fifth parameter, ε. The fifth parameter, ε, was introduced to change the magnitude of the κ map as a function of TIF overhang ratio, S_{TIF}. Larger ε means that required correction magnitude increases faster as overhang ratio increases.

$$\kappa_{map}(x,\alpha,\beta,\gamma,\delta,\varepsilon) = \kappa_0\cdot\{1+S_{TIF}{}^{\varepsilon}\cdot(f_1+f_2)\} \tag{7}$$

where the κ_0 is the Preston coefficient when there is no overhang.

The x-profiles of example κ maps are plotted in Fig. 4. An arbitrary parameter set (α=0.2, β=2, γ=0.2, δ=1 and ε=0.2) was used in the example.

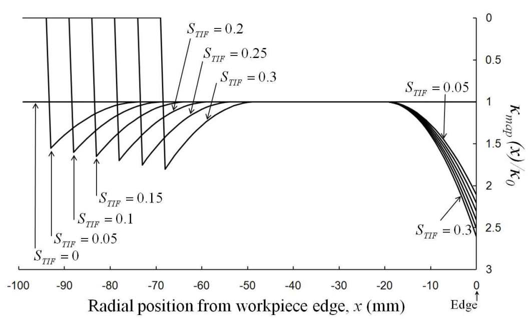

Fig. 4. x-Profiles of κ maps for various overhang ratio, S_{TIF}. (α=0.2, β=2, γ=0.2, δ=1 and ε=0.2).

3.3 Generation of the parametric edge TIF

The parametric edge TIFs for orbital and spin tool motion cases were generated by multiplying the κ map (i.e. the spatial distribution of the Preston's coefficient) by the basic edge TIF (with κ =1) introduced in Section 3.1. The overhang ratio, S_{TIF}, was varied from 0 to 0.3. Five parameter values (α, β, γ, δ, and ε) were used to fit the experimental data in Section 4.1 and 4.2. The parametric edge TIFs are shown in Table 1. As we increase the overhang ratio, S_{TIF}, non-linearly increasing removal near the workpiece edge is clearly shown as a result of the first correctional term for both the orbital and spin cases. The effects of the

#106335 - $15.00 USD Received 13 Jan 2009; revised 3 Mar 2009; accepted 20 Mar 2009; published 25 Mar 2009

second correction are also observed. Due to the opposite signs of δ for the orbital (δ = 20) and spin (δ = -3) cases, in the workpiece-center-side region, there is more and less removal than the basic edge TIF's.

Table 1. Normalized parametric edge TIFs[a]

Tool motion	Overhang ratio, S_{TIF} 0	0.1	0.2	0.3	Scale
Orbital (Media 1)	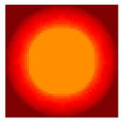	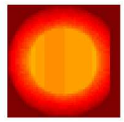	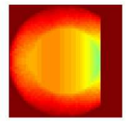	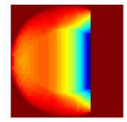	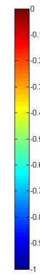
Spin (Media 2)	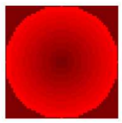	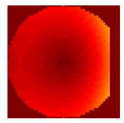	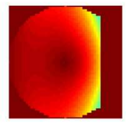	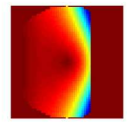	

[a](Orbital: α=0.2, β=4, γ=0.4, δ=20, ε=1.5 / Spin: α=0.4, β=6, γ=0.3, δ=-3, ε=0.9)

4. Experimental demonstration of the parametric edge TIF model

Two sets of experiments were used to demonstrate the performance of the parametric edge TIF model. Because the workpiece was rotated in the experiments, integration of parametric edge TIF along the workpiece rotation direction was computed to get the integrated removal profile while considering the workpiece rotation velocity. These model based removal profiles are plotted in Figs. 5 and 6. The conditions for the two edge TIF experiments are provided in Table 2.

Table 2. Edge TIF experiment conditions

Experiment Set No.		1	2
General	Run time	6 hours	1 hour
	Polishing compound	Hastlite ZD	Rhodite
Workpiece	Diameter	660mm	250mm
	Material	ULE	Pyrex
	Surface figure	Convex	Concave
	RPM	6	24
Tool [b]	Polishing Material	Poly-Urethane pad	Poly-Urethane pad
	Diameter	172mm	100mm
	RPM	60 (orbital motion)	30 (spin motion)
	Tool motion	Orbital	Spin
	Orbital radius, $R_{orbital}$	20mm	N/A

[b]More detailed information about the tool will be reported [17].

4.1 Experimental set 1: Orbital tool motion

The first experimental set was performed using orbital tool motion on a ULE workpiece. The overhang ratio was changed for S_{TIF} = 0.05, 0.14, 0.24 and 0.28. The measured removal profiles with RMS error bars are plotted in Fig. 5. The simulated removal profiles based on

#106335 - $15.00 USD Received 13 Jan 2009; revised 3 Mar 2009; accepted 20 Mar 2009; published 25 Mar 2009

the parametric edge TIF model (α=0.2, β=4, γ=0.4, δ=20 and ε=1.5) are also plotted. The five parameters were optimized to fit the experimental data. With one set of parameters, most of the simulated removal profiles for all overhang ratio cases are well fit to the measured removals within the RMS error bars. It means that we can predict all series of removal profiles with any overhang ratio for a given tool and tool motion as long as we perform a few edge runs to determine the tool's characteristic parameter set initially.

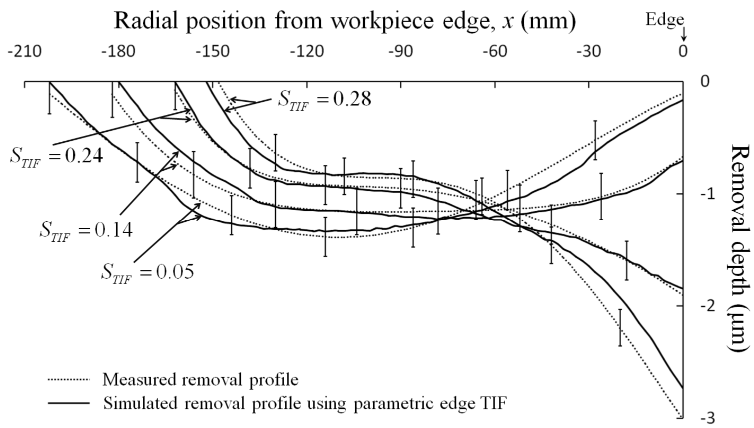

Fig. 5. Measured vs simulated removal profiles: orbital tool motion (α=0.2, β=4, γ=0.4, δ=20, and ε=1.5).

4.2 Experimental set 2: Spin tool motion

The second experimental set was performed using spin tool motion on a Pyrex workpiece.

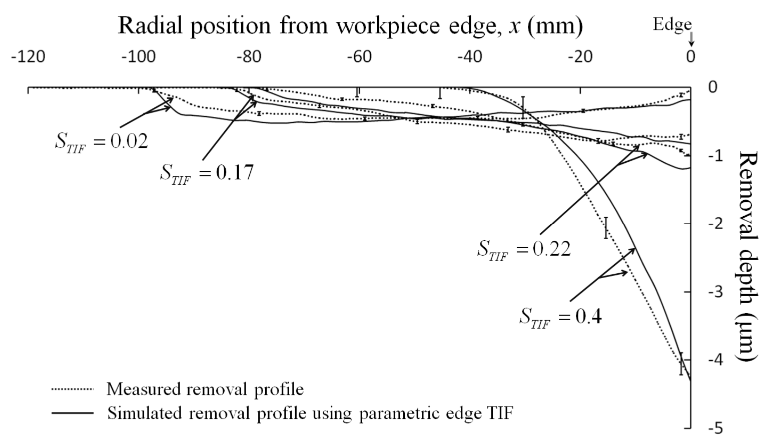

Fig. 6. Measured vs simulated removal profiles: spin tool motion case (α=0.4, β=6 γ=0.3, δ=-3, and ε=0.9).

The overhang ratio, S_{TIF}, was changed to 0.02, 0.17, 0.22 and 0.4. The measured removal profiles with RMS error bars are plotted in Fig. 6. The simulated removal profiles based on the parametric edge TIF model are plotted also. They are reasonably well matched with the measured removal profiles for all overhang ratio cases including very high overhang ratio case, S_{TIF} = 0.4.

#106335 - $15.00 USD Received 13 Jan 2009; revised 3 Mar 2009; accepted 20 Mar 2009; published 25 Mar 2009

4.3 Performance of the parametric edge TIF model

The comparison between the four different edge TIF models is shown in Fig. 7. The simulated removal profile based on nominal (i.e. no edge model) TIF model does not follow the overall slope of the measured removal profile. Especially, it shows a large difference in the edge-side removal (x = 0 ~ -60mm). The computed removal profile using basic edge TIF model seems to have a closer overall slope to the measured removal. However, two mismatches between the measured and simulated removal are clearly observed in the edge-side and workpiece-center-side regions. The parametric edge TIF model using only the first correction allows us to correct the discrepancy in the edge-side removal. The removal profile based on the parametric edge TIF model using both the first and second correction is well matched with the experimental removal profile over the whole range of the removal profile.

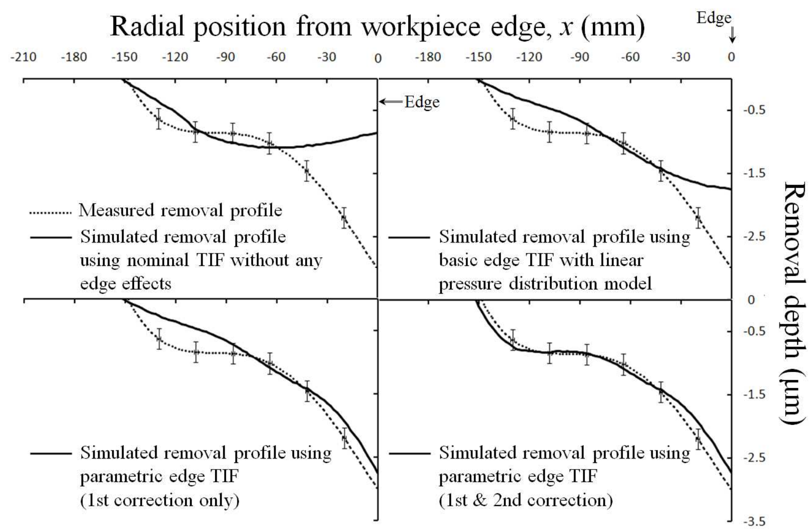

Fig. 7. Measured (with RMS error bars) vs simulated (using different edge TIF models) edge removal profiles for the orbital tool motion case.

The comparison between the four TIF models is presented in Fig. 8. We define normalized fit residual, Δ, as a figure of merit to quantify the performance of the parametric model compared to the data. This is normalized as

$$\Delta = normalized\ fit\ residual = \frac{RMS\ of\ (data - model)}{RMS\ of\ data} \cdot 100\ (\%) \tag{8}$$

It is clear that the normalized fit residual, Δ, is relatively low (about 10~20%) for all TIF model cases when the overhang ratio is small (S_{TIF} <0.14 for orbital case and S_{TIF} <0.02 for spin case). It basically means that there is no difference between nominal and edge TIF models when the overhang effects are negligible.

The improvements become significant as the overhang ratio increases. For the orbital tool motion case with S_{TIF} =0.28, the normalized fit residual, Δ, falls to 10% (parametric edge TIF using both corrections) from 52% (nominal TIF), or from 30% (basic edge TIF). For the spin tool motion case with S_{TIF} =0.4, the normalized fit residual, Δ, is dramatically improved to 12% (parametric edge TIF using both corrections) from 87% (nominal TIF), or from 66% (basic edge TIF). The second correction is not really required for the spin tool motion case, in contrast to the orbital tool motion case, where the second correction brought significant improvement.

#106335 - $15.00 USD Received 13 Jan 2009; revised 3 Mar 2009; accepted 20 Mar 2009; published 25 Mar 2009

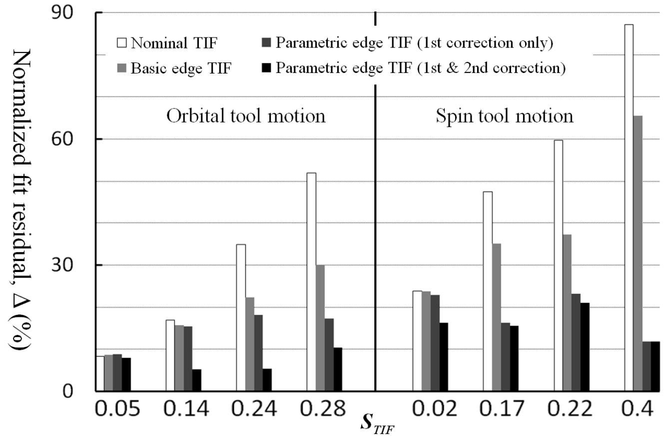

Fig. 8. Normalized fit residual, Δ, of the simulated removal profiles using different TIF models for orbital and spin tool motion cases.

5. Concluding remarks

We presented a parametric edge TIF model that allows accurate simulation of edge effects when a tool overhangs the workpiece edge. Unlike other approaches using analytical pressure distributions to develop edge TIF models, we introduced a parametric approach using a κ map, which represents the spatial distribution of the Preston coefficient. In this way, we were able to express the net effects of many entangled factors affecting the edge removal process in terms of a parametric κ map. Then the parametric edge TIF was derived from a multiplication of the κ map and the basic edge TIF.

Experimental verification for the parametric edge TIF model was successfully performed. The normalized fit residual, Δ, for the simulated removal using the parametric edge TIF model stayed in the 5~20% range for all overhang cases, which allows us to correct about 80% of the surface errors (with an assumption that everything else is ideal) in a single CCOS process. It means that more than 99% of the initial surface errors can be corrected in 3 CCOS runs. Improvement in convergence rate for the residual surface form error is directly related to more efficient time management and lower cost for large optics fabrication projects. Its significance would be even greater for segmented optical system projects, such as GMT [1] and JWST [2], which have more edges across the whole pupil.

Acknowledgments

We acknowledge that this work was supported by the Optical Engineering and Fabrication Facility of the College of Optical Sciences at the University of Arizona, and Korea Research Foundation Grant funded by Korean Government (MOEHRD) KRF-2007-612-C00045. We thank Buddy Martin (Steward Observatory Mirror Lab) and Robert Parks (College of Optical Sciences) at the Univ. of Arizona for assistance in the final manuscript preparation.

#106335 - $15.00 USD Received 13 Jan 2009; revised 3 Mar 2009; accepted 20 Mar 2009; published 25 Mar 2009

APPENDIX E

Edge Tool Influence Function Library using the Parametric Edge Model for Computer Controlled Optical Surfacing

Dae Wook Kim, Won Hyun Park, Sug-Whan Kim

and James H. Burge

Article published in **SPIE *Proceedings***

2009

Copyright Transfer Agreement

Publisher's permission is hereby granted under the following conditions: (1) the material to be used has appeared in our publication without credit or acknowledgment to another source; and (2) you credit the original SPIE publication. Include the authors' names, title of paper, volume title, SPIE volume number, and year of publication in your credit statement.

Eric Pepper October 28, 2009
Eric Pepper Date
Director of Publications, SPIE

Edge tool influence function library using the parametric edge model for computer controlled optical surfacing

Dae Wook Kim*[a], Won Hyun Park[a], Sug-Whan Kim[b], and James H. Burge [a]
[a] College of Optical Sciences, Univ. of Arizona, 1630 E. University Blvd, Tucson, AZ 85721, USA;
[b] Space Optics Laboratory, Dept. of Astronomy, Yonsei Univ., 134 Sinchon-dong, Seodaemun-gu, Seoul 120-749, Republic of Korea

ABSTRACT

Computer controlled optical surfacing (CCOS) requires accurate knowledge of the tool influence function (TIF) for the polishing tool. The linear Preston's model for material removal has been used to determine the TIF for most cases. As the tool runs over the edge of the workpiece, however, nonlinear removal behavior needs to be considered to model the edge TIF. We reported a new parametric edge TIF model in a previous paper.** This model fits 5 parameters to measured data to accurately predict the edge TIF. We present material from the previous paper, and provide a library of the parametric edge TIFs for various tool shape and motion cases. The edge TIF library is a useful reference to design an edge figuring process using a CCOS technique.

Keywords: edge tool influence function, edge removal, Preston's model, edge TIF library

1. INTRODUCTION

Many Computer Controlled Optical Surfacing (CCOS) techniques have been presented and developed since 1972 [1-8]. The CCOS with its superb ability to control material removal is known as an ideal method to fabricate state-of-the-art optical surfaces, such as meter-class optics, segmented mirrors, off-axis mirrors, and so forth [5-7, 9].

The demand for an efficient workpiece edge figuring process using the CCOS techniques have been increased due to the popularity of segmented optics in many next generation optical systems, such as the Giant Magellan Telescope (GMT) [10] and James Webb Space Telescope (JWST) [11]. Since those systems have multiple mirror segments as their primary or secondary mirrors, i) the total length of edges is much larger than the conventional system with one mirror; ii) the edges are distributed across the whole pupil.

The dwell time map of a tool on the workpiece is usually the primary control parameter to achieve a target removal (i.e. form error on the workpiece) as it can be modulated via altering the transverse speed of the tool on the workpiece [1-8, 12]. In order to calculate an optimized dwell time map, the CCOS mainly relies on a de-convolution process of the target removal using a Tool Influence Function (TIF) (i.e. the material removal map for a given tool and workpiece motion). Thus, having an edge TIF library (i.e. collection of the edge TIFs) based on a realistic edge model is crucial for the edge figuring process using the CCOS techniques.

The TIF can be calculated based on the equation of material removal, Δz, which is known as the Preston's equation [9],

$$\Delta z(x, y) = \kappa \cdot P(x, y) \cdot V_T(x, y) \cdot \Delta t(x, y) \tag{1}$$

* letter2dwk@hotmail.com; phone: 1 520 626 0486

** Section 1 ~ 4 is mainly from the previous paper without change [16].

where Δz is the integrated material removal from the workpiece surface, κ the Preston coefficient (i.e. removal rate), P pressure on the tool-workpiece contact position, V_T magnitude of relative speed between the tool and workpiece surface and Δt dwell time. It assumes that the integrated material removal, Δz, depends on P, V_T and Δt linearly.

It is well known that a nominal TIF calculated by integrating Eq. (1) under a moving tool fits well to experimental (i.e. measured) TIF as long as the tool stays inside the workpiece [9]. However, once the tool overhangs the edge of workpiece, the measured TIF tends to deviate from the nominal behavior due to dramatically varying pressure range, tool bending, and non-linear effects due to tool material (e.g. pitch) flow [13].

Assuming the linearity of Preston's equation the edge effects can be associated with the pressure distribution on the tool-workpiece contact area. R. A. Jones suggested a linear pressure distribution model in 1986 [6]. Luna-Aguilar, et al.(2003) and Cordero-Davila, et al.(2004) developed this approach further using a non-linear high pressure distribution near the edge-side of the workpiece, however they did not report the model's validity by demonstrating it using experimental evidence [14, 15].

For any real polishing tool, the actual removal distribution is a complex function of many factors such as tool-workpiece configuration, tool stiffness, polishing compounds, polishing pad, and so forth. The analytical pressure distribution, $p(x,y)$, approaches [6, 14, 15] tend to ignore some of these effects. Also, in the edge TIF cases, the linearity for Preston's equation may need to be re-considered since the pressure distribution changes in wide pressure value range. The linearity is usually valid for a moderate range of pressure, P, values for a given polishing configuration [13].

Rather than assigning the edge effects to a certain type of analytical pressure distribution model, we define a parametric model based on measured data that allows us to create an accurate TIF without the need of identifying the actual cause of the abnormal behavior in edge removal. We then re-defined the Preston coefficient, κ, which has been regarded as a universal constant in the spatial domain as a function of position in the TIF via the parametric approach. By doing so, we can simulate the combined net effect of many complex factors without adding more terms to the original Preston's equation, Eq. (1).

This paper describes the parametric edge TIF model and provides an edge TIF library for various CCOS parameters, such as tool shape, size and motion. Section 2 deals with the theoretical background supporting the parametric edge TIF model. We introduce a functional form of the κ map, and show simulated parametric edge TIFs from the model in Section 3. The experimental demonstration and value of the parametric edge TIF model are summarized in Sections 4. The edge TIF library using the parametric edge model will be provided in Section 5 and Appendix A.

2. THEORETICAL BACKGROUND FOR THE PARAMETRIC EDGE TIF MODEL

2.1 Linear pressure distribution model

Assuming the linear pressure distribution and Preston's relation, we determine the resulting TIF analytically. Assume local coordinate system, (x, y), centered at the workpiece edge with the x axis in the overhang direction (i.e. the radial direction from the workpiece center). The pressure distribution under the tool-workpiece contact area should satisfy two conditions [15]. i) The total force, f_0, applied on the tool should be the same as the integral of the pressure distribution, $p(x,y)$, over the tool-workpiece contact area, A. ii) The total sum of the moment on the tool should be zero. It is assumed that the pressure distribution in y direction is constant, and it is symmetric with respect to the x axis. The moment needs to be calculated about the center of mass of the tool, (x', y') [15]. These two conditions are expressed in Eq. (2) and (3), respectively.

$$\iint_A p(x,y)dxdy = f_0 \tag{2}$$

$$\iint_A (x-x')\cdot p(x-x',y)dxdy = 0 \tag{3}$$

where x' is the x coordinate of the center of mass of the tool.

R.A. Jones introduced the linear pressure distribution model, Eq. (4), in 1986 [6] on the tool-workpiece contact area.

$$p(x,y) = c_1 \cdot x + c_2 \tag{4}$$

The pressure distribution, $p(x,y)$, is determined by solving two equations, Eq. (2) and (3), for two unknown coefficients, c_1 and c_2. Some examples of the linear pressure distribution, $p(x)$, are plotted in Fig. 1 (left) when a circular tool overhang ratio, S_{tool}, changes from 0 to 0.3. S_{tool} is defined as the ratio of the overhang distance, H, to the tool width in the overhang direction, W_{tool}, in Fig. 1 (left).

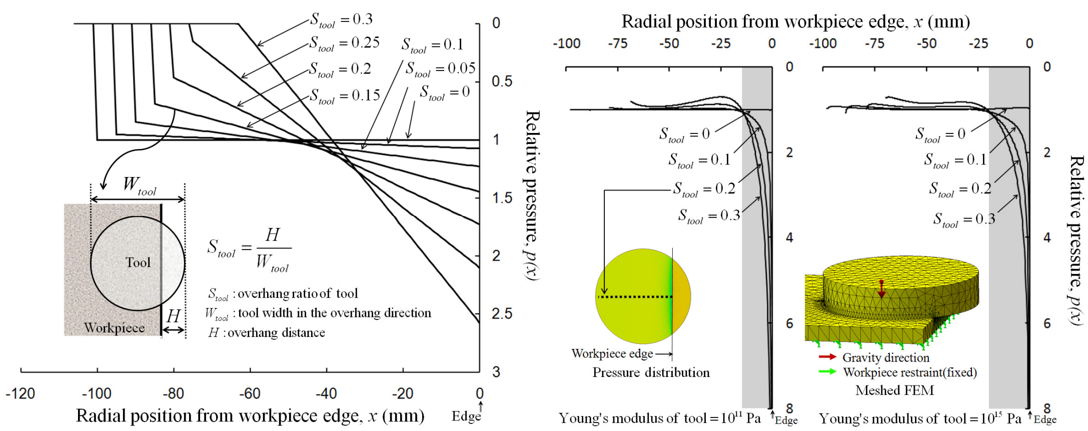

Fig. 1. x-profiles of the pressure distribution, $p(x,y)$, under the tool-workpiece contact area: linear pressure distribution model. (left), static FEA results. (right)

2.2 The first (edge-side) correction Section

One of the well-known edge removal anomalies is the 'turned-down edge', excessively high removal relative to the target removal near the edge-side [13]. This effect, as shown in the top-right quadrant of Fig. 7 later, cannot be explained by the linear pressure distribution model (i.e. basic edge TIF model).

Static Finite Element Analysis (FEA) was performed to characterize a general trend of the edge pressure distribution when tools with different stiffnesses overhang a workpiece. A circular tool and a workpiece were created in a solid model as shown in Fig. 1 (right). The Young's modulus of the tool was changed to simulate the effects of the tool stiffness. The tool was deformed by gravity, and the pressure distribution in the gravity direction was calculated under the tool-workpiece contact area.

Two of the FEA results are shown in Fig. 1 (right). There are two major trends in common for most of the FEA results. i) There is a non-linear high pressure distribution in the edge-side, shaded region in Fig. 1 (right). ii) The range of this non-linear distribution remains about same although the overhang ratio, S_{tool}, varies.

The first correction term, f_1, described in detail later in Section 3.2 is formed to correct this edge-side phenomenon.

2.3 The second (workpiece-center-side) correction

Experimentally it was found that the high pressure distribution model used on the edge-side of the tool did not predict the measured behavior at the other side (i.e. workpiece-center-side) of the tool. For an example, more removal than the predicted removal based on the basic edge TIF was observed in the workpiece-center-side of the experimental edge removal profile as shown in the top-right quadrant of Fig. 7. This phenomenon cannot be explained using models which focus only on the edge-side effects. Therefore, we define a second correction term, f_2, to address this discrepancy in Section 3.2.

3. PARAMETRIC EDGE TIF MODEL

3.1 Generation of the basic edge TIF

For a given tool motion and pressure distribution under the tool-workpiece contact area, a basic edge TIF can be calculated using Eq. (1) and the linear pressure model in Section 2.1 [9]. Two types of tool motion, orbital and spin, were used in this paper. i) Orbital: The tool orbits around the TIF center with orbital radius, $R_{orbital}$, and does not rotate. ii) Spin: The tool rotates about the center of the tool. These tool motions are depicted in Fig. 2.

The tool overhang ratio, S_{tool}, is fixed for the spin tool motion case, but varies as a function of tool position (A~F in Fig. 2 (left)) for the orbital case while the basic edge TIF calculation is being made.

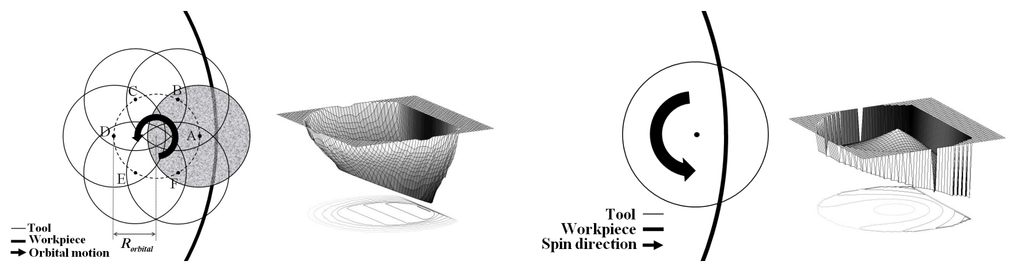

Fig. 2. Orbital (left) and spin (right) tool motion with the basic edge TIF.

3.2 Spatially varying Preston coefficient (κ) map

A new concept using the κ map for the parametric edge TIF model is introduced. The κ map represents the spatial distribution of the Preston coefficient, $\kappa(x,y)$, on the basic edge TIF that already includes the linear pressure gradient. It changes as a function of TIF overhang ratio, S_{TIF}, and five function control parameters (α, β, γ, δ and ε). S_{TIF} is defined as the ratio of the overhang distance, H, to the TIF width in the overhang direction, W_{TIF}, in Fig. 3. The parametric edge TIF can be calculated by multiplying the basic edge TIF by the κ map. The κ map is defined by a local coordinate centered at the edge of the workpiece. x represents the radial position from the workpiece edge.

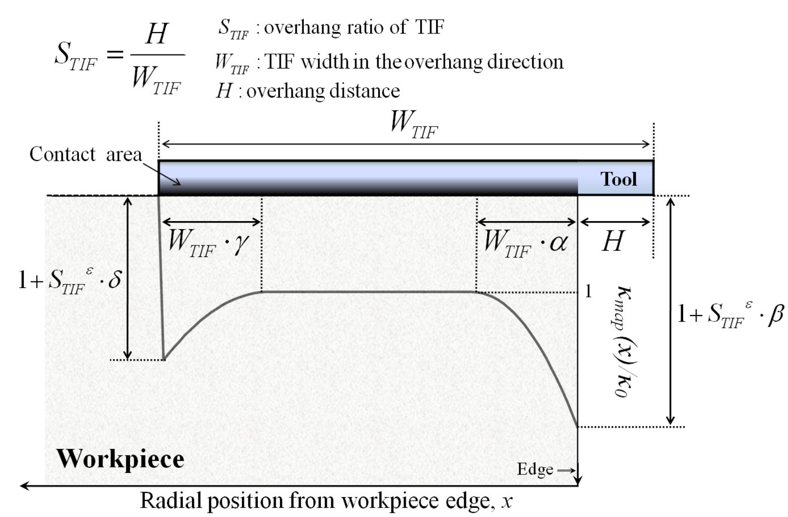

Fig. 3. Degrees of freedom of the κ map (in x-profile) using five parameters.

The edge-side high removal mentioned earlier in Section 2.2 is approximated by the first quadratic correction term, f_1, with two parameters, α and β. The first parameter, α, determines the range of the quadratic correction from the edge of the workpiece. The second parameter, β, controls the magnitude of the correction. This degree of freedom using α and β is shown in Fig. 3. This correction is shown graphically in Fig. 3 and defined analytically as

$$f_1(x,\alpha,\beta) = \frac{\beta}{(W_{TIF} \cdot \alpha)^2} \cdot (x + W_{TIF} \cdot \alpha)^2 \cdot \Theta(x + W_{TIF} \cdot \alpha) \tag{5}$$

where $\Theta(z)$ is the step function; 1 for $z \geq 0$ and 0 for $z<0$.

The second correction term, f_2, to address the discrepancy between the simulated edge removal using basic edge TIF and measured edge removal in the workpiece-center-side region (mentioned in Section 2.3) is defined by Eq. (6). Similar to f_1, it has two parameters, γ and δ. The third parameter, γ, determines the range of the second correction, and the fourth parameter, δ, controls the magnitude of the correction as shown in Fig. 3.

$$f_2(x,\gamma,\delta) = \frac{\delta}{(W_{TIF} \cdot \gamma)^2} \cdot (-x - W_{TIF} + W_{TIF} \cdot S_{TIF} + W_{TIF} \cdot \gamma)^2 \cdot \Theta(-x - W_{TIF} + W_{TIF} \cdot S_{TIF} + W_{TIF} \cdot \gamma) \tag{6}$$

The κ map is defined in Eq. (7). It is a sum of the first and second correction terms, and includes a fifth parameter, ε. The fifth parameter, ε, was introduced to change the magnitude of the κ map as a function of TIF overhang ratio, S_{TIF}. Larger ε means that required correction magnitude increases faster as overhang ratio increases.

$$\kappa_{map}(x,\alpha,\beta,\gamma,\delta,\varepsilon) = \kappa_0 \cdot \{1 + S_{TIF}{}^{\varepsilon} \cdot (f_1 + f_2)\} \tag{7}$$

where the κ_0 is the Preston coefficient when there is no overhang.

The x-profiles of example κ maps are plotted in Fig. 4. An arbitrary parameter set (α=0.2, β=2, γ=0.2, δ=1 and ε=0.2) was used in the example.

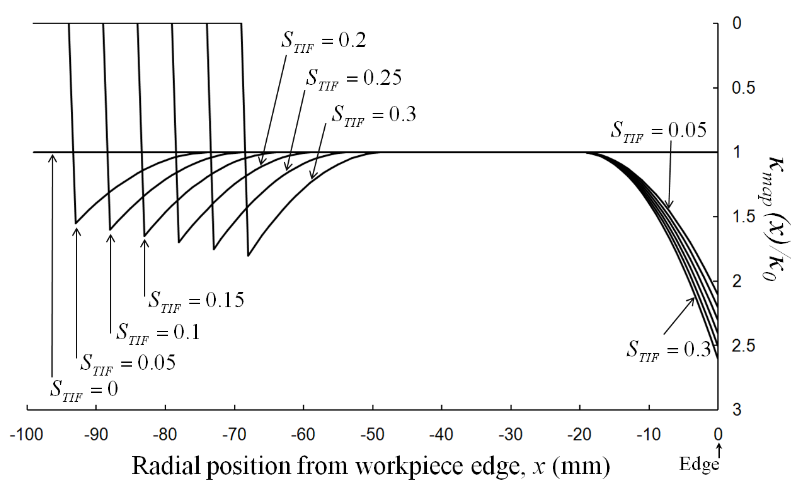

Fig. 4. x-Profiles of κ maps for various overhang ratio, S_{TIF}. (α=0.2, β=2, γ=0.2, δ=1 and ε=0.2).

3.3 Generation of the parametric edge TIF

The parametric edge TIFs for orbital and spin tool motion cases were generated by multiplying the κ map (i.e. the spatial distribution of the Preston's coefficient) by the basic edge TIF (with κ =1) introduced in Section 3.1. The overhang ratio, S_{TIF}, was varied from 0 to 0.3. Five parameter values (α, β, γ, δ, and ε) were used to fit the experimental data in Section 4.1 and 4.2. The parametric edge TIFs are shown in Table 1. As we increase the overhang ratio, S_{TIF}, non-linearly increasing removal near the workpiece edge is clearly shown as a result of the first correctional term for both the orbital and spin cases. The effects of the second correction are also observed. Due to the opposite signs of δ for the orbital (δ = 20) and spin (δ = -3) cases, in the workpiece-center-side region, there is more and less removal than the basic edge TIF's.

Table. 1. Normalized parametric edge TIFs

Tool motion	Overhang ratio, S_{TIF}				Scale
	0	0.1	0.2	0.3	
Orbital	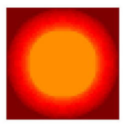	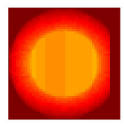	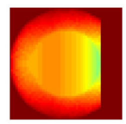	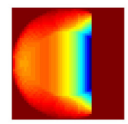	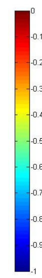
Spin	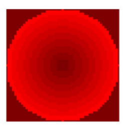	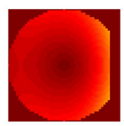	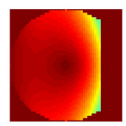	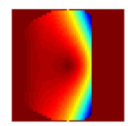	

(Orbital: α=0.2, β=4, γ=0.4, δ=20, ε=1.5 / Spin: α=0.4, β=6, γ=0.3, δ=-3, ε=0.9)

4. EXPERIMENTAL DEMONSTRATION OF THE PARAMETRIC EDGE TIF MODEL

Two sets of experiments were used to demonstrate the performance of the parametric edge TIF model. Because the workpiece was rotated in the experiments, integration of parametric edge TIF along the workpiece rotation direction was computed to get the integrated removal profile while considering the workpiece rotation velocity. These model based removal profiles are plotted in Fig. 5 and 6. The conditions for the two edge TIF experiments are provided in Table 2.

Table. 2. Edge TIF experiment conditions

Experiment Set No.		1	2
General	Run time	6 hours	1 hour
	Polishing compound	Hastlite ZD	Rhodite
Workpiece	Diameter	660mm	250mm
	Material	ULE	Pyrex
	Surface figure	Convex	Concave
	RPM	6	24
Tool	Polishing Material	Poly-Urethane pad	Poly-Urethane pad
	Diameter	172mm	100mm
	RPM	60 (orbital motion)	30 (spin motion)
	Tool motion	Orbital	Spin
	Orbital radius, $R_{orbital}$	20mm	N/A

4.1 Experimental set 1: Orbital tool motion

The first experimental set was performed using orbital tool motion on a ULE workpiece (w/ overhang ratio S_{TIF} = 0.05, 0.14, 0.24 and 0.28). The measured removal profiles with RMS error bars are plotted in Fig. 5. The simulated removal profiles based on the parametric edge TIF model (α=0.2, β=4, γ=0.4, δ=20 and ε=1.5) are also plotted. The five parameters were optimized to fit the experimental data. With one set of parameters, most of the simulated removal profiles for all overhang ratio cases are well fit to the measured removals within the RMS error bars.

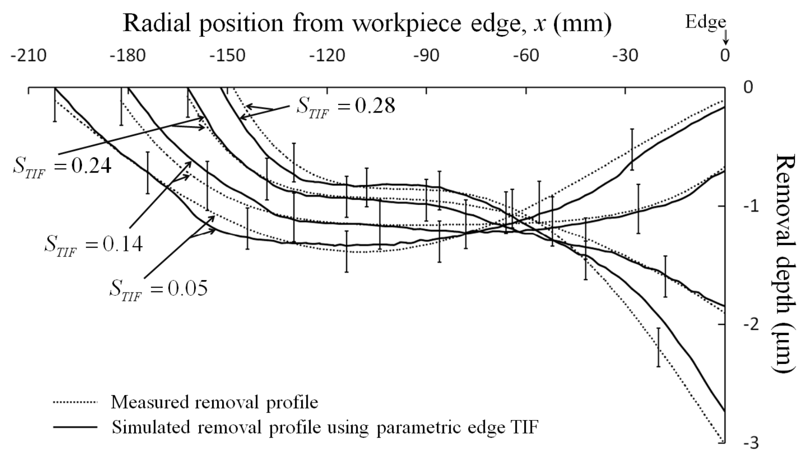

Fig. 5. Measured vs simulated removal profiles: orbital tool motion (α=0.2, β=4, γ=0.4, δ=20, and ε=1.5).

4.2 Experimental set 2: Spin tool motion

The second experimental set was performed using spin tool motion on a Pyrex workpiece. The overhang ratio, S_{TIF}, was changed to 0.02, 0.17, 0.22 and 0.4. The measured removal profiles with RMS error bars are plotted in Fig. 6. The simulated removal profiles based on the parametric edge TIF model are plotted also. They are reasonably well matched with the measured removal profiles for all overhang ratio cases including very high overhang ratio case, S_{TIF} = 0.4.

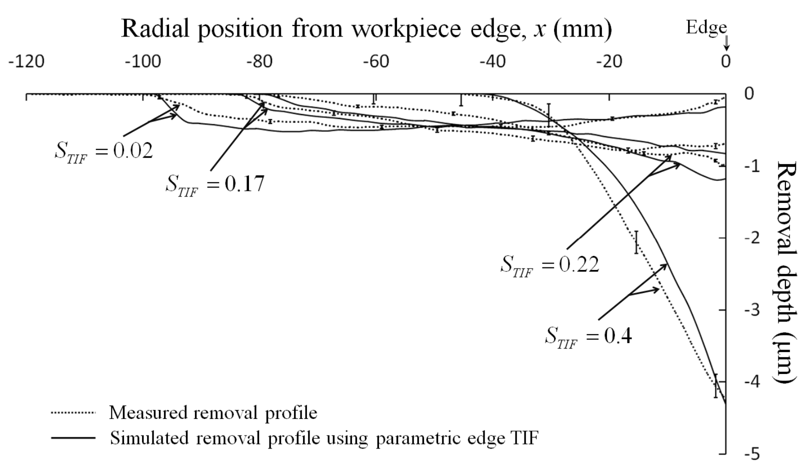

Fig. 6. Measured vs simulated removal profiles: spin tool motion case (α=0.4, β=6, γ=0.3, δ=-3, and ε=0.9).

4.3 Performance of the parametric edge TIF model

The comparison between the four different edge TIF models is shown in Fig. 7. The simulated removal profile based on nominal (i.e. no edge model) TIF model does not follow the overall slope of the measured removal profile. Especially, it shows a large difference in the edge-side removal (x = 0 ~ -60mm). The computed removal profile using basic edge TIF model seems to have a closer overall slope to the measured removal. However, two mismatches between the measured and simulated removal are clearly observed in the edge-side and workpiece-center-side regions. The parametric edge TIF model using only the first correction allows us to correct the discrepancy in the edge-side removal. The removal profile based on the parametric edge TIF model using both the first and second correction is well matched with the experimental removal profile over the whole range of the removal profile.

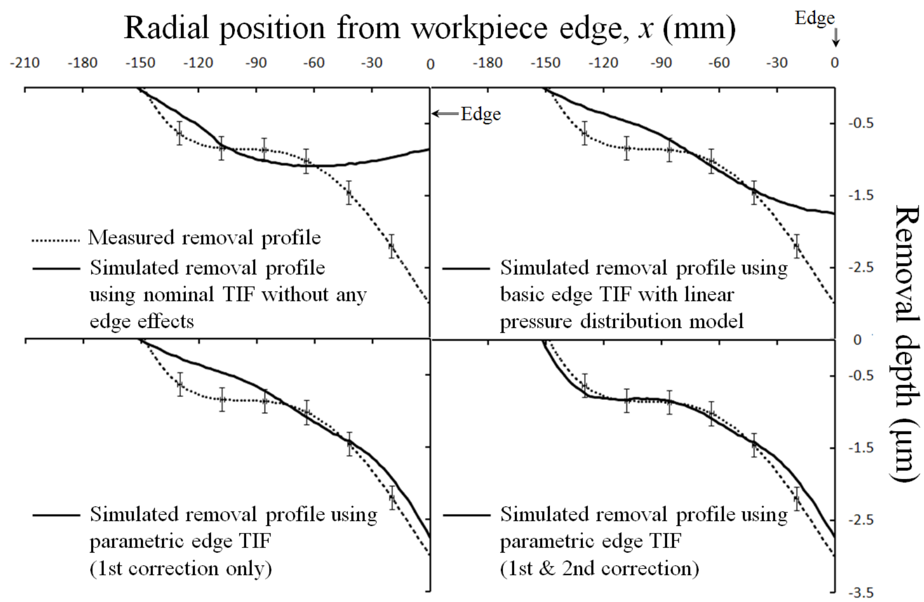

Fig. 7. Measured (with RMS error bars) vs simulated (using different edge TIF models) edge removal profiles for the orbital tool motion case.

The comparison between the four TIF models is presented in Fig. 8. We define normalized fit residual, Δ, as a figure of merit to quantify the performance of the parametric model compared to the data. This is normalized as

$$\Delta = normalized\ fit\ residual = \frac{RMS\ of\ (data - model)}{RMS\ of\ data} \cdot 100\ (\%) \tag{8}$$

It is clear that the normalized fit residual, Δ, is relatively low (about 10~20%) for all TIF model cases when the overhang ratio is small (S_{TIF}<0.14 for orbital case and S_{TIF}<0.02 for spin case). It basically means that there is no difference between nominal and edge TIF models when the overhang effects are negligible.

The improvements become significant as the overhang ratio increases. For the orbital tool motion case with S_{TIF}=0.28, the normalized fit residual, Δ, falls to 10% (parametric edge TIF using both corrections) from 52% (nominal TIF), or from 30% (basic edge TIF). For the spin tool motion case with S_{TIF}=0.4, the normalized fit residual, Δ, is dramatically improved to 12% (parametric edge TIF using both corrections) from 87% (nominal TIF), or from 66% (basic edge TIF).

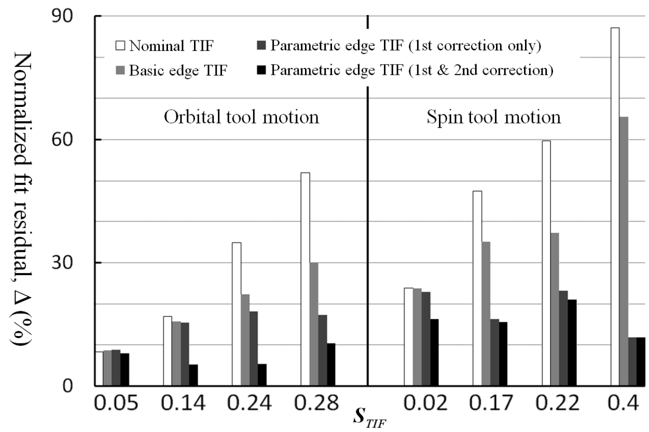

Fig. 8. Normalized fit residual, Δ, of the simulated removal profiles using different TIF models for orbital and spin tool motions.

5. PARAMETRIC EDGE TIF LIBRARY

5.1 Generation of the TIF library

A TIF is the material removal map for a given specific CCOS configuration, which includes tool shape, tool motion, workpiece motion, tool position and so forth. For instance, the TIF is a function of the tool position on the workpiece since the relative motion between the tool and workpiece changes as the tool moves on the workpiece.

The TIF library is a collection of these TIFs at various positions on the workpiece for a given polishing configuration. The shape, size and magnitude of the TIFs are directly related with the tool size, tool motion, and tool shape.

5.2 Parametric edge TIF library

The parametric edge TIF library was generated from the edge model for various tool shapes, tool motions, and tool sizes. We assumed same control parameter values as the experimental cases in Section 4.1 and 4.2 (Orbital tool motion: α=0.2, β=4, γ=0.4, δ=20, ε=1.5 and Spin tool motion: α=0.4, β=6, γ=0.3, δ=-3, ε=0.9). The relative rotation speed between the tool and workpiece was also varied since it plays an important role to determine the TIF shapes. These CCOS configuration parameters for the TIF library are listed in Appendix A.1. The parametric edge TIF library is provided in Appendix A.2.

The tool shape and its edge TIF (S_{TIF} = 0.3) are presented in the second and third column of the library table in Appendix A.2. The edge TIF is the material removal map under the tool-workpiece contact area when the tool overhangs. The ring TIF is the removal map when the workpiece rotates under the tool motion. This removal map looks like a ring (e.g. donut) on the workpiece. The relative speed between the tool motion and the workpiece rotation was considered to generate it. This is a function of the radial position of the edge TIF center, ρ, on the workpiece. The ring TIF profiles in Appendix A.2 only displays for ρ = 75, 80, 85, 90cm (i.e. S_{TIF} = 0, 0.1, 0.2, 0.3) cases in this paper. The full TIF library includes the ring TIFs for all ρ values.

Different tool shapes (circle, ellipse, square, and so forth) with different tool motions (spin and orbital) were used to generate the TIF library No.1 ~ 10. The relative speed between the tool and workpiece motion was changed in TIF library No. 11 ~ 20.

6. CONCLUDING REMARKS

We presented a parametric edge TIF library based on the parametric edge model that allows accurate simulation of edge effects when a tool overhangs the workpiece edge. This parametric edge TIF library is used to design (or optimize) an edge figuring process using the CCOS techniques [17]. Unlike other approaches using analytical pressure distributions to develop edge TIF models, we introduced a parametric approach using a κ map, which represents the spatial distribution of the Preston coefficient. In this way, we were able to express the net effects of many entangled factors affecting the edge removal process in terms of a parametric κ map.

Experimental verification was successfully performed. The normalized fit residual, Δ, for the simulated removal using the parametric edge TIF model stayed in the 5~20% range for all overhang cases, which allows us to correct about 80% of the surface errors (with an assumption that everything else is ideal) in a single CCOS process using the parametric edge TIF library. It means that more than 99% of the initial surface errors can be corrected in 3 CCOS runs. Improvement in convergence rate for the residual surface form error is directly related to more efficient time management and lower cost for large optics fabrication projects. Its significance would be even greater for segmented optical system projects, such as GMT [10] and JWST [11], which have more edges across the whole pupil.

APPENDIX A. PARAMETRIC EDGE TIF LIBRARY

A.1 Parameters for the parametric edge TIF library

Library ID #	**Tool RPM**	**Workpiece RPM**	**Tool width (cm)**	**Tool motion**	**Orbital radius, $R_{orbital}$ (cm)**	**Tool shape**
1	60	0.01	50	Spin	N/A	Circle
2	60	0.01	50	Spin	N/A	Donut
3	60	0.01	40	Orbital	5	Circle
4	60	0.01	40	Orbital	5	Donut
5	60	0.01	40	Orbital	5	Donut
6	60	0.01	40	Orbital	5	Ellipse
7	60	0.01	40	Orbital	5	Ellipse
8	60	0.01	40	Orbital	5	Square
9	60	0.01	40	Orbital	5	Rectangle
10	60	0.01	40	Orbital	5	Rectangle
11	60	-15	50	Spin	N/A	Circle
12	60	-5	50	Spin	N/A	Circle
13	60	1	50	Spin	N/A	Circle
14	60	5	50	Spin	N/A	Circle
15	60	15	50	Spin	N/A	Circle
16	60	-3	40	Orbital	5	Circle
17	60	-1	40	Orbital	5	Circle
18	60	0.01	40	Orbital	5	Circle
19	60	1	40	Orbital	5	Circle
20	60	3	40	Orbital	5	Circle

i) Preston constant [8] was assumed as -100 um/psi(m/sec)hour with 1 PSI tool pressure.
ii) Positive and negative RPM means clockwise and counterclockwise rotation, respectively.
iii) Tool width is measured in the overhang direction.
iv) Workpiece radius was assumed as 100cm.

A.2 Parametric edge TIF library

ID #	Tool Shape (cm × cm)	Normalized edge TIF (cm × cm)	Ring TIF radial, *r*, profiles on the workpiece (*r* axis in cm)
1	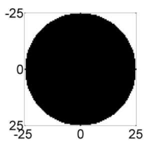	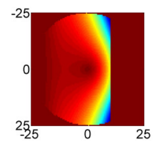	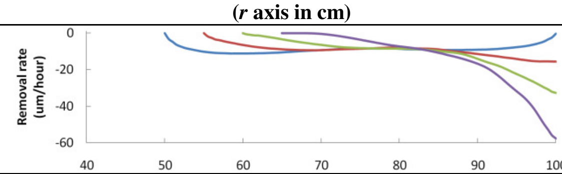
2	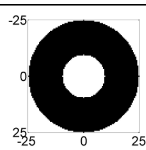	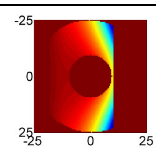	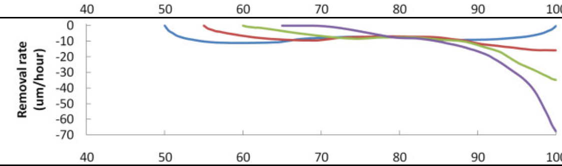
3	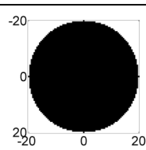	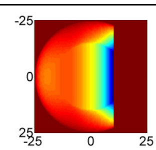	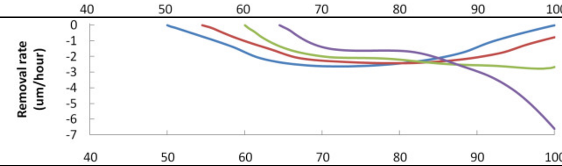
4	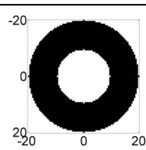	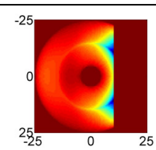	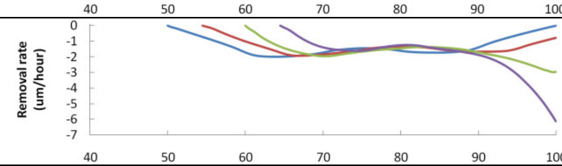
5	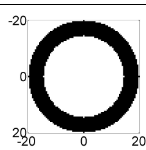	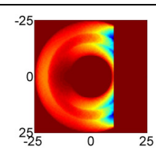	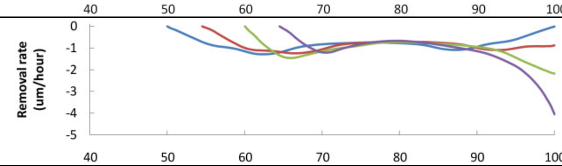
6	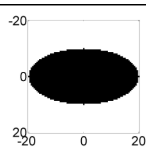	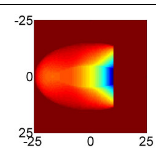	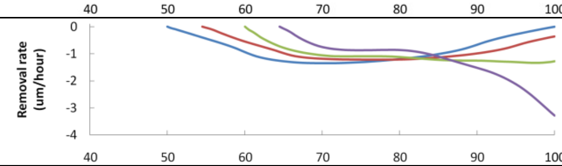
7	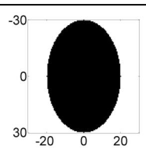	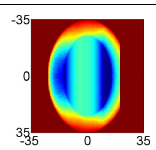	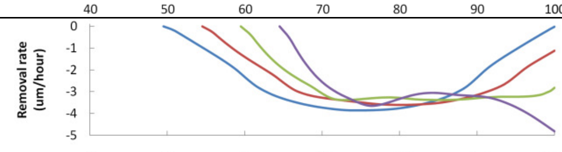
8	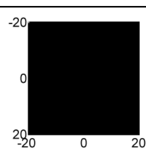	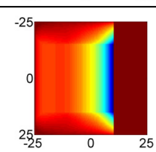	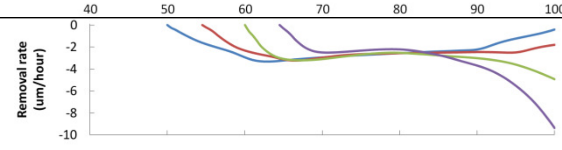
9	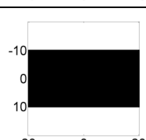	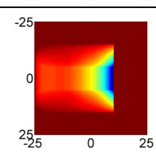	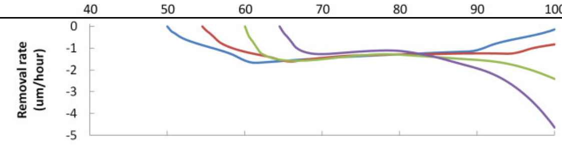
10	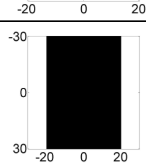	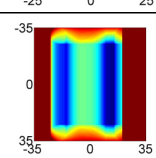	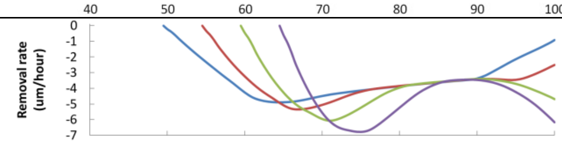

ID #	Tool Shape (cm × cm)	Normalized edge TIF (cm × cm)	Ring TIF radial, *r*, profiles on the workpiece (*r* axis in cm)
11	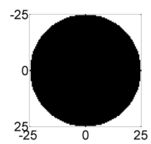	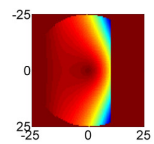	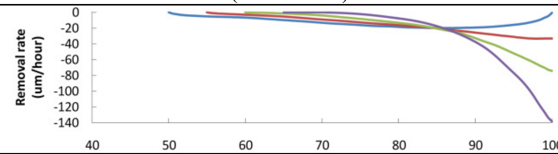
12	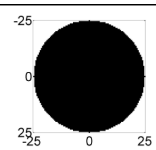	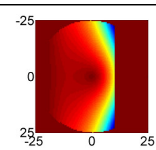	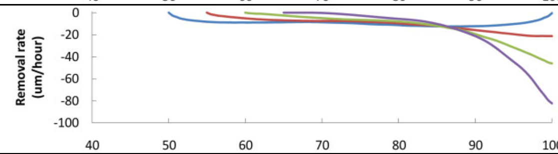
13	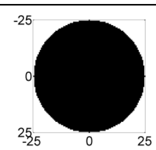	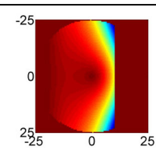	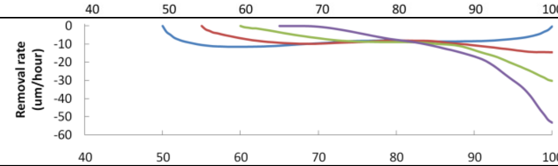
14	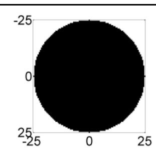	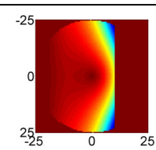	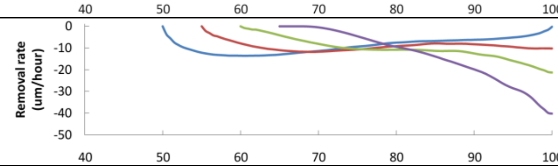
15	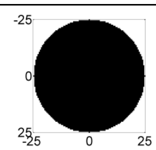	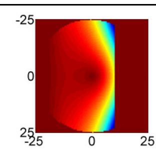	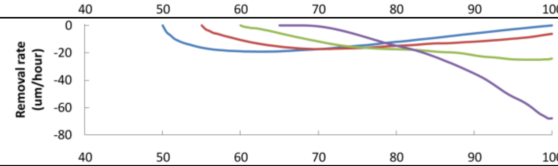
16	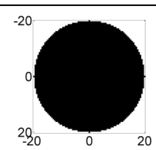	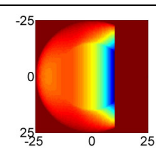	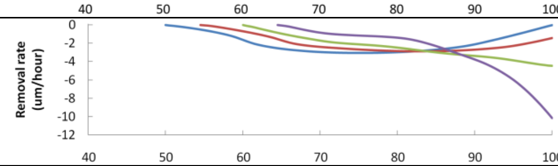
17	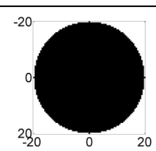	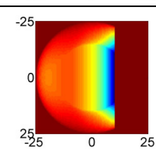	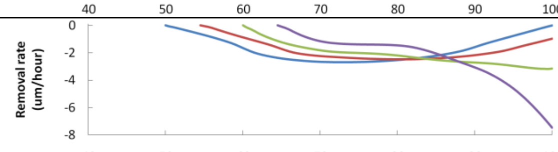
18	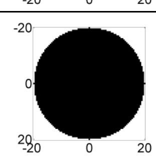	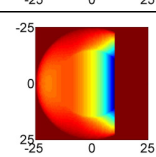	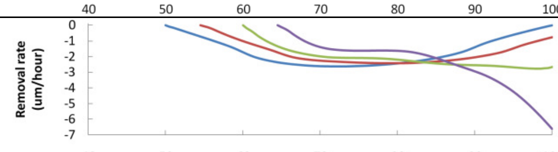
19	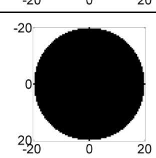	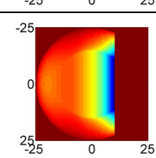	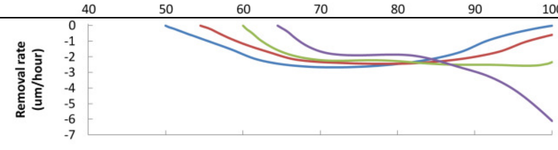
20	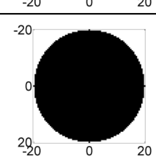	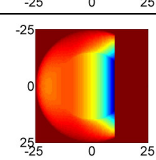	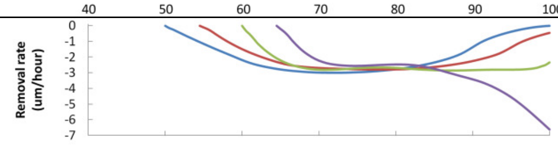

i) Overhang ratio for the ring TIF profiles: S_{TIF} = 0 (blue), 0.1 (red), 0.2 (green), 0.3 (purple)
ii) Edge model parameters for the orbital tool motion: α=0.2, β=4, γ=0.4, δ=20, ε=1.5
iii) Edge model parameters for the spin tool motion: α=0.4, β=6, γ=0.3, δ=-3, ε=0.9
iv) Normalized edge TIF uses same color scale as the edge TIF in Table. 1.

ACKNOWLEDGMENTS

We acknowledge that this work was supported by the Optical Engineering and Fabrication Facility of the College of Optical Sciences at the University of Arizona. We thank Buddy Martin (Steward Observatory Mirror Lab), Anoopoma Bhowmik, and Robert Parks (College of Optical Sciences) at the Univ. of Arizona for assistance in the final manuscript preparation.

REFERENCES

[1] R. Aspden, R. McDonough, and F.R. Nitchie, Jr, "Computer assisted optical surfacing," Appl. Opt. **11**, 2739-2747 (1972).

[2] R. E. Wagner and R. R. Shannon, "Fabrication of aspherics using a mathematical model for material removal," Appl. Opt. **13**, 1683-1689 (1974).

[3] D.J. Bajuk, "Computer controlled generation of rotationally symmetric aspheric surfaces," Opt. Eng. **15**, 401-406 (1976).

[4] R.A. Jones, "Grinding and polishing with small tools under computer control," Opt. Eng. **18**, 390-393 (1979).

[5] R.A. Jones, "Computer-controlled polishing of telescope mirror segments," Opt. Eng. **22**, 236-240 (1983).

[6] R.A. Jones, "Computer-controlled optical surfacing with orbital tool motion," Opt. Eng. **25**, 785-790 (1986).

[7] J.R. Johnson and E. Waluschka, "Optical fabrication-process modeling-analysis tool box," Proc. SPIE **1333**, 106-117 (1990).

[8] R.A. Jones and W.J. Rupp, "Rapid optical fabrication with CCOS," Proc. SPIE **1333**, 34-43 (1990).

[9] D.W. Kim and S.W. Kim, "Static tool influence function for fabrication simulation of hexagonal mirror segments for extremely large telescopes," Opt. Express. **13**, 910-917 (2005).

[10] Matt Johns, "The Giant Magellan Telescope (GMT)," Proc. SPIE **6986**, 698603 (2008).

[11] Mark Clampin, "Status of the James Webb Space Telescope (JWST)," Proc. SPIE **7010**, 70100L (2008).

[12] D.D. Walker, A.T. Beaucamp, D. Brooks, V. Doubrovski, M. Cassie, C. Dunn, R. Freeman, A. King, M. Libert, G. McCavana, R. Morton, D. Riley, and J. Simms, "New results from the Precessions polishing process scaled to larger sizes," Proc. SPIE **5494**, 71-80 (2004).

[13] Bob C. Crawford, Don Loomis, Norm Schenck, and Bill Anderson, Optical Engineering and Fabrication Facility, University of Arizona, 1630 E. University Blvd, Tucson, Arizona 85721, (personal communication, 2008).

[14] Luna-Aguilar E., Cordero-Davila A., Gonzalez Garcia J., Nunez-Alfonso M., Cabrera-Pelaez V.H., Robledo-Sanchez C., Cuautle-Cortez J., and Pedrayes-Lopez M. H., "Edge effects with Preston equation," Proc. SPIE **4840**, 598-603 (2003).

[15] Alberto Cordero-Davila, Jorge Gonzalez-Garcia, Maria Pedrayes-Lopez, Luis Alberto Aguilar-Chiu, Jorge Cuautle-Cortes, and Carlos Robledo-Sanchez, "Edge effects with the Preston equation for a circular tool and workpiece," Appl. Opt. **43**, 1250-1254 (2004).

[16] D.W. Kim, W.H. Park, S.W. Kim and J.H. Burge, " Parametric modeling of edge effects for polishing tool influence functions," Opt. Express. **17**, 5656-5665 (2009).

[17] Dae Wook Kim, College of Optical Sciences, University of Arizona, 1630 E. University Blvd, Tucson, Arizona 85721, S.W. Kim, and James H. Burge are preparing a manuscript to be called "Computer controlled optical surfacing technique using multiple TIF libraries."

Note: The format of this published article was modified to follow the dissertation format.

APPENDIX F

Non-sequential Optimization Technique for a Computer Controlled Optical Surfacing Process using Multiple Tool Influence Functions

Dae Wook Kim, Sug-Whan Kim

and James H. Burge

Journal article published in ***Optics Express***

2009

Copyright Transfer Agreement

The Optical Society of America considers this requested use of its copyrighted materials to be allowed under the OSA Author Agreement submitted by the requester on acceptance for publication of his/her manuscript. It is requested that a complete citation of the original material be included in any publication.

Delois Millner October 22, 2009
Delois Millner Date
Authorized Agent, Optical Society of America

Non-sequential optimization technique for a computer controlled optical surfacing process using multiple tool influence functions

Dae Wook Kim,[1]* Sug-Whan Kim[2] and James H. Burge[1]

[1]*College of Optical Sciences, University of Arizona, 1630 E. University Blvd, Tucson, Arizona 85721, USA*
[2]*Space Optics Laboratory, Dept. of Astronomy, Yonsei University, 134 Sinchon-dong, Seodaemun-gu, Seoul 120-749, Republic of Korea*
**letter2dwk@hotmail.com*

Abstract: Optical surfaces can be accurately figured by computer controlled optical surfacing (CCOS) that uses well characterized sub-diameter polishing tools driven by numerically controlled (NC) machines. The motion of the polishing tool is optimized to vary the dwell time of the polisher on the workpiece according to the desired removal and the calibrated tool influence function (TIF). Operating CCOS with small and very well characterized TIF achieves excellent performance, but it takes a long time. This overall polishing time can be reduced by performing sequential polishing runs that start with large tools and finish with smaller tools. In this paper we present a variation of this technique that uses a set of different size TIFs, but the optimization is performed globally – *i.e.* simultaneously optimizing the dwell times and tool shapes for the entire set of polishing runs. So the actual polishing runs will be sequential, but the optimization is comprehensive. As the optimization is modified from the classical method to the comprehensive non-sequential algorithm, the performance improvement is significant. For representative polishing runs we show figuring efficiency improvement from ~88% to ~98% in terms of residual RMS (root-mean-square) surface error and from ~47% to ~89% in terms of residual RMS slope error.

OCIS codes: (220.0220) Optical design and fabrication; (220.4610) Optical fabrication; (220.5450) Polishing

References and links

1. R. A. Jones, "Computer control for grinding and polishing," Photon. Spectra, 34–39 (1963).
2. R. Aspden, R. McDonough, and F. R. Nitchie, Jr., "Computer assisted optical surfacing," Appl. Opt. **11**(12), 2739–2747 (1972).
3. R. E. Wagner, and R. R. Shannon, "Fabrication of aspherics using a mathematical model for material removal," Appl. Opt. **13**(7), 1683–1689 (1974).
4. R. A. Jones, "Computer-controlled polishing of telescope mirror segments," Opt. Eng. **22**, 236–240 (1983).
5. R. A. Jones, "Computer-controlled optical surfacing with orbital tool motion," Opt. Eng. **25**, 785–790 (1986).
6. J. R. Johnson, and E. Waluschka, "Optical fabrication-process modeling-analysis tool box," in *Manufacturing and metrology tooling for the Solar-A Soft X-Ray Telescope*, W.R. Sigman, L.V. Burns, C.G. Hull-Allen, A.F. Slomba, and R.G. Kusha, eds., Proc. SPIE **1333,** 106–117 (1990).
7. D. D. Walker, D. Brooks, A. King, R. Freeman, R. Morton, G. McCavana, and S. W. Kim, "The 'Precessions' tooling for polishing and figuring flat, spherical and aspheric surfaces," Opt. Express **11**(8), 958–964 (2003).
8. H. M. Pollicove, E. M. Fess, and J. M. Schoen, "Deterministic manufacturing processes for precision optical surfaces," in *Window and Dome Technologies VIII*, R. W. Tustison, eds., Proc. SPIE **5078**, 90–96 (2003).
9. D. W. Kim, and S. W. Kim, "Static tool influence function for fabrication simulation of hexagonal mirror segments for extremely large telescopes," Opt. Express **13**(3), 910–917 (2005).
10. S. D. Jacobs, "International innovations in optical finishing," in Current Developments in *Lens Design and Optical Engineering V*, P.Z. Mouroulis, W.J. Smith, and R.B. Johnson, eds., Proc. SPIE **5523,** 264–272 (2004).
11. J. H. Burge, S. Benjamin, D. Caywood, C. Noble, M. Novak, C. Oh, R. Parks, B. Smith, P. Su, M. Valente, and C. Zhao, "Fabrication and testing of 1.4-m convex off-axis aspheric optical surfaces," in *Optical Manufacturing and Testing VIII*, J. H. Burge; O. W. Fähnle and R. Williamson, eds., Proc. SPIE **7426**, 74260L1–12 (2009).

#116367 - $15.00 USD Received 28 Aug 2009; revised 30 Oct 2009; accepted 6 Nov 2009; published 18 Dec 2009

12. M. Johns, "The Giant Magellan Telescope (GMT)," in *Extremely Large Telescopes: Which Wavelengths?* T. E. Andersen, eds., Proc. SPIE **6986**, 698603 1–12 (2008).
13. J. Nelson, and G. H. Sanders, "The status of the Thirty Meter Telescope project," in *Ground-based and Airborne Telescopes II*, L. M. Stepp and R. Gilmozzi, eds., Proc. SPIE **7012**, 70121A1–18 (2008).
14. D. D. Walker, A. P. Doel, R. G. Bingham, D. Brooks, A. M. King, G. Peggs, B. Hughes, S. Oldfield, C. Dorn, H. McAndrews, G. Dando, and D. Riley, "Design Study Report: The Primary and Secondary Mirrors for the Proposed Euro50 Telescope" (2002), *http://www.zeeko.co.uk/papers/dl/New%20Study%20Report%20V%2026.pdf*.
15. T. Andersen, A. L. Ardeberg, J. Beckers, A. Goncharov, M. Owner-Petersen, H. Riewaldt, R. Snel, and D. Walker, "The Euro50 Extremely Large Telescope," in *Future Giant Telescopes*, J.R.P. Angel and R. Gilmozzi, eds., Proc. SPIE **4840**, 214–225 (2003).
16. A. Ardeberg, T. Andersen, J. Beckers, M. Browne, A. Enmark, P. Knutsson, and M. Owner-Petersen, "From Euro50 towards a European ELT," in *Ground-based and Airborne Telescopes*, L. M. Stepp, eds., Proc. SPIE **6267**, 626725 1–10 (2006).
17. R. E. Parks, "Specifications: Figure and Finish are not enough," in *An optical Believe It or Not: Key Lessons Learned*, M. A. Kahan, eds., Proc. SPIE **7071**, 70710B1–9 (2008).
18. J. M. Hill, "Optical Design, Error Budget and Specifications for the Columbus Project Telescope," in *Advanced Technology Optical Telescopes IV*, L. D. Barr, eds., Proc. SPIE **1236**, 86–107 (1990).
19. D. W. Kim, W. H. Park, S. W. Kim, and J. H. Burge, "Parametric modeling of edge effects for polishing tool influence functions," Opt. Express **17**(7), 5656–5665 (2009).
20. A. P. Bogodanov, "Optimizing the technological process of automated grinding and polishing of high-precision large optical elements with a small tool," Sov. J. Opt. Technol. **52**, 409–413 (1985).
21. C. L. Carnal, C. M. Egert, and K. W. Hylton, "Advanced matrix-based algorithms for ion beam milling of optical components," in *Current Developments in Optical Design and Optical Engineering II*, R. E. Fischer and W. J. Smith, eds., Proc. SPIE **1752**, 54–62 (1992).
22. M. Negishi, M. Ando, M. Takimoto, A. Deguchi, and N. Nakamura, "Studies on super-smooth polishing (2nd report)," J. Jpn. Soc. Precis. Eng. **62**, 408–412 (1996).
23. H. Lee, and M. Yang, "Dwell time algorithm for computer-controlled polishing of small axis-symmetrical aspherical lens mold," Opt. Eng. **40**(9), 1936–1943 (2001).
24. W. H. Press, B. P. Flannery, S. A. Teukolsky, and W. T. Vetterling, *Numerical recipes in C* (Cambridge, 1988)
25. C. Bob, Crawford, Don Loomis, Norm Schenck, and Bill Anderson, Optical Engineering and Fabrication Facility, University of Arizona, 1630 E. University Blvd, Tucson, Arizona 85721, (personal communication, 2008).
26. D. W. Kim, W. H. Park, S. W. Kim, and J. H. Burge, "Edge tool influence function library using the parametric edge model for computer controlled optical surfacing," in *Optical Manufacturing and Testing VIII*, J. H. Burge; O. W. Fähnle and R. Williamson, Proc. SPIE **7426**, 74260G1–12 (2009).
27. P. R. Goode, C. J. Denker, L. I. Didkovsky, J. R. Kuhn, and H. Wang, "1.6 m Solar Telescope in Big Bear – the NST," J. Korean Astron. Soc. **35**, 1–8 (2002).
28. A. Heller, "Safe and sustainable energy with LIFE" (2009), *https://str.llnl.gov/AprMay09/pdfs/05.09.02.pdf*.
29. H. H. Barrett, and K. J. Myers, *Foundations of Image Science* (Wiley, 2004)
30. D. W. Kim, and S. W. Kim, "Novel simulation technique for efficient fabrication of 2m class hexagonal segments for extremely large telescope primary mirrors," in *Optical Design and Testing II*, Y. Wang, Z. Weng, S. Ye and J. M. Sasian, eds., Proc. SPIE **5638**, 48–59 (2005).

1. Introduction

Many computer controlled optical surfacing (CCOS) processes have been developed and used since 1963 [1–8]. These CCOS processes are usually aimed at three characteristics, i) low tooling overhead, ii) deterministic material removal and iii) embedded process control intelligence [9,10].

These CCOS techniques have been successfully used for fabrication of large aspheric optical surfaces, including off-axis segments [4–8,11]. Nevertheless, further development in the efficiency and performance of the CCOS techniques is highly desired to meet the demanding target specifications of the next generation Extremely Large Telescope (ELT) projects, such as those for Giant Magellan Telescope (GMT), Thirty Meter Telescope (TMT), and European Extremely Large Telescope (EELT) [12–16].

Those ELTs use giant segmented primary mirrors with hundreds of square meter collecting area, and may have hundreds of segments. Each meter-class segment is to have the surface form accuracy of better than 18nm peak-to-valley [14]. Such a primary mirror system is to be phased and aligned to the precision of about 10-20nm RMS (root-mean-square) [15]. Also, mid-spatial frequency error (*a.k.a.* tool marks) suppression on these precision optical surfaces is important for maximum performance (*i.e.* less scattering, well defined point spread function) of the optical systems [17]. Most of the recent large optical surfaces have been

#116367 - $15.00 USD Received 28 Aug 2009; revised 30 Oct 2009; accepted 6 Nov 2009; published 18 Dec 2009

polished until the spatial frequencies of the surface errors satisfied a target structure function or power spectrum density (PSD) specification to quantify the target form accuracy as a function of spatial frequencies [17,18]. Thus, the improved CCOS technique must provide an efficient fabrication process for a mass-fabrication of precision optical surfaces while minimizing the mid-spatial frequency error.

In a conventional CCOS process, a dwell time map (*i.e.* ablation time as a function of position on the workpiece) of a tool influence function (TIF) is optimized as the major optimization parameter to achieve a target material removal (*i.e.* target error map). The TIF represents instantaneous material removal for a tool with specific motion. Then a numerically controlled polishing machine executes the optimized dwell time map on the workpiece by altering the transverse speed of the tool [1–7].

The convergence rate and overall efficiency of CCOS figuring are optimized using a sequence of polishing runs, where the largest scale irregularities are addressed by large tools. Smaller tools are used to correct small scale irregularities and tool marks from the larger tools. This method works, but may not be optimal.

The new CCOS process suggested here uses a non-sequential optimization technique utilizing multiple TIFs simultaneously in a single CCOS run optimization, while the conventional CCOS processes use TIFs one by one in a sequential manner. The actual polishing runs are still to be sequential under the guidance of comprehensive optimization. This new technique, which enables the ensemble of various TIFs, forms an attractive solution for the mass fabrication capability of high quality optical surfaces.

The theoretical background for the non-sequential optimization technique is presented in Section 2. We introduce, in Section 3, the non-sequential optimization engine in detail, and discuss its novelty over the conventional methods. A reference TIF library (*i.e.* collection of different TIFs) is provided also. Simulation results are presented to demonstrate the performance of the new technique in Section 4. Section 5 summarizes the implications.

2. Theoretical background

2.1 Generation of the TIF library

A TIF is the material removal foot-print for a given tool and tool motion, which can be calculated based on Preston's equation [9], but is usually measured directly. Because the material removal process is affected by the workpiece motion and edge effects, which are the function of tool position on the workpiece, the TIF is also changed according to its center position on the workpiece [19]. For instance, the relative motion between the tool and workpiece varies as the tool moves on the workpiece. Also, the tool removes more material near the workpiece edge as the tool overhangs the workpiece [19].

We define a TIF library as a collection of these TIFs depending on tool shape, tool motion, and lap materials. The TIFs are parameterized as functions of positions on the workpiece. The shape, size and magnitude of the TIFs are directly calculated from these tool configuration parameters. Two common edge TIFs from a circular tool with orbital and spin tool motion are depicted in Fig. 1 [19]. The TIF library for various tool configuration cases is provided in Appendix A.

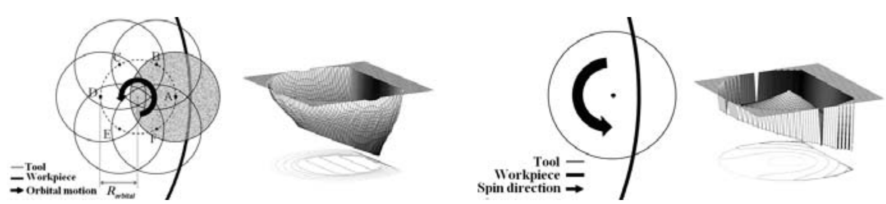

Fig. 1. Orbital (left) and spin (right) tool motion with their parametric edge TIFs [19].

#116367 - $15.00 USD Received 28 Aug 2009; revised 30 Oct 2009; accepted 6 Nov 2009; published 18 Dec 2009

2.2 Dwell time map optimization using merit functions

One key factor of successful CCOS processes is the dwell time optimization technique which provides the closest (ideally equal) removal map to the target removal map (*e.g.* measured errors on the optical surface). This optimization is also known as a de-convolution of the target removal map using a TIF. A TIF can be regarded as an impulse response of a tool with a given tool motion. In other words, a TIF represents the instantaneous material removal for a unit time at a location on the workpiece. The removal map (*i.e.* accumulated TIFs over the whole workpiece) after the tool finishes its path on the workpiece can be expressed as

$$\begin{aligned} &Removal\_map(x_{workpiece}, y_{workpiece}) \\ &= Dwell\_time\_map(x_{workpiece}, y_{workpiece}) ** TIF(x_{TIF}, y_{TIF}, x_{workpiece}, y_{workpiece}) \end{aligned} \tag{1}$$

where $x_{workpiece}$, $y_{workpiece}$ are the coordinates on the workpiece, x_{TIF}, y_{TIF} the coordinates on the TIF, and ** is the two dimensional convolution operator.

Because no general solution to the dwell time map in Eq. (1) exists, as briefly explained in Appendix B, finding the best dwell time map solution becomes an optimization problem. There has been a wide range of study for dwell time map optimization techniques (*e.g.* Fourier transform based algorithms, matrix-based least-squares algorithms) [20–23]. For all optimization techniques, it is very important to define a relevant merit function (*i.e.* objective function) to search for the optimal solution. The merit function for the non-sequential optimization technique is presented in Section 3.4.

3. Non-sequential optimization technique using multiple TIFs

3.1 Conventional (i.e. sequential) vs. non-sequential optimization technique

For the case of conventional (*i.e.* sequential) CCOS optimization, a dwell time map for one TIF has been the major search space for the optimal solution. In other words, an optimization engine searches for the optimal dwell time values for a TIF on the workpiece, which gives the best residual error map. After the CCOS run is executed, another (or same) TIF is used for the next dwell time map optimization to attack the residual error map. This sequential process is repeated, usually using successively smaller TIFs until the target specification is achieved.

In contrast, the non-sequential optimization approach uses various TIFs in a single optimization, simultaneously. Each TIF has its own dwell time map. Thus, multiple dwell time maps are brought into the non-sequential optimization engine, and optimized to achieve the target removal map. The total removal comes from the combination of all different TIFs and their own dwell time maps. Unlike the conventional technique using TIFs sequentially, different TIFs are used together to support each other in a single optimization. Non-linear optimization allows TIFs with low significance (*i.e.* ignorable dwell time or removal) to be extracted from the TIF library during the optimization. However, the key difference of the non-sequential technique from the conventional one is not the number of utilized TIFs. The conventional case may use as many TIFs as the non-sequential case in sequential manner. The major improvement comes from considering all TIFs at the same time, so that the optimal combinations of TIFs are used in constructive manner to improve the performance of the CCOS process.

For instance, a large square tool with orbital tool motion may be selected to remove most of the low spatial frequency errors on the workpiece. A small TIF from a circular tool with spin tool motion may be chosen with the large square tool TIF as an optimal set to achieve high figuring efficiency (defined in Section 4.1) by removing localized small errors. As a result, the mid-spatial frequency error on the workpiece, often caused by the small tool, can be minimized because the small tool was used only for a short time. Some specialized TIFs such as the parametric edge TIFs in Fig. 1 may be utilized for an edge figuring optimization.

In summary, both conventional and non-sequential optimization techniques are used to find an optimal dwell time map solution. However, there are significant differences, which make the non-sequential technique more powerful than the conventional one. The

#116367 - $15.00 USD Received 28 Aug 2009; revised 30 Oct 2009; accepted 6 Nov 2009; published 18 Dec 2009

optimization engine now has wider search space, including tool shape, tool size, tool motion, and so forth. These various tool configuration parameters were formerly the human's decision in the conventional CCOS technique. Many different combinations of the various TIFs are simulated to find an optimal TIF set. This technical advance leads to improvements in figuring efficiency and mid-spatial frequency error reduction, which are demonstrated in Section 4.

3.2 Non-sequential optimization engine using the gradient search method

The non-sequential optimization engine was developed using the gradient search (*a.k.a.* steepest descent) method [24]. The method is known as one of the most simple and straight forward optimization technique which works in search spaces of any number of dimensions. This method presupposes that the gradient of the merit function space at a given point can be computed. It starts at a point, and moves to the next point by minimizing a figure of merit along the line extending from the initial point in the direction of the downhill gradient. This procedure is repeated as many times as required. Because the search space for the non-sequential optimization also has multiple dimensions (*i.e.* many TIFs with various tool configuration parameters), the gradient descent method is suitable for our application.

There are two general weaknesses in the gradient descent method. First, it may take many iterations to converge towards the optimal solution in the search space, especially if the search space has complex variations [24]. This problem can be minimized by putting only reasonable TIFs in the TIF library. For instance, if we put a too small TIF (*e.g.* 5cm in diameter) in the TIF library to optimize an 8m diameter target removal map, the curvature of the figure of merit values along the 5cm TIF direction may be very shallow compared to the other reasonable size TIF (*e.g.* 20, 35, or 50cm in diameter) directions. Thus, including a 5cm TIF to the TIF library is inappropriate in this case. Limiting the total number of TIFs in the library improves computing efficiency. We do not rely on especially powerful computers for this work. Most of the optimization runs (including the case study runs in Section 4) are finished in 2-10 minutes on a regular desktop PC. Second, an improper perturbation step to calculate the local gradient may result in poor optimization performance. However, most of the search space dimensions are not a continuous space, but a discrete space depending on the given TIF library. For instance, there are only five available tool sizes (30, 40, 50, 60, and 70cm) in the reference TIF library in Table 3 (Appendix A). Although we carefully claim that the gradient descent method is suitable for this application, we still acknowledge the possibility of undesired optimization results for some special cases. For example, the TIFs are not orthogonal functions. Consequentially, the sequential application of TIFs for the optimization engine may not lead to the global minimum, but to a local minimum. However, we have not yet observed such cases in our trial optimization runs. Some actual optimization results using this optimization method are demonstrated in Section 4.

The schematic flow chart for the non-sequential optimization technique is shown in Fig. 2. The TIF library is fed into the non-sequential optimization engine to calculate the optimal dwell time maps for each TIF. More explanation about the TIF library is presented in Section 3.3. In order to calculate the local gradient in the multi-dimensional search space, the optimization engine begins to perturb the dwell time maps, which have a constant value initially. A minimum dwell time is applied during the perturbations to avoid an impractically small dwell time at a position on the workpiece. Because an actual computer controlled polishing machine (CCPM) has its mechanical limitations (*e.g.* maximum acceleration), the minimum dwell time is set by the CCPM specification. The optimization engine evaluates each TIF to achieve the target removal map for all possible TIF locations on the workpiece. For each trial, the change in the total figure of merit, FOM_{total} in Section 3.4, is recorded to determine the steepest descent case as follows. Using the TIFs with their own dwell time maps for each perturbation case, the expected removal maps are calculated using Eq. (1). The difference between the total expected removal map (*i.e.* sum of all expected removal maps from each TIF) and the target removal map is the residual error map. This residual error map is used to evaluate the FOM_{total}. After all TIFs (*i.e.* dimensions of the search space) have been

#116367 - $15.00 USD Received 28 Aug 2009; revised 30 Oct 2009; accepted 6 Nov 2009; published 18 Dec 2009

tried, the optimization engine updates the dwell time maps with the optimal trial, which recorded the steepest improvements in FOM_{total}.

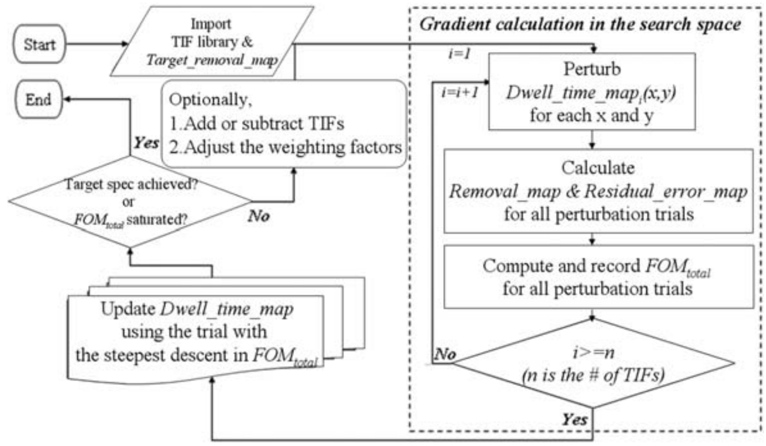

Fig. 2. Flow chart for the non-sequential optimization technique using the gradient descent method

The optimization engine repeats this procedure in a loop until FOM_{total} reaches the specification or does not decrease anymore (*i.e.* saturated). The current dwell time maps for each TIF become the optimization result. If these conditions are not met, more TIFs are fed into the TIF library. The TIFs which were hardly used are extracted from the TIF library. By performing more rounds of optimization using the updated TIF library, the optimal TIF set with their dwell time maps is determined eventually.

3.3 TIF library

The search space, including the tool configuration parameters, is defined by the TIF library in practice. Even though infinite numbers of TIFs are possible in theory, the non-sequential optimization engine utilizes the TIFs provided in the library. For instance, a typical pitch tool can be carved into any shape [25]. However, due to the limited resources (*e.g.* computing power, time), only reasonable TIFs need to be generated and saved in the library. A square tool, a circular tool, and a sector tool (*e.g.* TIF #7 in Fig. 6, Appendix A) with orbital or spin tool motions may create a sufficient tool shape search space (*i.e.* TIF library) for most cases. Also, the shop does not need to have a large inventory for all tools in the library. Only some optimal tool sets need to be made and maintained.

A complimentary TIF library was generated and provided using various tool shapes, tool motions, and tool sizes as mentioned in Section 2.1. The TIF library can be used as a good reference when one designs a CCOS run using multiple TIFs. The relative rotation speed between the tool and workpiece was changed since it played an important role to determine the TIF shape. These parameters for the TIF library are listed in Table 3 (Appendix A). The tool shape with its static TIF and ring TIF profiles are presented in Fig. 6 (Appendix A). The static TIF shows a material removal map under the tool motion for a unit time without any workpiece motion (*i.e.* workpiece RPM = 0). The ring TIF is the axisymmetric removal profile when the workpiece also rotates, and is calculated using the relative speed between the tool motion and the workpiece rotation. The ring TIF looks like a ring (*i.e.* donut) on the workpiece. The ring TIF shape is a function of radial position of the TIF center, ρ, on the workpiece. The ring TIF radial profiles in Fig. 6 are only displayed for ρ = 50, 150, and 250cm. The full TIF library includes the ring TIFs for all ρ values on the workpiece. These two different types of TIFs can be selected depending on the relative speed between the tool and workpiece. If the workpiece motion is slow compared to the tool motion, the static TIFs are used because their shapes do not change significantly by the workpiece motion. However,

#116367 - $15.00 USD Received 28 Aug 2009; revised 30 Oct 2009; accepted 6 Nov 2009; published 18 Dec 2009

if the workpiece rotates quickly, then the ring TIFs, which incorporate the workpiece motion effect, are used.

Different tool shapes (circle, ellipse, square, sector and so forth) with different tool motions (spin and orbital) were used to generate the TIF library No.1-10. The relative speed between the tool and workpiece motion was changed in TIF library No. 11-20. As shown in the ring TIFs, the removal profiles can be skewed by changing the relative rotation directions between the tool and workpiece. This technique has been often used to correct the edge errors by opticians manually [25]. The circular tool diameter was changed from 70cm to 30cm to show the effect of the tool size in TIF size and magnitude. These TIFs are shown in TIF library No. 21-25. Some TIFs using the parametric edge TIF models [19] are presented in TIF library No. 26-30. More parametric edge TIFs are available in the previous study [26].

3.4 Merit functions for the non-sequential optimization technique

The non-sequential optimization technique provides an optimal solution which suppresses the mid-spatial frequency error while still maintaining the high figuring efficiency as mentioned in Section 3.1. In order to find the optimal solution, the merit functions must completely represent the residual error map in terms of the RMS of the error map, mid-spatial frequency error, and newly generated local error features. Also, the computational load for the merit function calculations should be minimized, because the calculations are placed in the optimization loop.

The figure of merit used for this work combines six different merit functions using RSS (root-sum-square) as follows:

$$FOM_{total} \equiv RSS_{RMS\_errors} = \sqrt{\sum_{i=1}^{6} C_i \cdot FOM_i^{\,2}} \quad (2)$$

where $C_{1\text{-}6}$ is the weighting factors for $FOM_{1\text{-}6}$. Each FOM_i is defined as

$$FOM_1 \equiv RMS\ of\ Positive\ Error\ Map = \sqrt{\iint_{M+} \{error\_map(x,y)\}^2 dxdy \Big/ \iint_{M} dxdy} \quad (3)$$

$$FOM_2 \equiv RMS\ of\ Negative\ Error\ Map = \sqrt{\iint_{M-} \{error\_map(x,y)\}^2 dxdy \Big/ \iint_{M} dxdy} \quad (4)$$

$$FOM_3 \equiv RMS\ of\ x\,Slope\ Map = \sqrt{\iint_{M} \{\frac{\partial}{\partial x} error\_map(x,y)\}^2 dxdy \Big/ \iint_{M} dxdy} \quad (5)$$

$$FOM_4 \equiv RMS\ of\ y\,Slope\ Map = \sqrt{\iint_{M} \{\frac{\partial}{\partial y} error\_map(x,y)\}^2 dxdy \Big/ \iint_{M} dxdy} \quad (6)$$

$$FOM_5 \equiv RMS\ of\ x\,Curvature\ Map = \sqrt{\iint_{M} \{\frac{\partial^2}{\partial x^2} error\_map(x,y)\}^2 dxdy \Big/ \iint_{M} dxdy} \quad (7)$$

$$FOM_6 \equiv RMS\ of\ y\,Curvature\ Map = \sqrt{\iint_{M} \{\frac{\partial^2}{\partial y^2} error\_map(x,y)\}^2 dxdy \Big/ \iint_{M} dxdy} \quad (8)$$

where the surface integral limit M represents the error map surface. M + and M- are the error map areas with positive and negative residual error values, respectively. The six weighting factors can be adjusted depending on a specific purpose of a CCOS run as a design parameter.

The RMS deviation of the error map is calculated using FOM_1 and FOM_2. FOM_1 is the RMS of the positive error map, where the final surface is still higher than the target surface. FOM_2 is the RMS of the negative error map, where the final surface is lower than the target

#116367 - $15.00 USD Received 28 Aug 2009; revised 30 Oct 2009; accepted 6 Nov 2009; published 18 Dec 2009

surface. Because the polishing process can only remove material from the workpiece, the surface often needs to be kept higher than the target surface to a certain extent during the polishing process. This can be achieved by increasing the weighting factor C_2 for FOM_2. At the final polishing run to finish the project, both FOM_1 and FOM_2 may need to be minimized with the same weightings ($C_1 = C_2$) to minimize the conventional RMS of the error map.

The RMS deviation of the surface slope map [*i.e.* FOM_3 & FOM_4 in Eq. (5) and (6)] and the RMS deviation of the surface curvature map [FOM_5 & FOM_6 in Eq. (7) and (8)] are used to quantify the mid-spatial frequency error and localized small errors. The approaches using Fourier transform or PSD based figure of merits were excluded due to their computing power requirements. In contrast, the differential calculations in FOM_3, FOM_4, FOM_5 and FOM_6 can be easily done for a numerical data set (*e.g.* matrix for a pixelized error map) in most computing language platforms, such as MATLAB™.

The total figure of merit FOM_{total} combines the functions $FOM_{1\text{-}6}$ with appropriate weighting coefficients depending on the purpose of a CCOS run, and provides a good criterion to optimize a CCOS run using a TIF library. For instance, if large C_3 and C_4 values were entered, the optimization engine would try to minimize the slope errors on the final workpiece. By minimizing FOM_{total}, the non-sequential optimization engine prevents the unwanted mid-spatial frequency error and localized small errors, while it achieves a small RMS of the residual error map.

4. Performance

4.1 High figuring efficiency

The figuring efficiency of a CCOS process can be maximized when an optimal TIF set is used for a given target removal. Four cases were simulated to demonstrate the performance of the non-sequential optimization. The figuring efficiency (FE) is defined by

$$FE \equiv \frac{RMS_{initial\_error\_map} - RMS_{residual\_error\_map}}{RMS_{initial\_error\_map}} \cdot 100 \qquad [\%]. \tag{9}$$

The advantage of performing the simultaneous optimization was demonstrated by comparing two case studies, Case 1.1 and 1.2. A 1µm piston target removal profile for a 2m radius workpiece was used. The piston target removal is often desired when one tries to remove sub-surface damages on a workpiece without changing the figure of the surface. A TIF using an 84cm circular tool with orbital tool motion was used as a primary TIF to achieve the target removal inside the workpiece edge. An 84cm sector tool was given for a secondary edge TIF. Only these two TIFs were used for both cases for a fair comparison, even though the non-sequential case may use other edge TIF as an optimal set with the primary TIF. The simulation results are presented in Fig. 3.

Case 1.1 did not use the non-sequential optimization technique. The given piston target removal was optimized using the primary TIF first. Then, the residual removal profile was optimized using the secondary edge TIF. The removal profile using the primary TIF (green dotted line in Case 1.1, Fig. 3) removed the target error to the edge as much as possible at the expense of having a bump around 100-120cm radial region. Also, the residual removal profile was not matched well with the removal using the secondary TIF (brown dotted line in Case 1.1, Fig. 3), so that the secondary TIF could not perform its role well. This is because the first optimization using the primary TIF did not consider the possible removal using the secondary TIF in the following optimization. This is a good example to show the fundamental limitation of the sequential approach. Finally, the residual profile shows relatively low figuring efficiency, FE = 88%, since those two TIFs were not utilized in a constructive manner.

Case 1.2 was optimized using the non-sequential optimization technique, where both the primary and secondary TIFs were considered simultaneously during the optimization process. Thus, the primary TIF intentionally left the edge side error, which was fit with the secondary edge TIF from the 84cm sector tool. As a result, a high figuring efficiency (FE = 98.4%) was accomplished. The two removal profiles from both TIFs (green and brown dotted lines in

#116367 - $15.00 USD Received 28 Aug 2009; revised 30 Oct 2009; accepted 6 Nov 2009; published 18 Dec 2009

Case 1.2, Fig. 3) matched well, so that the total removal (blue solid lines in Case 1.2, Fig. 3) is almost a constant (*i.e.* piston) removal profile. The residual error (red solid line in Case 1.2, Fig. 3) shows flat profile, which is much improved over Case 1.1.

Case No.	NS mode [a]	Utilized polishing tools (with tool motion) and radial profiles	RMS_{ini}, RMS_{res}, FE [b]
1.1	off (2)	A: 84cm circular tool (orbital), B: 84cm sector tool (orbital) 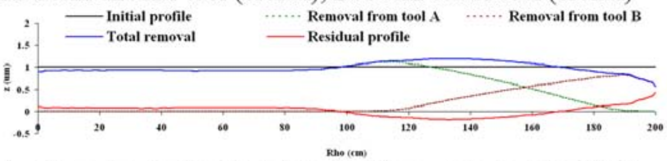	1μm 0.12μm 88%
1.2	on (2)	A: 84cm circular tool (orbital), B: 84cm sector tool (orbital) 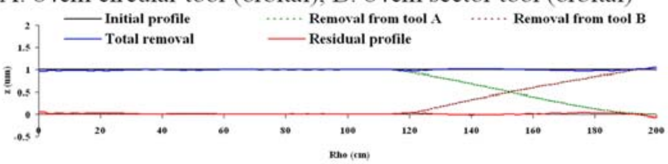	1μm 0.016μm 98.4%
1.3	on (2)	A:30cm circular tool (spin), B:50cm square tool (orbital) 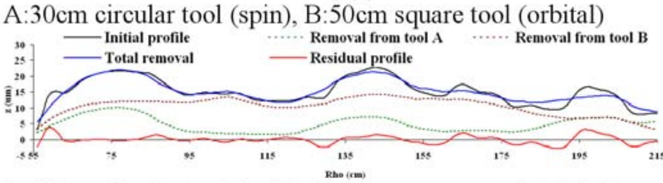	15.71μm 1.30μm 91.7%
1.4	on (5)	A: 20cm circular tool (spin), B: 50cm square tool (orbital) 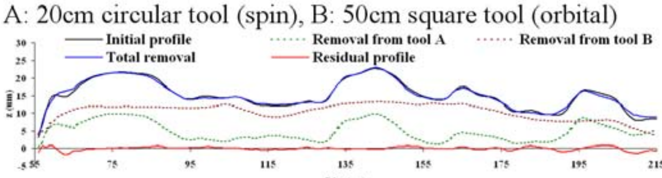	15.71μm 0.50μm 96.8%

[a] NS mode means the non-sequential optimization mode. The number in the parenthesis refers the number of TIFs in the library.
[b] RMS_{ini} and RMS_{res} is the RMS of the initial and residual profile, respectively. FE is the figuring efficiency in Eq. (9).

Fig. 3. Optimization results for Case 1.1-1.4

Two more case studies were conducted to show the value of an optimal TIF set. For Case 1.3 and 1.4, a target removal profile for a 4.3m diameter surface was randomly generated. It has a 0.55m in radius circular hole at the center. This profile is shown as black solid lines (*i.e.* initial profile) in Case 1.3 and 1.4, Fig. 3. The TIF from 50cm square tool with orbital tool motion was given as a common primary TIF.

Case 1.3 was optimized using a secondary TIF from a 30cm circular tool with spin tool motion. The TIF library only had these two TIFs (using the 50cm primary square tool and 30cm circular tool), so that the optimization engine was not allowed to use other TIFs. Case 1.3 in Fig. 3 shows the optimized removal profiles using the 30cm circular tool (green dotted line) and the 50cm square tool (brown dotted line), which was not a good TIF set for the given target error profile. As shown in the residual profile (red solid line in Case 1.3, Fig. 3), most of the localized small errors in the target error profile were not removed since the secondary TIF from the 30cm circular tool was too large to remove them. The un-matched TIFs results in the relatively low figuring efficiency (FE = 91.7%) with hard-to-correct bumpy features on the residual error profile.

#116367 - $15.00 USD Received 28 Aug 2009; revised 30 Oct 2009; accepted 6 Nov 2009; published 18 Dec 2009

Case 1.4 was optimized using five TIFs (using the 50cm primary square tool and 10, 20, 30, 40cm circular tools) in the TIF library. For the direct comparison with Case 1.3 the final number of utilized TIFs was limited to two. As the result of the optimization, a TIF from a 20cm circular tool with spin tool motion was used as the secondary TIF. As you see in the removal profile using the 50cm tool (brown dotted line), the large tool removes most of the low-spatial frequency errors in the target error profile efficiently. Then, the removal profile from the 20cm tool (green dotted line) covers the localized small errors only. Most of the target errors were successfully removed with high figuring efficiency, *FE* = 96.8%.

The comparison between Case 1.1 and 1.2 clearly shows the importance of the simultaneous optimization to achieve high figuring efficiency. Also, Case 1.4 highlights the advantage of utilizing an optimal TIF set for a given target removal.

4.2 Mid-spatial frequency error suppression with high time-efficiency

The performance of the non-sequential optimization technique for the suppression of mid-spatial frequency error (*i.e.* tool marks) was evaluated in a two-dimensional simulation of polishing the 1.6m New Solar Telescope (NST) primary mirror [27]. A 1.6m optical surface map with 701nm RMS of irregular errors was simulated as shown in Fig. 4. The target specification for the residual error map was set as <20nm RMS, the NST primary final optical surface specification [27].

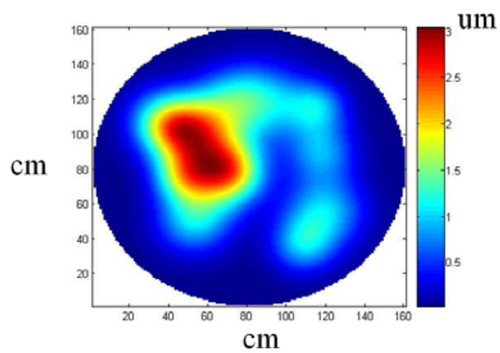

Fig. 4. Randomly generated 1.6m target removal map (surface RMS: 701nm, slope error RMS: 0.522arcsed, error volume: 1.31cm^3)

Due to uncertainties in the actual TIF shapes (including magnitude) and the tool positioning accuracy of the CCPM, the difference between the ideal removal and actual removal tends to produce the mid-spatial frequency error (*i.e.* tool marks) on the finished optical surface.

Large TIFs, which usually have less total dwell time with shorter tool path, are less sensitive to those uncertainties, so that the residual tool marks are limited. However, small TIFs are required to correct localized small errors. Thus, the key for the mid-spatial frequency error suppression is using proper size TIFs for various spatial frequency error components on the workpiece. The non-sequential optimization engine utilizes large and small TIFs for the low-spatial frequency errors and localized small errors, respectively.

For a realistic polishing simulation, we assumed random positioning errors and TIF magnitude variation. Up to 0.5% (of the workpiece size) tool positioning error was used. This positioning error may come from a low resolution measured target removal map, which may have errors in absolute coordinates, or a limited positioning accuracy of the CCPM itself. Up to ± 2.5% random variation in the TIF magnitude was applied during the simulations. This variation is a function of TIF stability, which is a characteristic of each tool. An actual laboratory environment may cause other errors which may degrade the simulation result. The simulation parameters are listed in Table 1.

#116367 - $15.00 USD Received 28 Aug 2009; revised 30 Oct 2009; accepted 6 Nov 2009; published 18 Dec 2009

Table 1. Parameters for the polishing simulation

Parameter	Values	Note
Target form accuracy	<20nm RMS	NST Spec [27].
Available tool sizes	100~300mm	Circular tools
Variation of TIF magnitude	± 2.5%	
Positioning error	± 4mm	0.5% of 1.6m

Three simulations were compared to show the performance of the non-sequential optimization technique in suppressing the mid-spatial frequency error. For the first two cases, Case 2.1 and 2.2, the non-sequential optimization technique was not used. Only a single TIF from the largest tool (300mm in diameter) or the smallest tool (100mm in diameter) was used during the polishing simulations. Case 2.3 utilized multiple TIFs simultaneously. The residual error maps and optimization results are summarized in Fig. 5 and Table 2.

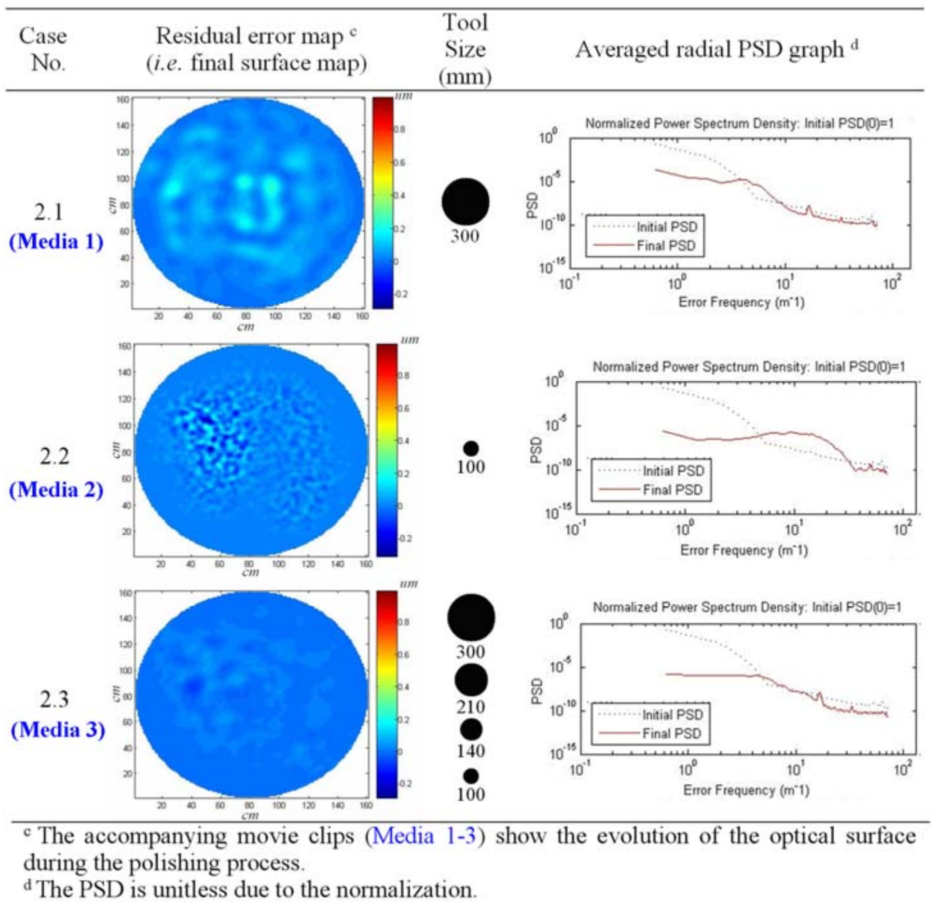

Fig. 5. (Media 1, Media 2, Media 3) Three simulation results for 1.6m NST target removal map.

#116367 - $15.00 USD Received 28 Aug 2009; revised 30 Oct 2009; accepted 6 Nov 2009; published 18 Dec 2009

Table 2. Surface specifications before and after polishing process for Case 2.1-2.3 [e]

Case No.	Initial surface spec. (*i.e.* target error map spec.)			Final surface spec. (*i.e.* residual error map spec.)			Total polishing time (unit time [f])
	Surface error RMS (nm)	Slope error RMS (arcsec)	Error volume (cm^3)	Surface error RMS (nm)	Slope error RMS (arcsec)	Error volume (cm^3)	
2.1	701	0.522	1.31	36 *94.9%*	0.1 *80.8%*	0.072 *94.5%*	82
2.2	701	0.522	1.31	31 *95.6%*	0.277 *46.9%*	0.006 *99.5%*	774
2.3	701	0.522	1.31	10 *98.6%*	0.057 *89.1%*	0.005 *99.6%*	100

[e] Percentile in *italic* represents the improvement ratio with respect to the initial surface specification for the surface error RMS, slope error RMS, and error volume. This is same as the figuring efficiency *FE* for the surface error RMS case.
[f] The 'unit time' was used for the relative comparison between cases.

The largest TIF, Case 2.1, left localized small errors on the final surface as shown in Fig. 5. There was a limitation caused by the small features (>3m^{-1} in the PSD graph) which were relatively smaller than the TIF size. In contrast, for the Case 2.2, almost 99.5% of the form error volume was removed using the smallest TIF. However, it caused significant mid-spatial frequency error on the final optical surface. This is easily observed by comparing the initial and final PSD graphs in Case 2.2, Fig. 5. Even though the low-spatial frequency errors (<5m^{-1}) were removed, there was a significant generation of mid-spatial frequency error (5-30m^{-1}). As a result, the final RMS slope error was 0.277arcsec which was the worst among three cases in Table 2.

The non-sequential optimization result, Case 2.3, showed the best performance in terms of both preventing the mid-spatial frequency error and achieving the high figuring efficiency. The optimization engine used four different TIF diameters, 100, 140, 210 and 300mm, among the available TIF sizes between 100 and 300mm. The PSD graph (in Case 2.3, Fig. 5) shows good suppression (*i.e.* no increase from the initial PSD) in the mid-spatial frequency range (5-30m^{-1}) during the polishing process. This also means that the figures of merit in Section 3.4 were effectively representing the errors in terms of the spatial frequencies in the course of the optimization. The final surface had 0.057arcsec RMS slope variation and 10nm RMS surface irregularity, which meets the target specification. About 99.6% of the initial error volume was removed. This demonstrates that the non-sequential optimization technique successfully balanced between various size TIFs by selecting the large TIFs for most of the error volume and the small TIFs only for the localized small errors. The final surface error map is shown in Case 2.3, Fig. 5.

As shown in Table 2, the total polishing time for non-sequential optimization Case 2.3 (100 unit time) was much smaller compared to the 774 unit time of Case 2.2. While both Case 2.1 and 2.3 show significantly shorter total polishing time, Case 2.3 which used multiple TIFs resulted in superior performance. Thus, the non-sequential optimization technique provides a time-efficient CCOS process with both high figuring efficiency and good mid-spatial frequency error suppression.

5. Concluding remarks

In this paper the non-sequential optimization technique for a CCOS process utilizing multiple TIFs was developed and its performance was demonstrated. This technique benefits from the use of a wider search space (including the tool shape, tool size, and so forth) than that of conventional optimization techniques. An optimal TIF set for a given target removal is suggested as an optimization result, so that high (>95%) figuring efficiency can be achieved.

#116367 - $15.00 USD Received 28 Aug 2009; revised 30 Oct 2009; accepted 6 Nov 2009; published 18 Dec 2009

Also, the simulations showed that the CCOS process equipped with the new optimization technique effectively suppresses the mid-spatial frequency error. About 89% reduction in the slope error RMS was successfully demonstrated in the Case 2.3 simulation. The high time-efficiency (*i.e.* short polishing time) of the CCOS process using the new technique was clearly demonstrated. The CCOS aided with this new optimization technique enables mass fabrication processes for high quality optical surfaces, and will meaningfully contribute to the materialization of the next generation optical systems, such as Laser Inertial Fusion Engine [28] and ELT projects [12–16]

Appendix A. TIF library

Table 3. Parameters for the TIF library generation [g]

TIF No.	Tool RPM [h]	Workpiece RPM [h]	Tool width [i] (cm)	Tool motion	Orbital motion radius [j] (cm)	Tool Shape
1	1	<<1	60	Spin	N/A	Circle
2	1	<<1	60	Spin	N/A	Donut
3	1	<<1	60	Orbital	15	Circle
4	1	<<1	60	Orbital	10	Circle
5	1	<<1	60	Orbital	10	Square
6	1	<<1	60	Orbital	10	Rectangle
7	1	<<1	60	Orbital	5	Sector
8	1	<<1	60	Orbital	5	Sector
9	1	<<1	60	Orbital	10	Ellipse
10	1	<<1	60	Orbital	12	Donut
11	1	2.00	60	Spin	N/A	Circle
12	1	1.00	60	Spin	N/A	Circle
13	1	0.50	60	Spin	N/A	Circle
14	1	0.10	60	Spin	N/A	Circle
15	1	0.05	60	Spin	N/A	Circle
16	1	–0.05	60	Spin	N/A	Circle
17	1	–0.10	60	Spin	N/A	Circle
18	1	–0.15	60	Spin	N/A	Circle
19	1	–0.20	60	Spin	N/A	Circle
20	1	–1.00	60	Spin	N/A	Circle
21	1	1.50	70	Spin	N/A	Circle
22	1	1.50	60	Spin	N/A	Circle
23	1	1.50	50	Spin	N/A	Circle
24	1	1.50	40	Spin	N/A	Circle
25	1	1.50	30	Spin	N/A	Circle
26	1	1.50	60	Orbital	20	Circle
27	1	1.50	60	Orbital	15	Circle
28	1	1.50	60	Orbital	10	Circle
29	1	1.50	60	Spin	N/A	Circle
30	1	1.50	50	Spin	N/A	Circle

[g] Preston constant [9] was assumed as −100μm/psi(m/sec)hour with 1 PSI tool pressure.
[h] Positive and negative RPM means clockwise and counterclockwise rotation, respectively.
[i] Tool width is measured in max direction.
[j] Orbital motion radius refers to the radius of the circle passing through the points A~F in Fig. 1 (left).

#116367 - $15.00 USD Received 28 Aug 2009; revised 30 Oct 2009; accepted 6 Nov 2009; published 18 Dec 2009

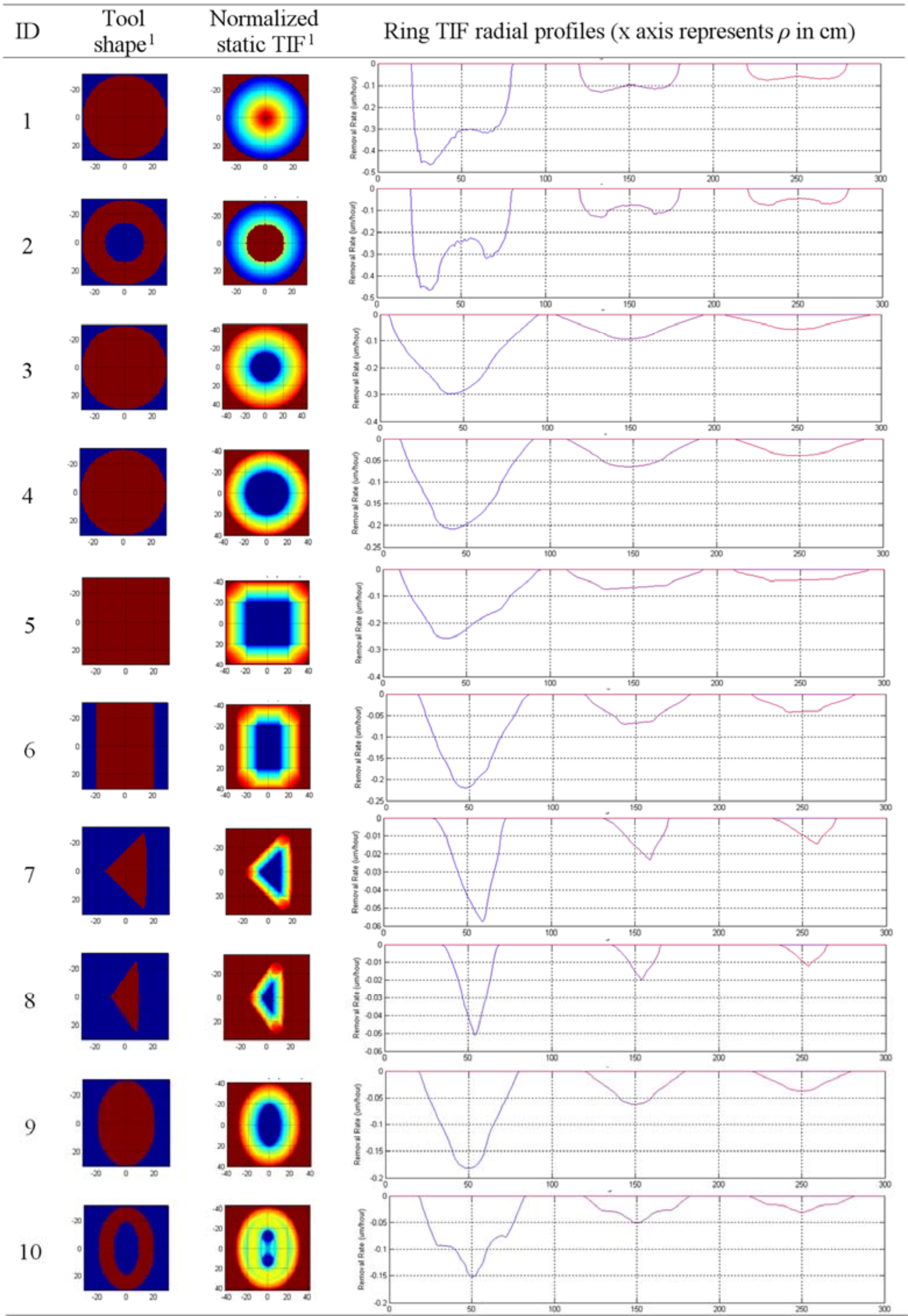

Fig. 6. Complementary TIF library

#116367 - $15.00 USD Received 28 Aug 2009; revised 30 Oct 2009; accepted 6 Nov 2009; published 18 Dec 2009

ID	Tool shape[1]	Normalized static TIF[1]	Ring TIF radial profiles (x axis represents ρ in cm)
11	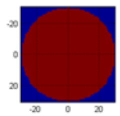	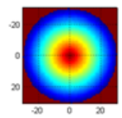	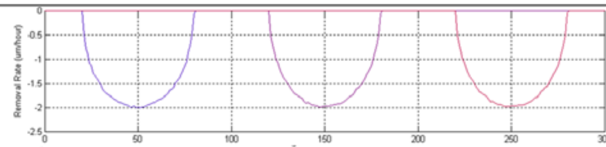
12	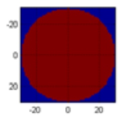	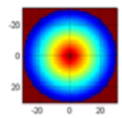	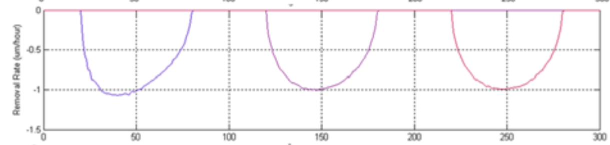
13	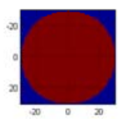	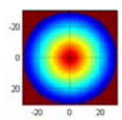	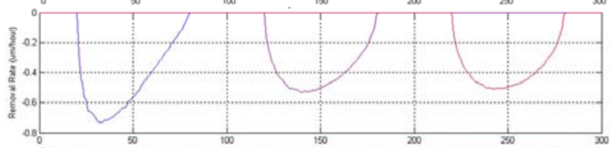
14	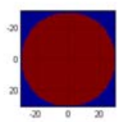	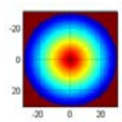	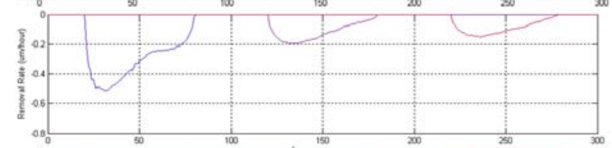
15	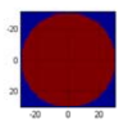	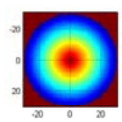	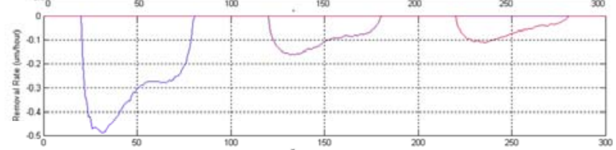
16	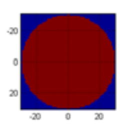	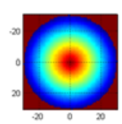	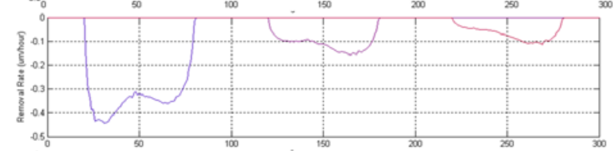
17	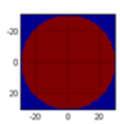	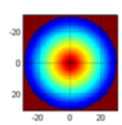	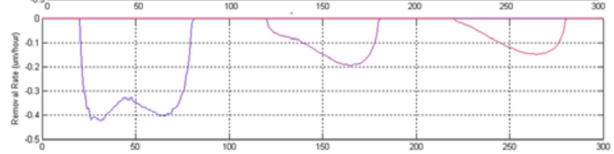
18	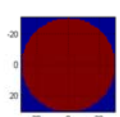	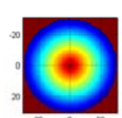	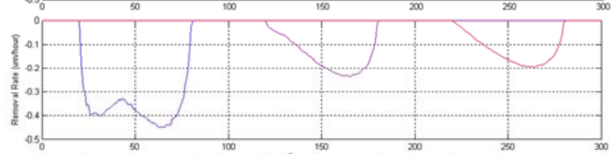
19	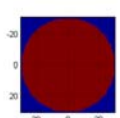	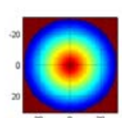	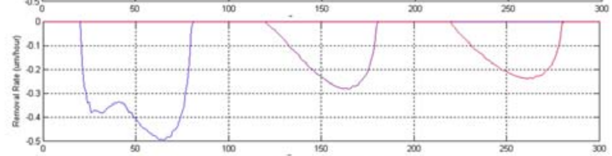
20	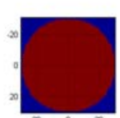	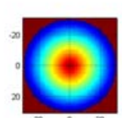	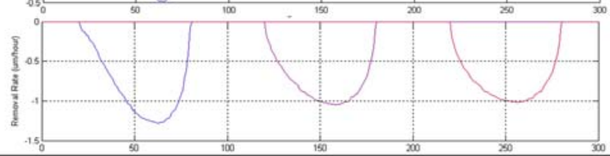

Fig. 6. Complementary TIF library (*continued*)

#116367 - $15.00 USD Received 28 Aug 2009; revised 30 Oct 2009; accepted 6 Nov 2009; published 18 Dec 2009

ID	Tool shape[1]	Normalized static TIF[1]	Ring TIF radial profiles (x axis represents ρ in cm)
21	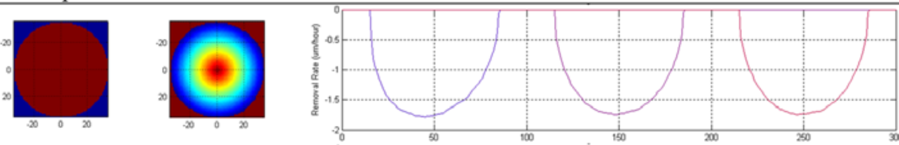		
22	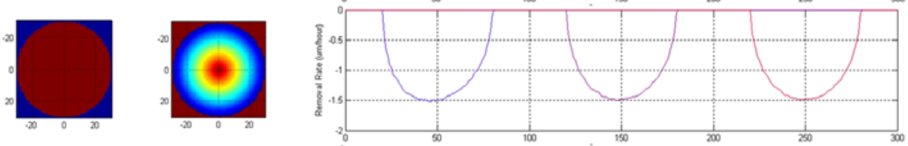		
23	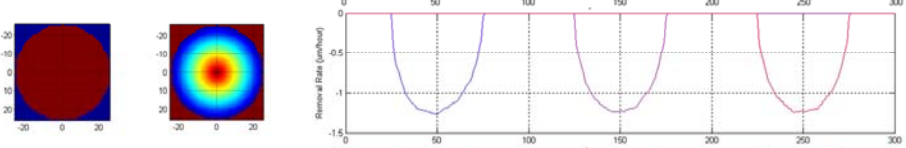		
24	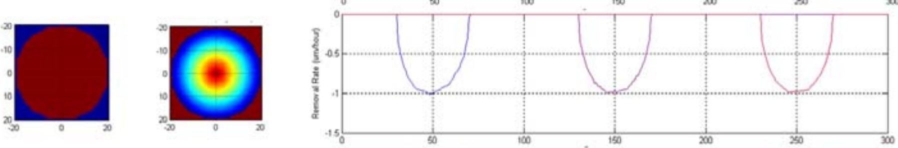		
25	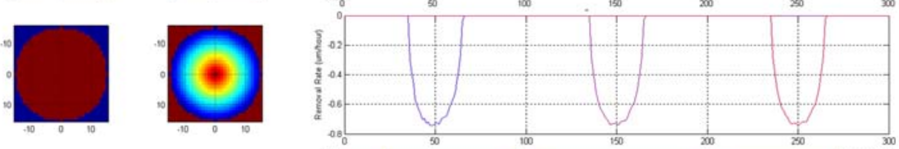		
26[k]	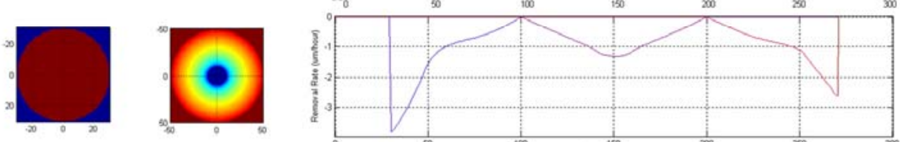		
27[k]	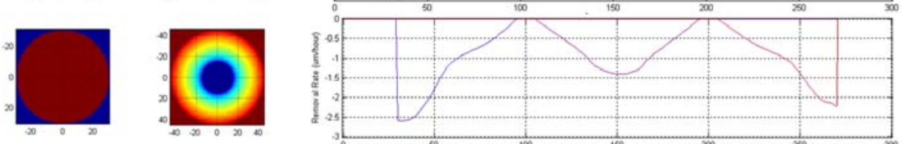		
28[k]	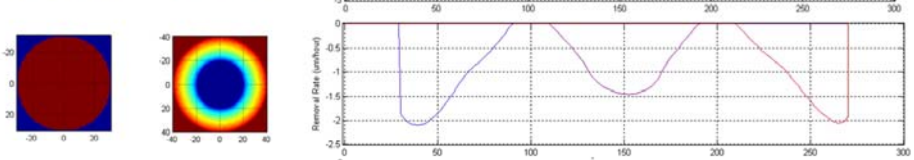		
29[k]	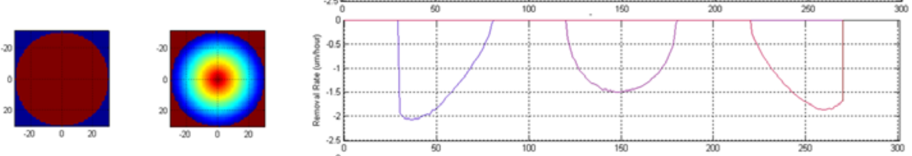		
30[k]	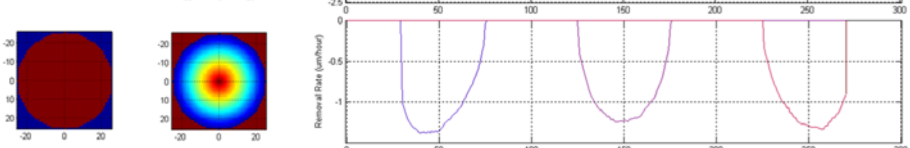		

[k] The parametric edge model [19] was used to calculate the edge TIFs for the TIF No. 26-30. Workpiece inside and outside edge was at 30 and 270cm, respectively.
[l] The units for the tool shape and the normalized static TIF are in cm.

Fig. 6. Complementary TIF library (*continued*)

#116367 - $15.00 USD Received 28 Aug 2009; revised 30 Oct 2009; accepted 6 Nov 2009; published 18 Dec 2009

Appendix B. Analytical solution for the dwell time map

The analytical solution for the dwell time map in Eq. (1) does not exist in general. The main reason is that the CCOS process is not a Linear Shift Invariant (LSI) system. For a LSI system, the TIF (*i.e.* impulse response) should not be a function of workpiece coordinates $x_{workpiece}$ and $y_{workpiece}$ [29]. The TIF should be same everywhere on the workpiece.

Conventional CCOS often assumes a LSI system (*i.e.* spatially invariant TIF) [20,22,30] by assuming, i) the velocity of the workpiece motion is small enough compare to the tool motion and ii) there is no edge effect. In this case, by replacing the $TIF(x_{TIF}, y_{TIF}, x_{workpiece}, y_{workpiece})$ with $TIF(x_{TIF}, y_{TIF})$ in Eq. (1), the analytical solution for the dwell time map can be calculated using the property of Fourier transform as below. (The 2D convolution operator can be changed to the multiplication operator.)

$$\begin{aligned}
& FF[Removal_map(x_{workpiece}, y_{workpiece})] \\
&= FF[Dwell_time_map(x_{workpiece}, y_{workpiece}) ** TIF(x_{TIF}, y_{TIF})] \\
&= FF[Dwell_time_map(x_{workpiece}, y_{workpiece})] \cdot FF[TIF(x_{TIF}, y_{TIF})]
\end{aligned} \tag{10}$$

where FF is the 2D Fourier transform. Then, using the inverse Fourier transform, the dwell time map is

$$\begin{aligned}
& Dwell_time_map(x_{workpiece}, y_{workpiece}) \\
&= FF^{-1}\left[\frac{FF[Removal_map(x_{workpiece}, y_{workpiece})]}{FF[TIF(x_{TIF}, y_{TIF})]}\right] \\
&= FF^{-1}\left[\frac{FF[Target_removal_map(x_{workpiece}, y_{workpiece})]}{FF[TIF(x_{TIF}, y_{TIF})]}\right]
\end{aligned} \tag{11}$$

where FF^{-1} is the inverse 2D Fourier transform. The removal map is replaced with the target removal map, which is the ideal goal. This is an analytical and ideal dwell time map solution, which gives the perfect removal map.

However, the analytical solution cannot be used as it is. The analytical dwell time map solution in Eq. (11), in general, may result in negative values that are unrealistic. A negative dwell time means that the tool would add material to the workpiece surface. Another practical issue comes when we use the numerical techniques to compute the Fourier transform, such as Fast Fourier transform (FFT). Because all functions should be limited in a finite range in any computational environment, the analytical solution is often not valid especially for the edge regions of the workpiece.

Also, the LSI assumption is not valid for the non-sequential CCOS optimization. Instead, the TIF should be handled as a function of position on the workpiece. For instance, the edge TIFs are very strong function of overhang distance over the edge of the workpiece [19]. Also, if the TIF shape is not axisymmetric (*e.g.* square tool case) and the workpiece rotates, the orientation of the square TIF also rotates with respect to the workpiece. Thus, no general solution to the dwell time map in Eq. (1) exists analytically.

Acknowledgments

We acknowledge that this work was supported by the Optical Engineering and Fabrication Facility of the College of Optical Sciences at the University of Arizona. We thank Martin Valente (Optical Engineering and Fabrication Facility), Anastacia Manuel (College of Optical Sciences) and Robert Parks (College of Optical Sciences) at the Univ. of Arizona for assistance in the final manuscript preparation.

#116367 - $15.00 USD Received 28 Aug 2009; revised 30 Oct 2009; accepted 6 Nov 2009; published 18 Dec 2009